MONASH University

# Biophysical interactions of outer membrane proteins and carbon nanomaterials with biomimetic membranes

Rajiv Thapa

A thesis submitted for the degree of Doctor of Philosophy at
Monash University in 2021
School of Chemistry

To my Dad

**Copyright notice**

## Abstract

The biological cell is the most important unit of life and is surrounded by a functional cell membrane. Despite the many different functions of cells, they are all composed of similar lipids, proteins, nucleic acids, and polysaccharides. Among its many features, the cell membrane contains gates (proteins) that are highly selective and regulate transport across the membrane. The membrane itself comprises lipids that are arranged in a bilayer and create a permeability barrier. A small portion of these lipids interact with some membrane proteins and are essential for the function of these proteins.

The overall theme of this thesis is interrogating biomimetic membranes and their interactions with proteins and carbon nanomaterials. In the first part of this thesis, we investigate outer membrane protein (Pet protein) folding kinetics in detergent micelles. The second part of the thesis looks at the interaction of graphene-like nanomaterials with different lipids.

Pet proteins are classified as autotransporter proteins based on their secretion pathway, and they are produced by Gram-negative bacteria. These proteins are closely associated with virulence and thereby disease outcomes, particularly for key bacteria such as *Escherichia coli*. They consist of an N-terminal sequence and C-terminal β-barrel domain, separated by the secreted passenger domain (virulence factor). After translocation of the passenger domain across the outer membrane, this section is released into the extracellular milieu via autocatalytic processing. The 12 stranded β-barrel facilitates the translocation of the passenger domain by forming a pore across the outer membrane. In this work, we studied the mutational effects of several conserved residues in the β-barrel domain and their impact on translocation of the passenger domain across the outer membrane.

Mutation of conserved glycine residues within the β-barrel domain resulted in non-native folding of Pet protein, which limited the passenger domain translocation to the extracellular milieu. Biophysical studies of Pet protein showed that the non-mutated protein was quickly folded into its native structure and facilitated passenger domain translocation.

Graphene and its derivatives have garnered considerable attention in different fields of research owing to their unique physical and chemical properties. The second part of this thesis focuses on the interactions of graphene oxide and reduced graphene oxide with biomimetic membranes and lipid vesicles. Graphene oxide and reduced graphene oxide comprise an atomically thin carbon lattice of graphene and are readily dispersible in water because of the presence of functional groups containing oxygen. Since graphene and its derivatives are being developed for different biotech and biomedical applications, it is essential to understand their biological effects and toxicity. The latter part of this thesis investigates the interaction of graphene oxide and reduced graphene oxide with lipid bilayers (biomimetic membranes) and lipid vesicles. Experimental techniques such as atomic force microscopy (AFM), force spectroscopy, small-angle neutron scattering and quartz crystal microbalance with dissipation are used to better understand the interactions, assembly, and surface chemistry.

Chapter 5 investigates interactions of GO and rGO with lipids using AFM imaging and force spectroscopy. This approach provides an overview of how GO interacts differently with charged and zwitterionic lipid bilayers. In most cases, introduction of GO to the lipid bilayer led to compromised integrity of the lipid bilayer. The extent of bilayer disruption differed based on the overall charge of the lipid bilayer.

Chapter 6 discusses interactions of GO and rGO with lipid vesicles using small-angle scattering to investigate bulk properties. Most of the interactions of GO with liposomes led to rupturing of the vesicles and reconfiguration of lipids from the smooth surfaces of

liposomes to a fractal composite. However, when rGO was introduced to anionic vesicles, interactions were limited and most liposomes remained intact, indicating again a role of charge and surface chemistry in lipid–nanomaterial interactions.

## Declaration

This thesis is an original work of my research and contains no material which has been accepted for the award of any other degree or diploma at any university or equivalent institution and that, to the best of my knowledge and belief, this thesis contains no material previously published or written by another person, except where due reference is made in the text of the thesis.

Signature: ……

Print Name: …….

Date: …….

## Publications during enrolment

Leyton, D.L., Johnson, M.D., **Thapa, R.**, Huysmans, G.H., Dunstan, R.A., Celik, N., Shen, H.H., Loo, D., Belousoff, M.J., Purcell, A.W. and Henderson, I.R. (2014). A mortise–tenon joint in the transmembrane domain modulates autotransporter assembly into bacterial outer membranes. *Nature Communications*, **5**, 1–11.

Prathapan, R., **Thapa, R.**, Garnier, G. and Tabor, R. F. (2016). Modulating the zeta potential of cellulose nanocrystals using salts and surfactants. *Colloids and Surfaces A: Physicochemical and Engineering Aspects*, **509**, 11–18.

Greene, G. W., **Thapa, R.**, Holt, S. A., Wang, X., Garvey, C. J. and Tabor, R. F. (2017). Structure and property changes in self-assembled lubricin layers induced by calcium ion interactions. *Langmuir*, **33**, 2559–2570.

## Acknowledgements

First and foremost, I would like to thank my supervisor A/Prof. Rico Tabor. Thank you for your helpful discussions, encouragement and inspiring me. Above all, thank you for all the chats and being there through my ups and downs (more downs than up). You took a chance on me and I will forever be thankful.

I thank Dr. Denisse Leyton, A/Prof. Lisa Martin and Professor Trevor Lithgow for introducing me to protein chemistry and their support during the early years of my PhD. I am thankful to Trevor for giving me an opportunity to come to Monash.

I also want to thank my lab-mates Dr. Ragesh Prathapan, Dr. Tom McCoy, Dr. Muthana Ali and Dr. Matthew Pottage. I want to thank Dr. Tom McCoy for his guidance and discussion during our SANS trip.

To my family, especially my parents. Thank you for your constant love and support throughout all my endeavours. I also want to thank my wife for coming with me on this journey, which has taken just a little longer than expected. You are probably more relieved than I am that our PhD journey is coming to a close. Kayden and Mason – this would not have been possible without you two in my life.

## Contents

**ABSTRACT** ..... **III**

**DECLARATION** ..... **VI**

**ACKNOWLEDGEMENTS** ..... **VIII**

**LIST OF FIGURES** ..... **XI**

**CHAPTER 1. BACKGROUND** ..... **1**

1.1. Gram-negative and Gram-positive bacteria ..... 1
1.2 Gram-negative bacterial protein secretion systems ..... 3
1.3 Details on the secretion pathway of autotransporters ..... 6
1.4. Serine protease autotransporters of the Enterobacteriaceae (SPATEs) ..... 7
1.5. Plasmid-encoded toxin (Pet) ..... 8
1.6. Membrane protein folding ..... 8
1.7. Aim of this study ..... 10
1.8 References: ..... 14

**CHAPTER 2. GLYCINE TO ALANINE MUTATION IN PETβ BARREL LEADS TO INEFFICIENT PROTEIN FOLDING.** ..... **16**

2.1 Introduction ..... 16
2.2. Materials and Methods ..... 18
2.2.1 Plasmid construction ..... 18
2.2.2 Materials ..... 19
2.2.3 Methods ..... 20
2.2.4 Biophysical assays ..... 23
2.3 Results ..... 24
2.3.1 Pet β-barrel protein folding, a schematic representation ..... 24
2.3.2 Pet $^{\Delta 1\text{-}902}$, Pet $^{\Delta 1\text{-}902}G^{1061}A$ and Pet $^{\Delta 1\text{-}902}G^{1076}A$ folding in LDAO micelles ..... 26
2.3.3 β-barrel heat modifiability: ..... 32
2.3.4. Gel filtration of folded Pet protein ..... 34
2.3.4. Folding of Pet $^{\Delta 1\text{-}902}G^{1061}A$ ..... 35
2.4 Discussion ..... 36
2.5. References ..... 39

**CHAPTER 3. DIFFERENT FACTORS AFFECTING PET PROTEIN FOLDING** ..... **41**

3.1. Introduction ..... 41
3.2. Materials and Methods ..... 42
3.2.1 Materials ..... 42
3.2.2 Methods ..... 43
3.2.3 Biophysical assays ..... 46
3.3 Results ..... 47
3.3.1. Pet β- barrel protein folding, different length of passenger domains ..... 47
..... **Error! Bookmark not defined.**
3.3.2 Protein folding at lower temperatures (15° C and 4° C) ..... 50
3.3.3 Pet 232β, Pet 464β and Pet 966β folding @ 15° C ..... 53
3.3.4 Pet 232β, Pet 464β and Pet 966β tertiary structure using Circular Dichroism and Fluorescence Spectroscopy ..... 54
3.3.5 Tertiary structure using tryptophan fluorescence ..... 58
3.3.6 Pet 232β, Pet 464β and Pet 966β folding @ 4 °C ..... 59
3.3.6 Folded proteins digested with trypsin ..... 61
3.4. Discussion and Conclusion ..... 66
3.5. References: ..... 69

**CHAPTER 4. CARBON NANOMATERIALS BACKGROUND** ..... **71**

4.1 Cells and cell membranes: a biological interface ..... 71
4.1.1. Phospholipids, Liposomes and lipid bilayers ..... 72
4.2. Graphene, Graphene Oxide and Reduced Graphene Oxide ..... 77
4.3. Aims: ..... 80
4.4.References: ..... 82

**CHAPTER 5. INTERACTIONS OF BIOMIMETIC MEMBRANES WITH CARBON NANOMATERIALS: GRAPHENE OXIDE (GO) AND REDUCED GRAPHENE OXIDE (RGO) ..... 85**

5.1.Introduction: ..... 85
5.1.1.Carbon nanomaterials ..... 85
5.1.2. Atomic Force Microscopy (AFM) for lipid studies ..... 86
5.2.Objective: ..... 89
5.3. Experimental design and methodology: ..... 89
5.3.1.Phospholipids ..... 89
5.3.2. Liposome Preparation: ..... 91
5.3.3. Quartz Crystal Microbalance and Dissipation (QCM-D): ..... 91
5.3.4. Attenuated total reflectance – Fourier-transform infrared spectroscopy (ATR-FTIR): ..... 92
5.4. Results: ..... 92
5.4.1. AFM imaging of lipid bilayer in AC mode ..... 92
5.4.2. Imaging of lipid bilayers in liquid – contact mode: ..... 94
5.4.3. Interaction between GO and supported lipid bilayer: ..... 96
5.4.4. Exploration of DOPC and GO interactions using force spectroscopy: ..... 99
5.4.5 DOPC interaction with rGO: ..... 104
5.4.6. POPC lipid bilayer integrity: ..... 106
5.4.7. POPC and GO interactions: ..... 107
5.4.8. Positively charged POPC/POEPC interaction with GO ..... 108
5.4.9. Negatively charged POPC/POPS interactions with GO: ..... 110
5.4.10. QCM-D study of bilayer interactions with GO: ..... 111
5.5. Conclusion: ..... 115
5.6. References: ..... 118

**CHAPTER 6. GRAPHENE OXIDE AND REDUCED GRAPHENE OXIDE INTERACTION WITH LIPOSOMES – STOPPED-FLOW SANS EXPERIMENT ..... 121**

6.1. Introduction: ..... 121
6.2. Methods: ..... 123
6.2.1. Small-angle neutron scattering (SANS): ..... 123
6.2.2. Modelling SANS data: ..... 126
6.3. Results and Discussion: ..... 128
6.3.1. Zwitterionic liposome interaction with GO ..... 129
6.3.2. Anionic liposome (POPC/POPS) interaction with GO ..... 139
6.3.3. Zwitterionic liposome interaction with rGO ..... 140
6.3.4. DPPC interaction with rGO ..... 141
6.3.5. POPC interaction with rGO. ..... 144
6.3.6. Negatively charged liposome interaction with rGO ..... 146
6.4. Discussion and conclusion ..... 147
6.5. References: ..... 152

**CHAPTER 7. CONCLUSIONS AND FUTURE DIRECTIONS ..... 154**

7.1. Pet β-barrel folding: ..... 154
7.2. Interactions of biomimetic membranes with graphene oxide and reduced graphene oxide ..... 158
7.3. References: ..... 164

**List of Figures**

**Chapter 1.**

**Figure 1.1:** Schematic of a Gram-negative bacterial cell membrane architecture, as exemplified by Escherichia coli.

**Figure 1.2:** Schematic representation of AT domains including an N-terminal signal peptide (SP, white), a central passenger domain (red) and a C-terminal β-domain.

**Figure 1.3:** AT passenger domain translocation.

**Figure 1.4:** Different types of secretion system of Gram-negative bacteria.

**Figure 1.5.** Two classes of integral membrane proteins.

**Figure 1.6.** Schematic representation of protein used in this study.

**Chapter 2.**

**Figure 2.1:** Schematic representation of Type 5 secretion system.

**Figure 2.2:** Pet β-barrel protein folding, a schematic representation.

**Figure 2.3:** Electrophoretic analysis of Pet $^{\Delta 1\text{-}902}$ and Pet $^{\Delta 1\text{-}902}G^{1076}A$ refolding.

**Figure 2.4**: Far UV CD spectra on the left panel and tryptophan fluorescence spectra on the right panel.

**Figure 2.5:** Folding of Pet $^{\Delta 1\text{-}902}$ and Pet $^{\Delta 1\text{-}902}G^{1076}A$ samples digested with trypsin in order to look at the different resistant fragment.

**Figure 2.6:** Thermal denaturation of folded Pet protein.

**Figure 2.7**: Chromatogram for the gel filtration.

**Figure 2.8:** 0 min to 24 hours folding and the folding of Pet $^{\Delta 1\text{-}902}G^{1061}A$.

**Chapter 3.**

**Figure 3.1:** Schematic representation comparing the proteins explored in Chapters 1 and 2.

**Figure 3.2:** Schematic representation of protein used in this study.

**Figure 3.3:** SDS-PAGE of Pet 116β and Pet 116β G58A (mutation in the barrel domain) folding at 37° C.

**Figure 3.4. A.** Pet 116β folding at 15 °C and **B.** Pet 116β G58A folding at 4 °C.

**Figure 3.5: A.** Pet 116β folding at 15 °C and **B.** Pet 116β G58A folding at 4 °C.

**Figure 3.6:** An exploration of the effect of length of passenger domain on Pet protein folding.

**Figure 3.7:** CD spectra of folded Pet 116β, Pet 464β and Pet 966β at 15 °C.

**Figure 3.8:** Tryptophan fluorescence spectra showing: **A**. Pet 116β folding at 15 °C; **B.** Pet 464β folding at 15 °C; and **C**. Pet 966β folding at 15 °C.

**Figure 3.9**: Pet protein folding at 4 °C. **A**. Pet 232β folding at 4 °C, **B**. Pet 464β folding at 4 °C and **C**. Pet 966β folding at 4 °C.

**Figure 3.10**: Trypsin treated samples probed for barrel and passenger domain.

**Figure 3.11**: Trypsin treated samples probed for barrel and passenger domain.

**Figure 3.12:** Trypsin treated samples probed for barrel and passenger domain.

**Figure 3.13:** Trypsin treated samples probed for barrel and passenger domain.

**Chapter 4.**

**Figure 4.1**: Liposomes are therefore formed as spheres comprising a 'capsule' of lipid bilayer surrounding an aqueous phase droplet.

**Figure 4.2: T**he structure of a phosphotidylcholine (1,2- dimyristoyl-sn-glycero-3-phosphocholine).

**Figure 4.3**: Chemical structures of the phospholipids used in this thesis.

**Figure 4.4:** Each layer of Graphite is made up of carbon atoms linked together in a hexagonal lattice.

**Chapter 5.**

**Figure 5.1:** Schematic representation of graphite, GO and rGO.

**Figure 5.2:** A) Schematic representation of AFM. B) Different imaging modes used in the experiment. Contact mode (top) and tapping mode (bottom

**Figure 5.3:** Phospholipids used in this study. DOPC and POPC are zwitterionic phospholipids. POPS is a negatively charged lipid and POEPC is a positively charged lipid.

**Figure 5.4**: AFM images of DOPC drop-casted, rinsed with water after 60 minutes, dried and imaged in AC mode.

**Figure 5.5:** AFM images of DOPC liposome dispersions drop-casted, rinsed with water after 30 mins and placed in a Petri dish containing water.

**Figure 5.6:** AFM images of DOPC deposited from liposomes that were drop-cast, rinsed with water after 30 mins, incubated with GO for another 30 mins, rinsed and placed in a petri dish containing water.

**Figure 5.7:** Lipid used for this study was DOPC. Liposomes were drop-casted, rinsed with water after 30 mins, incubated with GO for another 30 mins, rinsed and placed in a petri dish containing water.

**Figure 5.8**: Force curves can be used to calculate the mechanical properties such as adhesive energy, height of the lipid bilayer, Young's modulus, breakthrough force, *etc.*

**Figure 5.9**: Force curves can be used to calculate the mechanical properties.

**Figure 5.10:** DOPC supported lipid bilayer interaction with GO.

**Figure 5.11:** DOPC supported lipid bilayer interaction with rGO.

**Figure 5.12:** POPC supported lipid bilayer.

**Figure 5.13:** Interactions between POPC supported lipid bilayer GO.

**Figure 5.14:** POPC:POEPC (cationic) lipid bilayer.

**Figure 5.15:** POPC:POPS (anionic) lipid bilayer. A) AFM image of POPC:POPS bilayer. B) Representative force curve of POPC:POPS lipid bilayer.

**Figure 5.16:** Formation of biomimetic membrane by liposome rupture and fusion.

**Figure 5.17:** QCM data of POPC interaction with GO.

**Chapter 6.**

**Figure 6.1:** Schematic representation of a SANS setup.

**Figure 6.2:** Incident neutron vector $\vec{k}_i$ and the scattered neutron vector $\vec{k}_s$ and the scattering vector $\vec{q}$ is given as $\vec{q} = \vec{k}_s - \vec{k}_i$.

**Figure 6.3:** Small angle neutron scattering data from DOPC vesicles, and their interaction with different concentrations of graphene oxide (GO).

**Figure 6.4:** Scattering plots of DPPC (5mg/mL) by itself and its interaction with different concentrations of GO. A) SANS data of DPPC by itself, and in mixtures with with GO (5:1, 2:1 and 1:1).

**Figure 6.5:** Scattering plots of POPC (5 mg/mL) by itself and its interaction with different concentrations of GO.

**Figure 6.6:** Scattering plot of POPC:POPS (3:1) by itself and with different concentrations of GO.

**Figure 6.7:** Scattering plot of DPPC by itself and with different concentrations of rGO.

**Figure 6.8:** Scattering plot of POPC by itself and with different concentrations of rGO.

**Figure 6.9:** Scattering plot of POPC:POPS (3:1) by itself and with different concentrations of rGO.

**Figure 6.10:** Schematic showing the hypothesised outcomes of GO (rGO) interactions with liposomes.

## List of Tables

### Chapter 1.

**Table 1.1:** Examples of serine protease autotransporters and their functions. From Weiss *et al.* [23] with modifications.

### Chapter 6.

**Table 6.1**: Fitted SANS parameters for interaction of GO with lipids where a 'broad peak' (Lorentzian plus Porod exponent) was used to fit scattering data.

**Table 6.2:** Fitted SANS parameters for interaction of GO with lipids where a multilamellar vesicle was used to fit scattering data.

**Table 6.3:** Fitted SANS parameters for interaction of rGO with lipids where a 'broad peak' (Lorentzian plus Porod exponent) was used to fit scattering data.

**Table 6.4:** Fitted SANS parameters for interaction of rGO with lipids where a multilamellar vesicle was used to fit scattering data.

# Chapter 1. Background

## 1.1. Gram-negative and Gram-positive bacteria

Bacteria are broadly classified into two categories: Gram-positive and Gram-negative, differentiated by Gram staining. This is a method of cell differentiation by detection of peptidoglycan, present only in the cell walls of Gram-positive bacteria. Gram-positive bacteria have a single (inner) membrane, while Gram-negative bacteria contain two membranes, an inner membrane (IM) and outer membrane (OM, Figure 1.1). In the case of Gram-negative bacteria, the space between the two membranes is called the periplasm [1]. Although there are some variations among different bacterial species, the overall structure

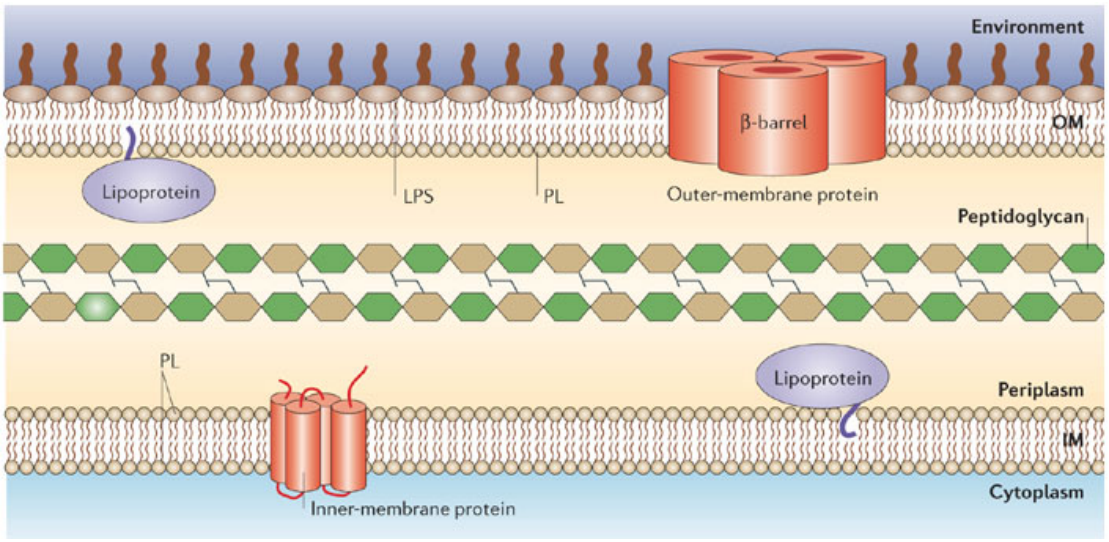


**Figure 1.1.** Schematic of a Gram-negative bacterial cell membrane architecture, as exemplified by Escherichia coli. The cytoplasm of E. coli is surrounded by the inner membrane (IM), periplasm and the outer membrane (OM). Unlike the IM, the OM is an asymmetric bilayer containing phospholipids and lipopolysaccharides (LPS) in its inner and outer leaflets respectively. The OM also contains β-barrel integral membrane proteins. This Figure was reproduced from Ruiz *et al.* [2].

and composition of the OM is largely conserved. Unlike the IM, the OM is an asymmetric bilayer containing phospholipids and lipopolysaccharides (LPS) in its inner and outer leaflets respectively. Both bacteria have a peptidoglycan layer comprising amino acids and a sugar-containing polymer. In the case of Gram-negative bacteria, the peptidoglycan layer is located in the outer layer of the inner membrane (Figure 1.1) [1]. An equivalent peptidoglycan layer is also present in the outer layer of Gram-positive bacteria, but in this instance, the peptidoglycan layer is relatively thicker than that of Gram-negative bacteria.

Proteins are secreted across the inner membrane of Gram-negative bacteria to the periplasmic space. In case of Gram-negative bacteria, periplasm is the space between the outer membrane and the inner membrane [3]. Unfolded proteins that get transported across the inner membrane to the periplasm either fold in the periplasm or once they have passed the outer membrane. Chaperone proteins are a class of biomolecules that exist in the periplasm, and which help proteins fold. The mechanism and action of many chaperone proteins are not well understood and it's an active field of research. Since there is no adenosine triphosphate (ATP) in the periplasm, protein is folded in the absence of ATP [4].

Bacterial pathogenesis includes secretion of protein virulence factors that perform cell adhesion and host invasion. In the case of Gram-negative bacteria, transportation of virulence factors is rather difficult because they are synthesized in the cytoplasm and they must cross the inner membrane, the periplasmic space and finally the outer membrane before reaching the cell surface and transferring onto the host cells [4].

## 1.2 Gram-negative bacterial protein secretion systems

A Gram-negative bacterium faces the challenge of transporting proteins across two membranes: the inner and outer, whereas Gram-positive bacteria lack this outer membrane. To overcome this problem, there are protein secretion systems in place to translocate proteins across the inner and the outer membrane.

There are at least eight types of protein secretary systems, numbered I-VIII and with the basic components shown in Figure 1.4**.** Out of the seven separate Gram-negative secretion mechanisms, Autotransporter proteins **(**ATs) or Type Va represent the most common secretion pathway. The type V secretion pathway consists of three categories of two-step


**Figure 1.2.** Schematic representation of AT domains including an N-terminal signal peptide (SP, white), a central passenger domain (red) and a C-terminal β-domain.

secretion pathways : the autotransporter (AT) pathway (Va), the two-partner secretion (TPS) pathway (type Vb) and the trimeric autotransporter adhesion (TAT) pathway (type Vc secretion) [5]. Autotransporter protein sequences contain three parts: an N-terminal signal sequence, a passenger domain which is the functional virulence protein, and a C-terminal barrel or porin domain [6, 7].

Wide ranges of virulence proteins are secreted via the autotransporter (AT) pathway (Type Va), in Gram-negative bacteria [8]. AT proteins are associated with virulence in Gram-negative bacteria, with functions that include protein and lipid hydrolysis, adhesion to host cells, maturation of other virulence proteins and promoting bacterial mobility [7]. Typically,

the AT contains a signal peptide at the N-terminus that mediates transport across the inner membrane, coupled to a passenger domain that exerts biological activity in the extracellular space (Figure 1.1 and 1.3). A linker domain connects the passenger and the β-domain, which forms a β-barrel with a hydrophilic pore in the outer membrane (Figure 1.2 and 1.3) [7]. Once the AT passenger domain is translocated across the outer membrane, it goes through a series of processing steps and may cleave off from the barrel domain. Among these proteins, the β-domain (β-barrel forming domain) appears to be a common structural feature, which folds into the β-barrel motif (essentially forming a pore across the outer membrane), and is essential for transport of the passenger domain across the outer membrane [7]. Three crystal structures of the AT protein have been captured, each consisting of a 12-stranded β-barrel [9-11]. In the first part of this thesis, I seek to understand the folding and insertion of β-domain in protein encoded toxin (Pet), an autotransporter protein.

**Figure 1.3.** AT passenger domain section. The N-terminal signal sequence (pink) facilitates

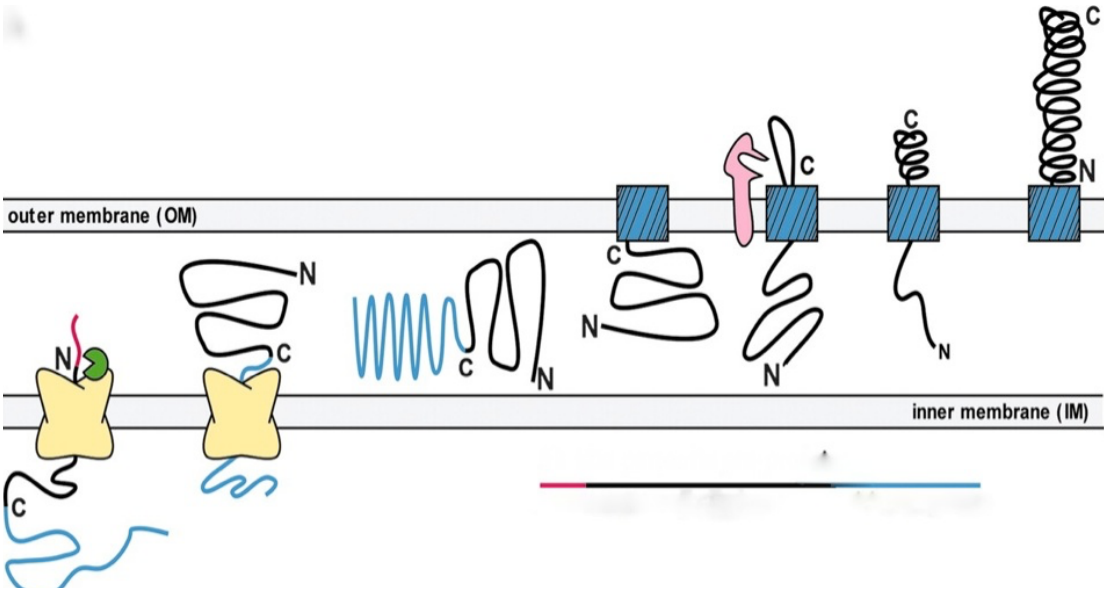


translocation of the passenger domain across the IM. The passenger domain (black) and β-barrel domain (cyan) are translocated across the periplasm, and the β-barrel forms a pore across the outer membrane. The passenger domain (virulence factor of the protein) is translocated across the OM through the pore. In this model, the passenger domain goes through the pores in the C to N terminus direction to get across the outer membrane [12]. This figure was reproduced from Junker et al [12].

Autotransporter proteins are produced in the cytoplasm and must cross the inner membrane (IM) to reach the periplasm and then the outer membrane (OM). AT translocation across the inner membrane is dependent on a translocase generated via the Secretion pathway, hence Sec-translocase. The Sec (secretion) system is the translocation system utilised in the inner membrane, and it is known to transfer unfolded proteins across the inner membrane. For Sec-dependent translocation, AT has a targeting signal that is located at the N-terminus of the protein. Translocation itself is mediated by the Sec machinery, which is composed of a core complex of three integral IM proteins, SecY, SecE and SecG, that form a heterotrimeric complex (Figure 1.4) [3, 4, 13]. ATs first bind SecA, a motor protein that drives the transport of membrane proteins, and then are fed into the channel formed by the complex.

Proteins are secreted across the inner membrane of Gram-negative bacteria and into the periplasmic space [14]. Most proteins in Gram-negative bacteria that are translocated across the inner membrane in their unfolded state fold at least to some degree in the periplasm before (a) being inserted/assembled into the outer membrane, or, complete their folding in the periplasm to be either (b) translocated across the outer membrane in a folded state or (c) remain resident in the periplasm [4]. Chaperone proteins such as SurA, Skp and DegP in the periplasm are known to help proteins fold, and their activity can be regulated by intrinsic properties of the client protein and by competition for binding to other assembly factors. One such factor is the β-barrel assembly machinery (BAM): a complex consisting of an outer membrane protein (BamA) and four lipoproteins (BamB, BamC, BamD and BamE), that catalyse the insertion of translocated proteins into the outer membrane of E. coli and other Gram-negative bacteria [4]. Delivery of client proteins to the BAM is mediated by

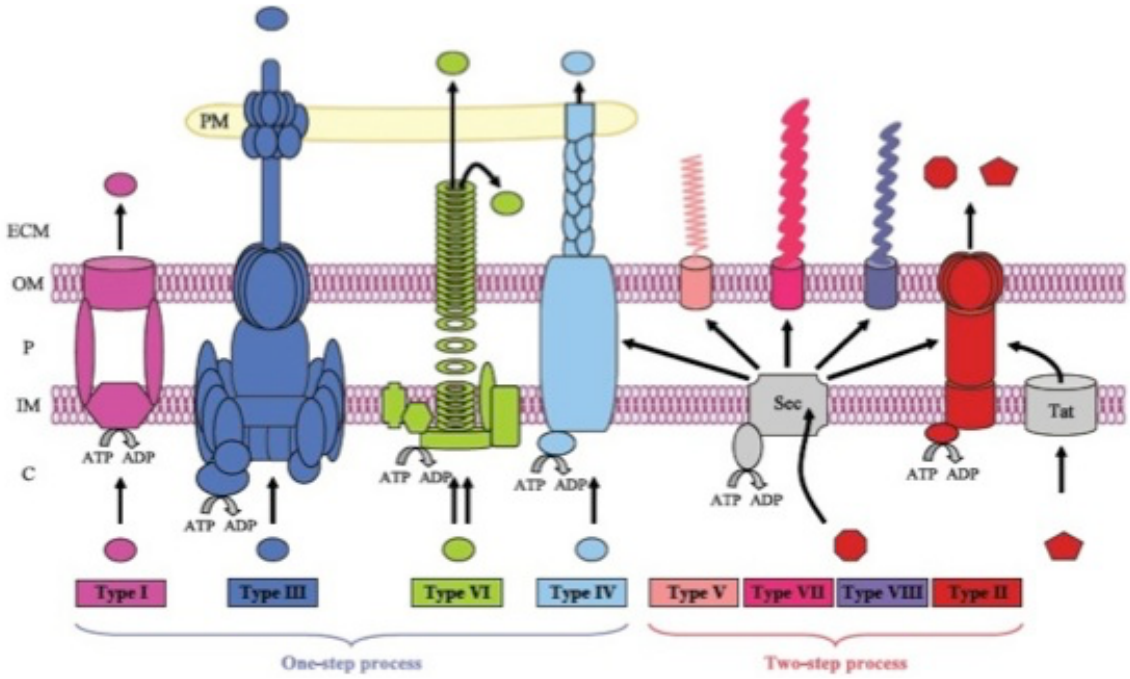


**Figure 1.4.** Different types of secretion system in Gram-negative bacteria. Image reproduced from Tseng *et al.*, 2009 [15]. There are currently nine different protein secretion system that have been identified, and they each vary significantly from each other. The focus of our study will be the type V secretion system.

several chaperones: Skp interacts with unfolded polypeptide chains, SurA and FkpA are periplasmic peptidylprolyl cis/trans isomerases [16], and the periplasmic chaperone DegP is multi-functional in that it is both a molecular chaperone, and has a protease activity that degrades any misfolded client proteins that it cannot assist to fold (or pass on to other factors) [17].

## 1.3 Details on the secretion pathway of autotransporters

Autotransporters follow a highly complex protein folding mechanism that ultimately drives the appearance of the passenger domain on the outer surface of bacterial cells. Several studies suggest that the passenger domain is translocated through the pore of the β-barrel domain in a C → N direction [18]. Studies have also shown that the passenger domain needs

to be in an unfolded conformation to go through the pore, given that artificial, folded proteins are not able to be translocated through the outer membrane [9]. In further support of this point, introduction of cysteine residues, which result in disulphide bond formation in passenger domains, creates enough of a loop to stall passenger domain secretion across the outer membrane [19]. Structural assessments are also consistent with this point: the diameter of the pore formed after the completion of folding of a 12-stranded autotransporter β-barrel is too small (≈6.4 Å to 11.0 Å) to passively allow a folded passenger domain to pass through the pore [20].

Numerous factors in the periplasm and outer membrane are required for an autotransporter to achieve its final form on the bacterial surface. Chaperones in the periplasmic space (such as Skp and SurA) bind the unfolded protein and avoid its misfolding in the periplasm [10]. BamA is necessary for the insertion of the β-domain into the outer membrane [10], as is the translocation and assembly module (TAM) [20].

## 1.4. Serine protease autotransporters of the Enterobacteriaceae (SPATEs)

SPATES are a well-studied sub-family of autotransporter proteins. The SPATEs are associated with virulence and are found in E.coli, Shigella spp. and Salmonella spp. [21]. All SPATEs have a serine protease motif that is necessary for virulence. The SPATEs' passenger domain has an N-terminal globular domain attached to a C-terminal β-helix. The β-domain in the SPATEs are the most conserved part of the protein sequence [22]. Plasmid-encoded toxin (Pet) is a member of the SPATE autotransporter sub-family. **Table 1.1** shows examples of SPATEs and their functions.

**Table 1.1.** Examples of serine protease autotransporters and their functions. From Weiss *et al.* [23] with modifications.

| NAME | Function(s) |
|---|---|
| EspP (extracellular serine protease) | Cleaves human apolipoprotein A-1 [22] |
| Hbp (haemoglobin protease) | Binding of hemoglobin |
| Pet (plasmid-encoded toxin) | Toxin, Inflammation, mucus secretion |
| Pic (protease involved in intestinal colonization) | Hemagluttin, serum resistance mediator, mucinase activity |
| SepA (Shigella extracellular protein) | Tissue inflammation, fluid accumulation |
| SigA (Shigella IgA-like protease homolog) | Toxin, Cell rounding and detachment |

## 1.5. Plasmid-encoded toxin (Pet)

Pet was first discovered on a virulence plasmid in the enteroaggregative E. coli strain 042 [24], a virulent strain of E.coli. Pet is a 137 kDa autotransporter protein that is secreted across the outer membrane, and its passenger domain is autocatalytically cleaved from its barrel domain, releasing into the extracellular milieu [25]. Pet has been found to degrade spectrin (a cytoskeletal protein found in the plasma membrane) and fodrin (similar to spectrin, in that it binds to actin and is found in plasma membranes) and the degradation is directly related to the Pet serine protease motif [25]. Enteroaggregative E.coli is known to cause diarrhoea and this has also been suggested to cause diarrheal diseases in HIV-infected adults [25]. Mutation or inhibition of the serine protease activity stops the activity of the virulence effects of Pet [25].

## 1.6. Membrane protein folding

Membrane proteins are classified into two categories: integral and peripheral, based on the nature of the membrane–protein interactions that they experience. Integral

membrane proteins (transmembrane proteins) span a phospholipid bilayer [26]. Peripheral membrane proteins are usually bound to the membrane indirectly by interactions with integral membrane proteins or directly by interactions with lipid polar head groups [27]. Two classes of integral membrane proteins are known to be characterized by the structure of their transmembrane domain: α-helical proteins and β-barrel proteins [28]. Despite significant progress towards understanding the structure and function of membrane proteins, complex fundamental questions still remain. Membrane protein folding involves binding to the membrane interface, insertion into the membrane and then a final assembly stage.

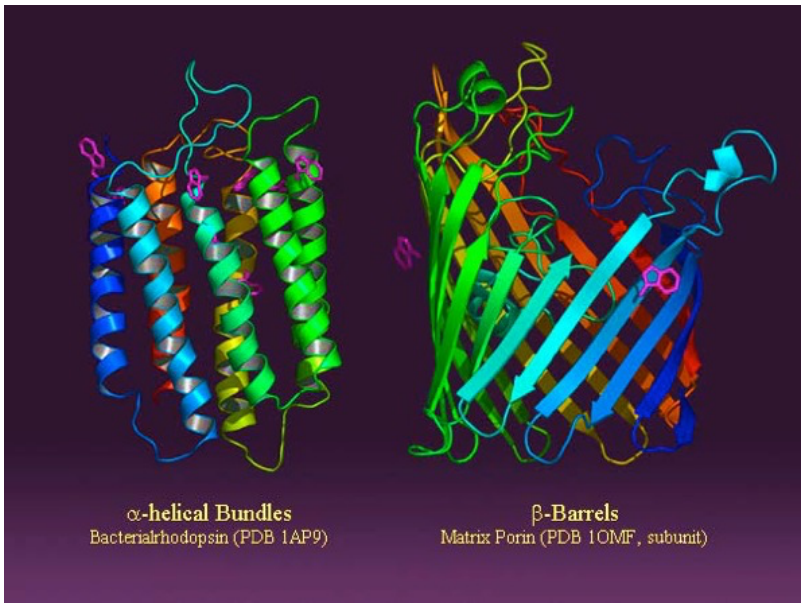


**Figure 1.5.** Two classes of integral membrane proteins. Bacteriorhodopsin forms a bundle of transmembrane α-helices that span the phospholipid bilayer. In porin (β-barrel), antiparallel β-strands span the membrane and form a barrel motif. This figure is reproduced fromhttps://www.gesundheitsindustrie-bw.de/en/article/news/a-special-focus-on-intercellular-mediators

α-helical proteins are the major class of transmembrane proteins and are characterised by containing one or more α-helices as shown in Figure 1.5. Proteins of this class with seven helices are the most common [27]. β-barrel membrane proteins are found in the outer

membranes of Gram-negative bacteria, mitochondria, chloroplasts and also in the cell walls of Gram-positive bacteria [13]. In β-barrel membrane proteins, antiparallel β-strands span the membrane and form barrel-like structures. Hydrogen bonds span between the amino acids on separate β-strands, contributing to this assembly state [29]. In transmembrane β-barrels, every second amino acid faces the non-polar lipid and must be a hydrophobic residue, while the others face the interior of the β-barrel and are mostly polar.

Protein folding affects the encryption of genetic code and how its translated. Soluble protein is generally easier to study, and there have therefore been numerous studies that explore the folding of soluble proteins using different experimental, theoretical and simulation approaches [29]. These investigations have identified and characterised intermediates and transition states of the folded protein and their kinetic and thermodynamic processes [30, 31]. In addition, protein misfolding and aggregation have also been studied extensively. Unfortunately, there hasn't been the same kind of interest in the study of membrane proteins until very recently, due to the more elaborate measurement and preparation conditions required. The exception to this general observation is that bacteriorhodopsin and Omp family membrane proteins have been studied extensively, both of which can be refolded to their native structure from a denatured state [32, 33].

## 1.7. Aim of this study

The motivation of this study is to obtain details on the structure and the assembly of the autotransporter β-barrel membrane protein. To this end, the Pet β-barrel protein is used as an experimental model for the study. It has been shown that outer membrane proteins can refold *in vitro* in the presence of detergent micelles and lipid vesicles including large unilamellar vesicles and small unilamellar vesicles [34, 35]. Studying the folding of Pet β-barrel protein *in vitro* allows us to systematically change experimental conditions and identify

the parameters that influence protein folding. The experiments presented here utilize SDS-PAGE, western blots, and spectroscopic techniques including circular dichroism and fluorescence, to investigate membrane protein folding using Pet β-barrel membrane protein.

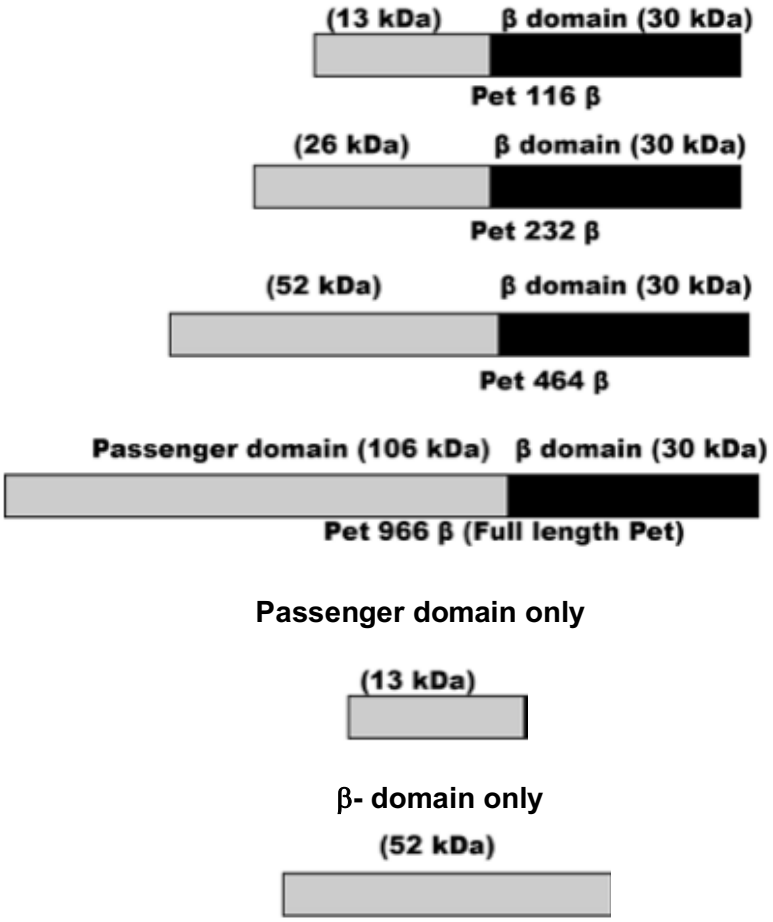


**Figure 1.6.** Schematic representation of the proteins used in this study. The full-length Pet is 136 kDa (106 kDa is the passenger domain and 30 kDa is the barrel domain). Pet 464β contains a 52 kDa passenger domain (truncated from the 106 kDa full length passenger domain) and a 30 kDa barrel domain. Pet 232β contains a 26 kDa passenger domain and a 30 kDa barrel domain, and Pet 116β contains a 13 kDa passenger domain and a 30 kDa barrel domain. Pet 116 and Pet 464 are the 13 kDa and 52 kDa passenger domain only.

**Specific aims of the first section of the thesis**

1. To understand why some of the residues of the Pet β-barrel protein have been conserved through evolution, and to determine their significance during autotransporter folding and assembly, explored via *in vitro* folding at 37°C. The goal of this section is to purify Pet proteins of different sizes and study their folding *in vitro*, to determine whether conserved glycine residues are important for their biogenesis. In Chapter 2, conserved glycine residues are mutated to alanine and *in vitro* folding efficiency is studied using SDS-PAGE, Western blotting, circular dichroism and fluorescence spectroscopy

2. To purify and refold Pet proteins (Pet 116β, Pet 232β, Pet 464β and pet 966β) in order to study the effects of temperature, lipids and periplasmic chaperone proteins in Pet protein folding. In Chapter 3, Pet proteins are folded at 37°C, 15°C and 4°C and analysed using SDS PAGE, western blotting and spectroscopy.

Pet proteins are expressed and purified from E.coli and folded in lauryldimethylamine-N-oxide (LDAO) at different temperatures to slow down the kinetics and compare the early stages of folding for various sizes of Pet proteins. Lipids with different head group and different acyl chain lengths will be used to study their effects on protein folding. LDAO is a detergent micelle used to study the folding of autotransporter proteins.

In Chapter 3, we investigate if the β-barrel domain accelerates folding of the passenger domain and determine whether the β-barrel initiates folding. Folded β-barrel functions to present the passenger domain at the cell surface. It has been postulated that β-barrel folding influences folding of the passenger domain. In the absence of β-barrel, passenger domain folds extremely slowly, and in this study, folding kinetics will be identified using a proteinase K assay. Folded protein samples will be probed with both barrel and

passenger antibody to identify the folding timeframe of β-barrel and passenger domain respectively.

## 1.8 References


1. Alberts, B., Molecular biology of the cell. 4th ed. 2002, New York: Garland Science. xxxiv, 1548 p.
2. Ruiz, N., D. Kahne, and T.J. Silhavy, Advances in understanding bacterial outer-membrane biogenesis. Nat Rev Microbiol, 2006. **4**(1): p. 57-66.
3. McNulty, B.C., G.B. Young, and G.J. Pielak, Macromolecular crowding in the Escherichia coli periplasm maintains alpha-synuclein disorder. J Mol Biol, 2006. **355**(5): p. 893-7.
4. Mansell, T.J., A.C. Fisher, and M.P. DeLisa, Engineering the protein folding landscape in Gram-negative bacteria. Curr Protein Pept Sci, 2008. **9**(2): p. 138-49.
5. Leyton, D.L., A.E. Rossiter, and I.R. Henderson, From self sufficiency to dependence: mechanisms and factors important for autotransporter biogenesis. Nat Rev Microbiol, 2012. **10**(3): p. 213-25.
6. Henderson, I.R., F. Navarro-Garcia, and J.P. Nataro, The great escape: structure and function of the autotransporter proteins. Trends Microbiol, 1998. **6**(9): p. 370-8.
7. Henderson, I.R., *et al.*, Type V protein secretion pathway: the autotransporter story. Microbiol Mol Biol Rev, 2004. **68**(4): p. 692-744.
8. Henderson, I.R. and J.P. Nataro, Virulence functions of autotransporter proteins. Infect Immun, 2001. **69**(3): p. 1231-43.
9. Oomen, C.J., *et al.*, Structure of the translocator domain of a bacterial autotransporter. EMBO J, 2004. **23**(6): p. 1257-66.
10. Barnard, T.J., *et al.*, Autotransporter structure reveals intra-barrel cleavage followed by conformational changes. Nat Struct Mol Biol, 2007. **14**(12): p. 1214-20.
11. van den Berg, B., Crystal structure of a full-length autotransporter. J Mol Biol, 2010. **396**(3): p. 627-33.
12. Junker, M., *et al.*, Pertactin beta-helix folding mechanism suggests common themes for the secretion and folding of autotransporter proteins. Proc Natl Acad Sci U S A, 2006. **103**(13): p. 4918-23.
13. Hunt, J.F., *et al.*, A biophysical study of integral membrane protein folding. Biochemistry, 1997. **36**(49): p. 15156-76.
14. Driessen, A.J. and N. Nouwen, Protein translocation across the bacterial cytoplasmic membrane. Annu Rev Biochem, 2008. **77**: p. 643-67.
15. Voulhoux, R., *et al.*, Role of a highly conserved bacterial protein in outer membrane protein assembly. Science, 2003. **299**(5604): p. 262-5.
16. Tseng, T.T., B.M. Tyler, and J.C. Setubal, Protein secretion systems in bacterial-host associations, and their description in the Gene Ontology. BMC Microbiol, 2009. **9 Suppl 1**: p. S2.
17. Arie, J.P., N. Sassoon, and J.M. Betton, Chaperone function of FkpA, a heat shock prolyl isomerase, in the periplasm of Escherichia coli. Mol Microbiol, 2001. **39**(1): p. 199-210.
18. Subrini, O. and J.M. Betton, Assemblies of DegP underlie its dual chaperone and protease function. FEMS Microbiol Lett, 2009. **296**(2): p. 143-8.
19. Dautin, N. and H.D. Bernstein, Protein secretion in Gram-negative bacteria via the autotransporter pathway. Annu Rev Microbiol, 2007. **61**: p. 89-112.
20. Junker, M., R.N. Besingi, and P.L. Clark, Vectorial transport and folding of an autotransporter virulence protein during outer membrane secretion. Mol Microbiol, 2009. **71**(5): p. 1323-32.

21. Selkrig, J., *et al.*, Discovery of an archetypal protein transport system in bacterial outer membranes. Nat Struct Mol Biol, 2012. **19**(5): p. 506-10, S1.
22. Yen, Y.T., *et al.*, Common themes and variations in serine protease autotransporters. Trends Microbiol, 2008. **16**(8): p. 370-9.
23. Schmidt, H., *et al.*, Identification and characterization of a novel genomic island integrated at selC in locus of enterocyte effacement-negative, Shiga toxin-producing Escherichia coli. Infect Immun, 2001. **69**(11): p. 6863-73.
24. Weiss, A. and J. Brockmeyer, Prevalence, biogenesis, and functionality of the serine protease autotransporter EspP. Toxins (Basel), 2013. **5**(1): p. 25-48.
25. Eslava, C., *et al.*, Pet, an autotransporter enterotoxin from enteroaggregative Escherichia coli. Infect Immun, 1998. **66**(7): p. 3155-63.
26. Navarro-Garcia, F., *et al.*, Plasmid-encoded toxin of enteroaggregative Escherichia coli is internalized by epithelial cells. Infect Immun, 2001. **69**(2): p. 1053-60.
27. Booth, P.J. and A.R. Curran, Membrane protein folding. Curr Opin Struct Biol, 1999. **9**(1): p. 115-21.
28. Surrey, T. and F. Jahnig, Refolding and oriented insertion of a membrane protein into a lipid bilayer. Proc Natl Acad Sci U S A, 1992. **89**(16): p. 7457-61.
29. Schulz, G.E., beta-Barrel membrane proteins. Curr Opin Struct Biol, 2000. **10**(4): p. 443-7.
30. Matysiak, S. and C. Clementi, Mapping folding energy landscapes with theory and experiment. Arch Biochem Biophys, 2008. **469**(1): p. 29-33.
31. Shea, J.E. and C.L. Brooks, 3rd, From folding theories to folding proteins: a review and assessment of simulation studies of protein folding and unfolding. Annu Rev Phys Chem, 2001. **52**: p. 499-535.
32. Baldwin, R.L., The search for folding intermediates and the mechanism of protein folding. Annu Rev Biophys, 2008. **37**: p. 1-21.
33. Brockwell, D.J. and S.E. Radford, Intermediates: ubiquitous species on folding energy landscapes? Curr Opin Struct Biol, 2007. **17**(1): p. 30-7.
34. Huang, K.S., *et al.*, Refolding of an integral membrane protein. Denaturation, renaturation, and reconstitution of intact bacteriorhodopsin and two proteolytic fragments. J Biol Chem, 1981. **256**(8): p. 3802-9.
35. Dornmair, K., H. Kiefer, and F. Jahnig, Refolding of an integral membrane protein. OmpA of Escherichia coli. J Biol Chem, 1990. **265**(31): p. 18907-11.

# Chapter 2. Glycine to Alanine mutation in Petβ barrel leads to inefficient protein folding

## 2.1 Introduction

When considering the folding of membrane protein motifs, β-barrel membrane proteins are expected to fold differently from their α-helical counterparts because their residues alternate between hydrophobic and hydrophilic chemistry [1-3]. The outermost amino acids expressed are the hydrophobic residues for interaction with the cell membrane, while the inner surface of the barrel is mostly hydrophilic to allow molecules to travel through the pore [4, 5].

Such membrane proteins are produced by secretion systems, and within these biological pathways, the Type V secretion system is one of the simplest protein secretion systems [6]. Three different subdivisions of the type V secretion system are, i) those secreted via an autotransporter system (type Va), ii) the two-partner secretion pathway (type Vb) and the type Vc system [4, 6, 7]. Fig 2.1 shows a schematic representation of the type V secretion pathway. Even though this is one of the simplest secretion systems, the folding of the autotransporter itself is complex [8, 9]. The folding and the presentation of the passenger domain on the extracellular surface of bacterial cells requires three different steps: i) folding and insertion of the 12 stranded β- barrel into the outer membrane, ii) segments of the N-terminal domain becoming entrapped within the pore of the barrel, and iii) folding of the passenger domain [9-11]. However, there are still questions as to how these folding events are coordinated. The β-barrel assembly machinery (the BAM complex) is known to catalyse the insertion of the barrel into the outer membrane in autotransporters [12-14]. This is crucial because evidence indicates that the passenger domain gets translocated through the barrel pore [9]. Chaperone proteins such as FkpA, SurA and Degp

have been known to participate in the folding and insertion of autotransporters [15-17], although their exact roles in folding and insertion is unclear. Efficient translocation of the passenger domain depends on the barrel domain of the protein, and the studies performed by Leyton *et al.* (in 2014) suggested that there are conserved motifs and conserved sequences with this barrel domain [10, 18]. These conserved motifs are posited to be targeted by the BAM complex and other chaperone proteins during folding and insertion events [9, 10, 18].

In this study, we have used the Pet protein as a model system to represent the autotransporter secretion system. This chapter will focus on conserved motifs and how their mutations affect the folding of the autotransporter proteins. These conserved residues are facing the pore of the barrel. Through this study we hope to understand whether these mutations in the conserved residues affect the folding and if so, to what extent [10]? In order to address this important question, this chapter presents a biophysical study to understand the assembly of the autotransporter using the Pet protein as a model system. Previous mutational study of autotransporter protein (Hbp and EspP) showed reduced assembly in *Escherichia coli* and delayed passenger domain translocation respectively [19-21].

Functional parts of the protein required during translocation are shown in Figure 2.1: the signal sequence, passenger domain, the linker region and the β-domain. Autotransporter proteins are synthesised in the cytoplasm and exported across the inner membrane via the secretion (Sec) machinery pathway. Different chaperone proteins in the cytoplasm keep the protein unfolded and keep it from misfolding. The β-domain becomes folded into the inner membrane forming a pore across the outer membrane. The passenger domain is translocated across the outer-membrane and in the case of an autotransporter, is cleaved from the β-barrel.

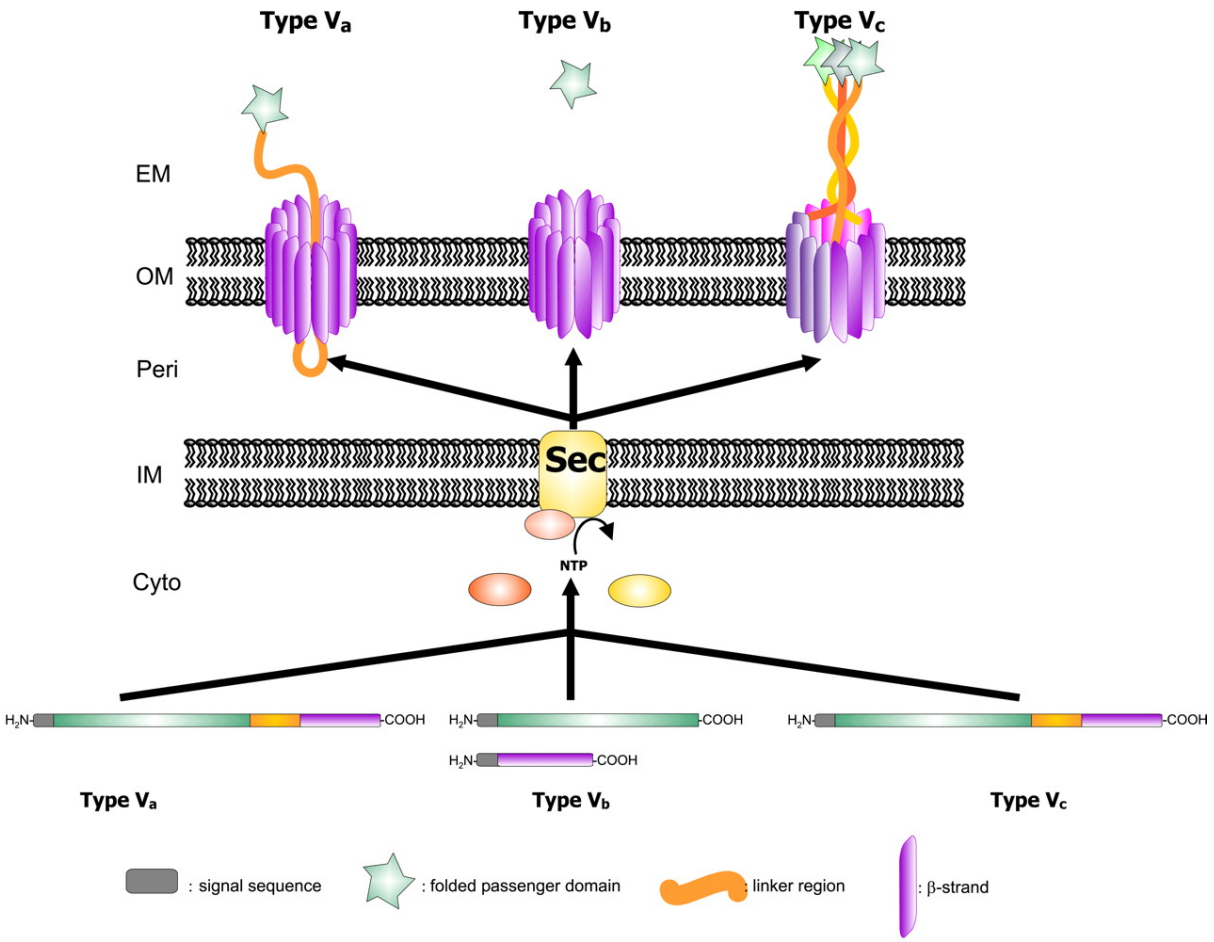


**Figure 2.1. Adapted from [22].** Schematic representation of Type 5 secretion system. Three subdivisions of the Type V secretion system are shown. To the left is the autotransporter proteins secretion system. Functional parts of the protein responsible during the translocation are shown: the signal sequence, passenger domain, the linker region and the β domain. This figure has been reproduced from Henderson et al. **[22].**

## 2.2. Materials and Methods

### 2.2.1 Plasmid construction

The plasmid for this work was provided to us by Dr. Denisse Leyton and Prof. Ian R. Henderson. Further information on the extraction method used is contained within a published paper [10]. pBADPet itself has been described previously [23].

Construct pBADPetG$^{1061}$A, pBADPetG$^{1076}$A, pBADPetG$^{1151}$A and pBADPetY$^{1103}$A, megaprimer PCR was performed as described previously [24, 25] with some variation. Briefly, all round 1 PCRs were performed on 500 ng of template DNA (pBADPet) with 1 µg of the appropriate mutagenesis primer always in combination with 1 µg of primer AatIIRv per 100 µl reaction mixture. Round 1 PCRs were then purified to remove residual primers from the megaprimer synthesized in this first round of amplification. Round 2 PCRs were performed with 4 µg of megaprimer and 1 µg of primer EagIFw on 500 ng of template DNA (pBADPet) per 100 µl reaction mixture. Round 2 amplicons and target vector (pBADPet) were then digested with EagI and AatII and ligated [24, 25).

## 2.2.2 Materials

### 2.2.2.1 Detergent:

N,N-dimethyldodecylamine N-oxide solution (LDAO) ~30% in $H_2O$, and Triton X-100 (>99%) were purchased from Sigma-Aldrich.

### 2.2.2.2 Media

For Luria Bertani (LB) medium, 10 g tryptone, 5 g yeast extract and 10 g NaCl were dissolved in approximately 950 mL deionized water. The pH was adjusted to 7.0 using conc. NaOH. The volume was adjusted to 1 L and the medium was autoclaved.

### 2.2.2.3 Antibiotics

Ampicillin was dissolved at 10 mg/mL in water, filter sterilized (0.2 µm filter) and kept frozen at –20 °C.

#### 2.2.2.4 Marker

Precision Plus®Bi protein dual color standards were purchased from Bio-Rad (Berkeley, California, USA) and used for all sodium dodecyl sulfate-poly(acrylamide) gel electrophoresis (SDS-PAGE) gels unless otherwise stated.

### 2.2.3 Methods

#### 2.2.3.1 Protein expression and purification

A volume of 800 mL of LB was inoculated with starter in a 2 L flask, and incubated at 37°C with stirring at 200 rpm until an optical density at 600 nm (OD600) of 0.3–0.4 in the presence of ampicillin was attained. Cultures were then induced with 0.5 mM IPTG for 4 hours and pelleted at 4200 x g for 15 minutes. Pellets were resuspended in 30 mL buffer 1 (recipe below). 1 mg DNASE, 4 mM $MgCl_2$, and 10 mM DTT were added to each sample, which were then placed in a rotary wheel for 20 min at room temperature. Cells were lysed by sonication and supernatant removed by centrifugation at 10,000 x g for 15 min. Pellets were resuspended in buffer 1 (50 mM Tris-HCl pH 8.0, 0.5% v/v Triton X-100, 100 mM NaCl, 1mM EDTA, 1 mM DTT, 0.2 mM PMSF), and spun at 10,000 x g for 15 min. This step was repeated a total of 3 times. The pellet was resuspended in wash buffer 2 (50 mM Tris-HCl, pH 8, 1 mM EDTA, 1 mM DTT, 0.2 mM PMSF) spun at 10,000 x g for 15 mins and the supernatant discarded. The pellet was resuspended in 50 mM Tris-HCl, pH 8, 8 M urea, 0.5 mM EDTA, 1 mM DTT, and put on rotating wheel for 2 hr at room temperature after which point the sample generally clarified. The sample was spun at 30,000 x g for 30 min and the supernatant discarded. Pellets were stored at –80 °C until further use.

#### 2.2.3.2 Sodium dodecyl sulphate-polyacrylamide gel electrophoresis (SDS-PAGE)

All protein samples were resolved on 12% SDS–poly(acrylamide) gels unless otherwise stated. 12 % SDS gels were prepared using acrylamide (40% acrylamide/Bis solution 29:1, Bio-Rad), stacking buffer comprising 375 mM tris(hydroxymethyl)aminomethane (Tris), pH 6.8, 0.02% SDS and 0.5 mM ethylenediaminetetraacetic acid (EDTA) and separating buffer comprising (375 nM Tris, pH 8.8, 0.1% SDS and 0.5 mM EDTA). The gels were run in a standard SDS running buffer.

#### 2.2.3.3 Immunoblotting

Proteins were transferred to nitrocellulose membranes from SDS-PAGE gels in transfer buffer (25 mM Tris, 190 mM glycine and 10% methanol). Proteins were transferred over the course of 1–1.5 hr. Membranes were blocked using Tris buffered saline containing 0.1% Tween-20 and 5% skim milk. Membranes were incubated with primary antibodies and detected using secondary antibody and enhanced chemiluminescence (ECL) solution. Immediately before the ECL stage, equal volumes of ECL stage 1 and 2 were mixed and added to the membrane. Excess ECL solution was removed, and the membrane was exposed to Fuji X-ray film and developed.

#### 2.2.3.4 sample prep for N-terminal sequencing

Protein samples were folded in LDAO. To achieve this, 0.5 mL of the folding sample (concentration 0.1 mg/mL) was added to a tube containing trypsin at different time points. Samples were then incubated on ice for 20 min, 10 µL of PMSF was added to each tube and then incubated for 5 more minutes on ice. Loading dye was added and the samples were heated at 95°C for 5 minutes. Samples were then analysed by electrophoresis on a

gradient (3–14%) gel at 60–70 V until the dye ran off the gel. N-cyclohexyl-3-aminopropanesulfonic acid (CAPS) buffer was used to transfer the protein onto a polyvinylidene fluoride (PVDF) membrane. The proteins were transferred over the course of about 2 hours at 1 amp. The membrane was then stained using Coomassie brilliant blue. 50% methanol was used to destain the membrane, which was then left overnight at ~4°C in ultrapure water. The bands containing proteins were excised and sequenced using Edman degradation at the Proteomics facility (Monash University).

#### 2.2.3.5 Protein folding

The concentration of unfolded protein (in 8 M urea) was 1 mg/mL. Folding of Petβ-barrel proteins were initiated by 10 × rapid dilution into Tris buffer containing 0.5% v/v LDAO (detergent micelles), to a final concentration of 0.1 mg/mL. All samples were incubated for 24 hr at 37°C and aliquots of the refolding reaction mixture were removed at the following time points: 0, 5, 10, 20, 30, 45 ,60, 120, 240, 360, 480, 600, 960 and 1400 minutes. Samples were boiled, quenched with SDS loading buffer, heated at 100°C and visualized using 12% sodium dodecyl sulphate–polyacrylamide gel electrophoresis (SDS-PAGE) and Coomassie staining. Folded and unfolded protein band intensities were determined by densitometry (see below) and this was achieved in collaboration with Gerard Huysmans at the Pasteur institute. Pet β-barrel folding as a function of time was fit to a double exponential equation and Pet β-barrel G1076A mutant was fit to a single exponential equation.

Some of the folded protein samples were further purified to separate folded from unfolded protein using a Ni affinity column and by gel filtration chromatography using Superdex S200-10/300 (GE healthcare).

### 2.2.4 Biophysical assays

#### 2.2.4.1 Densitometry

Densitometry analysis was performed on the SDS-PAGE gels of the folded/unfolded samples. This was completed to determine the fraction cleaved for each time point (0 min to 24 hrs). I performed all of the folding experiments and SDS-PAGE gels for all the samples (3x for each protein) and the densitometry was performed in collaboration with Gerard Huysmans at the Pasteur institute.

#### 2.2.4.2 Circular dichroism (CD) spectroscopy

A 1 mm path-length fused silica cuvette containing ~0.1 mg/mL protein was used to obtain far-UV circular dichroism (CD) spectra, recorded on a Jasco J-815 Spectropolarimeter. CD scans were recorded from 190 nm to 260 nm at a resolution of 1 nm/step and with an integration time of 1 sec. Background spectra of either 8 M urea, or Tris buffer with LDAO micelles were recorded and subtracted from the obtained protein spectra. Three scans were averaged, and the spectrum was adjusted for buffer contribution. Thermal denaturation of the sample was performed at 218 nm as a function of temperature from 25–100 °C at a thermal gradient of 1°C/min. Spectra were normalized to the mean residue ellipticity. Thermal unfolding was found to be irreversible and so cooling scans were generally not performed. The thermal denaturation CD spectral data shown below were collected by Matthew Johnson. However, I did perform the same experiment at a different time to confirm the results.

#### 2.2.4.3 Fluorescence spectroscopy

All fluorescence spectra were recorded on a Varian Cary Eclipse fluorimeter. Protein samples of ~0.01 mg/mL in a 1 cm path-length cuvette were excited with photons of $\lambda$ = 295 nm (5 nm bandwidth) and emission was recorded from 300 nm to 500 nm, with an integration time of 0.1 sec. Similarly to CD spectroscopy, background spectra for the dissolving media were recorded and subtracted in the analysis. The fluorescence signal seen in the emission spectra is interpreted to arise from the excitation of tryptophan residues.

## 2.3 Results

### 2.3.1 Pet β-barrel protein folding, a schematic representation

Figure 2.2 a shows a schematic representation of Pet β-barrel folding in the outer membrane of Gram-negative bacteria. The location of the conserved residues is highlighted in green. The white shaded residues in Figure 2.2a points towards the barrel lumen and the yellow shaded residues points towards the lipid bilayer. The boxed residues are the Tryptophan (W) residues, and these were used to obtain folding information via fluorescence spectroscopy. Figure 2.2a also shows extracellular loops (L1–L6) and periplasmic turns (T1–T5). The loops are exposed in the extracellular space of the bacterial envelope. Figure 2.2b shows the mutated glycine residues and their location. This investigation centres on a mutational study of PetβG$^{1061}$A and PetβG$^{1076}$A wherein glycine residues have been mutated to alanine in order to determine their role in folding. The glycine residues are across from the aromatic residue (strand 1 and 2, strand 3 and 4). These glycine residues accommodate

the aromatic residue, but we seek to discover how this changes if the glycine residue is mutated to an alanine residue. Will this mutation be silent or have a direct impact in protein folding?

The full length Pet protein is 136 kDa, of which, 30 kDa is the β-domain and 106 kDa is the passenger domain. For this study, we truncated the passenger domain and synthesised a protein of total mass of 43 kDa (Figure 2.2 c). All of the different molecules synthesised are the same overall size, but two of them are mutated and one is the wild type. Pet $^{\Delta 1\text{-}902}$ is the wild type, where Δ1-902 indicates that the first 902 residues of the passenger domain are deleted. Pet $^{\Delta 1\text{-}902}G^{1061}A$ and Pet $^{\Delta 1\text{-}902}G^{1076}A$ (Figure 2.2 c) are mutated versions of the wild type, where 1061 and 1071 are the position in the protein sequence of the residues on the full length Pet protein that were mutated from glycine to alanine.

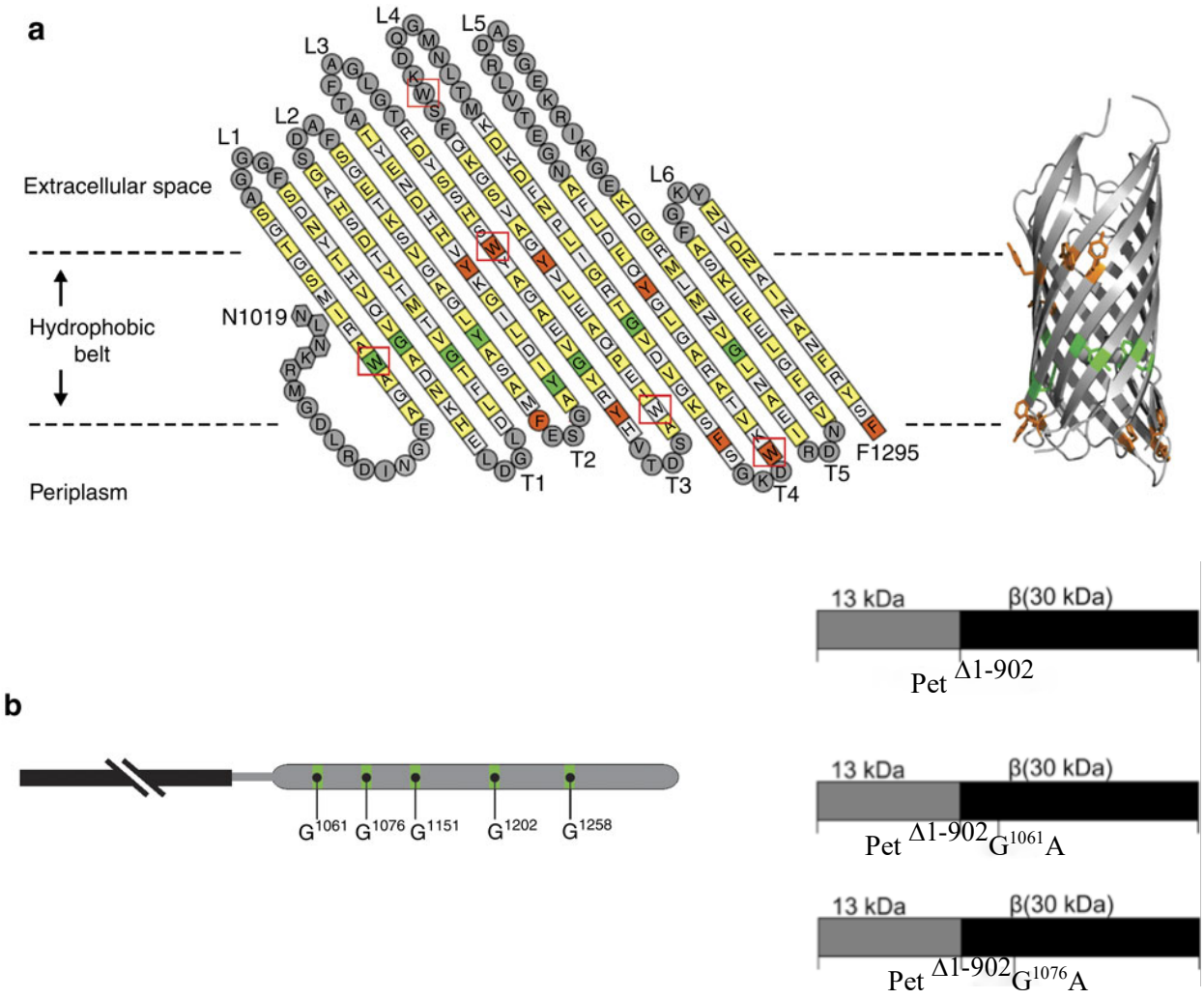


**Figure 2.2.** Reproduced from Leyton *et al.* 2014[10]. Pet β-barrel protein folding, a schematic representation. Conserved residues are shown in Green. The protein is a 43 kDa Pet β-barrel; the barrel is 30 kDa (passenger domain not shown in this representation). Yellow squares represent residues with side chains pointing towards the lipid bilayer and white squares represent residues with side chains pointing towards the barrel lumen. Red squared glycine residues indicate the mutation, G → A [10].

### 2.3.2 Pet $^{\Delta 1\text{-}902}$, Pet $^{\Delta 1\text{-}902}$G$^{1061}$A and Pet $^{\Delta 1\text{-}902}$G$^{1076}$A folding in LDAO micelles

Pet $^{\Delta 1\text{-}902}$, Pet $^{\Delta 1\text{-}902}$G$^{1061}$A and Pet $^{\Delta 1\text{-}902}$G$^{1076}$A were expressed using bacterial plasmid expression, and were provided for this study by Dr. Denisse Leyton and Prof. Ian

Henderson. These proteins contain the barrel domain and 116 residues of the passenger domain immediately proximal to the N-terminus of the barrel domain. These proteins were denatured in urea and refolded by 10x rapid dilution in the refolding buffer that contained 0.5% LDAO micelles [26]. Autocatalytic cleavage of the passenger domain is one of the characteristics of the autotransporter, and this process relies on a correctly positioned linker segment within the β-barrel pore. The passenger domain is cleaved between asparagine residues $N^{1018}$ and $N^{1019}$. The catalytic cleavage of the passenger domain can be used as a readout to signify correct folding of the barrel. This property is henceforth used to understand the folding of Pet proteins.

Unfolded Pet 116β (wild-type and 58 mutant) migrated during electrophoresis with an apparent molecular mass of 43 kDa (including the small fragment of passenger domain) while the folded and cleaved barrel (wild-type and 58 mutant) migrated at 30 kDa because the passenger domain cleaved autoproteolytically. Autoproteolytic cleavage of the passenger domain is an indication of a correctly folded (native like) barrel. The efficiency of the refolding reaction was monitored by the appearance of the 30kDa β-barrel fragment in the SDS-PAGE test. The folded and unfolded protein samples were quantified using densitometry analysis. The folded fraction was calculated by dividing the intensity of the folded band by the sum of the intensities of both the folded and unfolded bands. After folding was initiated, aliquots of the reaction were removed and quenched with SDS loading buffer at the following time points: 0, 5, 10, 20, 30, 45, 60, 120, 240, 360, 480, 600, 960 and 1400 minutes. The folded fraction for each time point was determined using SDS-PAGE and densitometry as described above. The folding kinetics were fit to single or double exponential equations.

Densitometry analysis showed that, after 24 hours of folding, both Pet $^{\Delta 1\text{-}902}$ and Pet $^{\Delta 1\text{-}902}G^{1076}A$ refolded with similar efficiencies (46 ± 3% and 35 ± 1% respectively). Even

though the overall folding efficiency after 24 hours was similar in both molecules, the kinetics were quite different and indeed complicated in the case of Pet $^{\Delta 1\text{-}902}$. Cleavage of the passenger domain commenced within the dead time of the experiment (that is, during mixing of the denatured protein with the folding buffer, also known as the burst phase). About 13% cleavage was achieved within the dead time of the experiment. The rest of the folding followed exponential kinetics with two clearly different phases. A significant proportion (~22%) of the protein was cleaved with a faster rate constant of 0.13 ± 0.001 $min^{-1}$. However, Pet $^{\Delta 1\text{-}902}G^{1076}A$ cleavage was slower and could be represented by a single exponential process with a rate constant of 0.004 ± 0.001 $min^{-1}$. This could indicate the folding to the native structure is rate limiting over the slow path, or that a small amount of the protein is misfolded. We monitored protein folding by CD and tryptophan fluorescence spectroscopy along with limited proteolysis to determine if the slow appearance of the passenger domain has anything to do with the barrel folding.

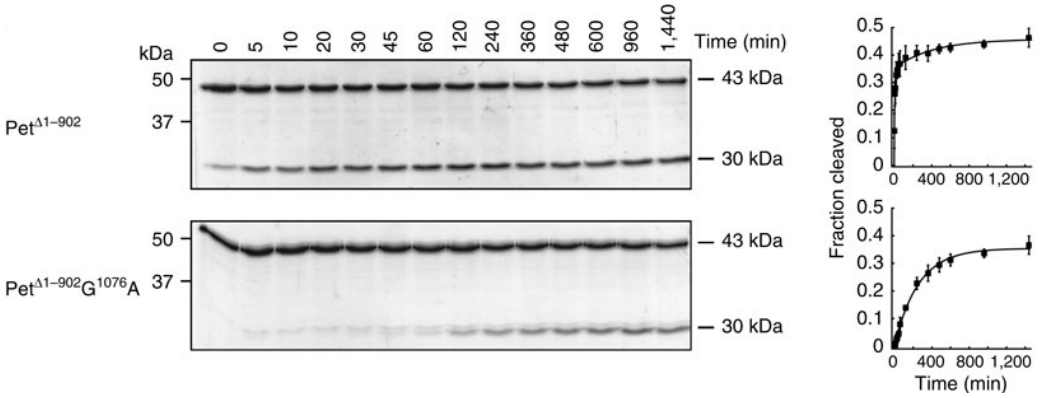


**Figure 2.3.** Electrophoretic analysis of Pet $^{\Delta 1\text{-}902}$ and Pet $^{\Delta 1\text{-}902}G^{1076}A$ refolding. Native folding of Pet protein is confirmed by the appearance of cleaved 30 kDa (β-barrel) as shown in the Figure [10]. Data shown here is the average of three experiments and the error bars corresponds to the standard deviation.

Insertion and folding of different variant of Pet proteins into LDAO micelles. The folding was monitored by the appearance of the autocatalytically cleaved 30kDa (β-barrel) vs the uncleaved 43 kDa form of Pet. Densitometry analysis was performed and plotted as a

function of time. The fraction cleaved obtained from the densitometry data were plotted and fitted to single or double exponential functions.

To compare the secondary structure of Pet $^{\Delta 1\text{-}902}$ and Pet $^{\Delta 1\text{-}902}G^{1076}A$, the conformational properties were examined using far UV circular dichroism and tryptophan fluorescence spectroscopies.

The far- UV CD spectra of Pet $^{\Delta 1\text{-}902}$ and Pet $^{\Delta 1\text{-}902}G^{1076}A$ (Figure 2.4) showed similar signals corresponding to characteristic β-sheet with minima at ~ 218 nm, whereas there was no secondary structure of the molecules when unfolded in urea. Secondary structure acquisition was very rapid, and appeared to occur mostly within the dead time of the experiment. Spectra taken at the beginning of the experiment and after 24 hours are very similar, indicating only very minor differences that could be due to light scattering effects at very low wavelength. Both traces exhibit a minimum at 218 nm, consistent with the protein folding to a predominantly β-sheet conformation, which is absent in the spectrum of unfolded Pet $^{\Delta 1\text{-}902}$ and Pet $^{\Delta 1\text{-}902}G^{1076}A$.

To better understand the folding of Pet proteins in a hydrophobic lipid-like environment, detergent micelles were employed as model amphiphilic system with a hydrophobic space. There are 5 tryptophan residues in the transmembrane domains of Pet protein. Tryptophan residues in the outer membrane proteins typically form aromatic girdles around the protein, located in the interfacial regions of the bilayer. Burial of 4 tryptophan residues upon refolding of Pet $^{\Delta 1\text{-}902}$ and Pet $^{\Delta 1\text{-}902}G^{1076}A$ and its insertion into detergent micelles would be expected to cause a change in the intensity and a blue shift of the fluorescence emission maximum. Rapid folding of the proteins (β-barrel) was confirmed with Tryptophan fluorescence spectroscopy in detergent micelles as well. As expected, the fluorescence emission spectra of Pet $^{\Delta 1\text{-}902}$ and Pet $^{\Delta 1\text{-}902}G^{1076}A$ refolded into LDAO (detergent micelles) were characterised by a substantial increase in fluorescence intensity

and a shift in the emission maximum. The unfolded proteins were characterised by relatively low intensity and a maximum emission wavelength at around 355 nm, which indicates that the tryptophan residues were solvent exposed [10].

The fluorescence spectra suggest that the tryptophan residues in Pet $^{\Delta 1\text{-}902}$ adopted their native state within the dead time of the experiment, which led to very similar spectra at 0 min and at 24 hours. Pet $^{\Delta 1\text{-}902}G^{1076}A$ also had a rapid shift within the experimental dead time, though the intensity was lower than Pet $^{\Delta 1\text{-}902}$ at 24 hours. The maximum emission wavelength of Pet $^{\Delta 1\text{-}902}G^{1076}A$ remained red shifted at 339 nm compared to 334 nm in Pet $^{\Delta 1\text{-}902.}$ This indicates that the tryptophan residues in the two proteins are in two different environments. These data suggest that the conformation of the two proteins is not the same, and that the conformations of Pet $^{\Delta 1\text{-}902}$ and Pet $^{\Delta 1\text{-}902}G^{1076}A$ could be distorted.

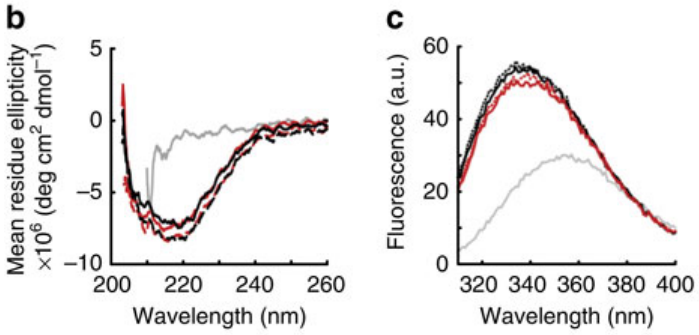


**Figure 2.4** Far UV CD spectra (left panel) and tryptophan fluorescence spectra (right panel). Spectra of unfolded (grey). folded Pet $^{\Delta 1\text{-}902}$ (black) and Pet $^{\Delta 1\text{-}902}G^{1076}A$ (red) at t=0 min (full lines) and at t=8 hr (dashed lines). Data shown here is the average of 3 set of experiments. This figure has been reproduced from Leyton et al.[10].

We further investigated the folded Pet $^{\Delta 1\text{-}902}$ and Pet $^{\Delta 1\text{-}902}G^{1076}A$ using limited treatment with trypsin. Protein samples at different timepoints during folding were digested with trypsin for 20 min, which generated a set of proteolytic products. In the case of Pet $^{\Delta 1\text{-}902}$ at ~ 0 min, trypsinolysis generated two fragments of 30 and 26 kDa (Figure 2.5) and also 25 and 24 kDa

(a fingerprint). This result suggests that the exposed arginine and lysine residues were cleaved by trypsin. However, the digestion of Pet $^{\Delta 1\text{-}902}G^{1076}A$ in the early stages of folding generated a dominant set of 25/24 kDa fragments and a ladder of larger fragments. This delay in the appearance of the 30 kDa fragment supports the fluorescence and SDS-PAGE data. This results in the delayed self-cleavage where the high molecular weight fragments are due to the truncated forms of 43 kDa Pet $^{\Delta 1\text{-}902}$. The passenger domain is still attached to the barrel and some of the passenger domain gets digested by trypsin.

N-terminal sequencing of these limited proteolysis fragments revealed that the 30, 26, 25 and 24 kDa sections of Pet $^{\Delta 1\text{-}902}$ (Fig 2.5) all start in the cleavage with the sequence $N^{1019}$LNKRM. The N-terminal sequence of Pet $^{\Delta 1\text{-}902}G^{1076}A$ is also initiated at N1019, which points to the autocatalytic cleavage of the barrel domain. The 25/24 kDa fragments (Figure 2.5) of Pet $^{\Delta 1\text{-}902}G^{1076}A$ initiate from I1040 within the first transmembrane β-strand. This suggests that the barrel domain was not folded in its native conformation, otherwise it would not be accessible to trypsin, but rather that the mutant barrel adopts a non-native conformation.

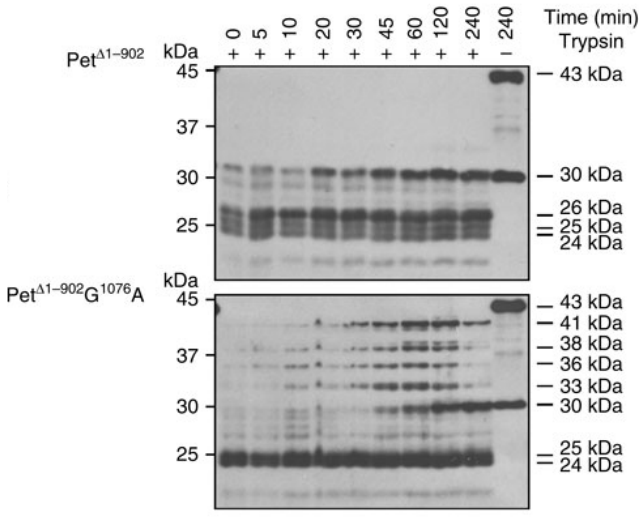


**Figure 2.5** Folding of Pet $^{\Delta 1\text{-}902}$ and Pet $^{\Delta 1\text{-}902}G^{1076}A$ samples digested with trypsin in order to look at the different resistant fragments. Samples were analysed by SDS-PAGE and

immunoblotted with anti-barrel domain antibodies [10]. This figure has been reproduced from Leyton et al. [10].

### 2.3.3 β-barrel heat modifiability:

Pet β-barrel and mutants were expressed in the form of inclusion bodies in *E. coli*, which were solubilized in urea. We first examined the folding of the protein by SDS-PAGE. It has been known that some outer membrane proteins share a specific characteristic known as heat modifiability [27, 28]. During electrophoresis, the folded Pet protein migrates to a different position compared to the unfolded analogue in unboiled SDS-PAGE samples. However, when Pet proteins are boiled prior to electrophoresis, previously folded protein migrates to the same position as the unfolded protein. Thus, SDS-PAGE can distinguish between folded and unfolded Pet β-barrel proteins. Adding SDS loading buffer, this captures the folded and unfolded populations present in solution. During electrophoresis, these two-protein conformations migrate to different positions when outer membrane β-barrel protein shows heat modifiability. The Pet $^{\Delta 1\text{-}902}$ showed heat modifiability whereas the refolded Pet $^{\Delta 1\text{-}902}G^{1076}A$ (Fig, 2.6) barrel appeared completely denatured under the same conditions. Thermal unfolding was also recorded in CD to monitor changes in the β-sheet at 218 nm. These data (Figure 2.6) indicate that Pet $^{\Delta 1\text{-}902}G^{1076}A$ is less stable than Pet $^{\Delta 1\text{-}902}$. This strongly suggests that the Pet $^{\Delta 1\text{-}902}G^{1076}A$ does not fold to its native state like Pet $^{\Delta 1\text{-}902}$.

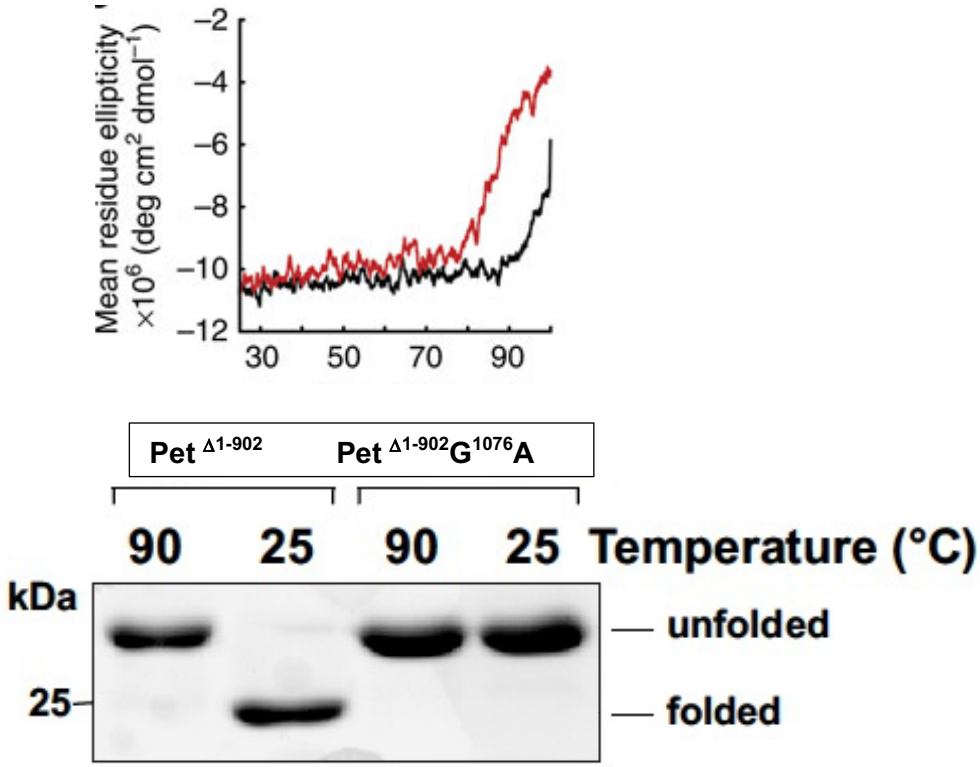


**Figure 2.6** Thermal denaturation of folded Pet protein (upper panel). Proteins were purified using gel filtration. Pet $^{\Delta 1\text{-}902}$(black) and Pet $^{\Delta 1\text{-}902}G^{1076}A$ (red). (lower panel) Cleaved protein purified to separate folded and unfolded states. Folded samples were separated and run on SDS-PAGE. Pet $^{\Delta 1\text{-}902}$ shows heat modifiability evidenced by increased migration of the folded beta barrel. Pet $^{\Delta 1\text{-}902}G^{1076}A$ does not show heat modifiability. Data shown here is the average of 3 different experiments. This figure has been reproduced from leyton et al. [10].

### 2.3.4. Gel filtration of folded Pet protein

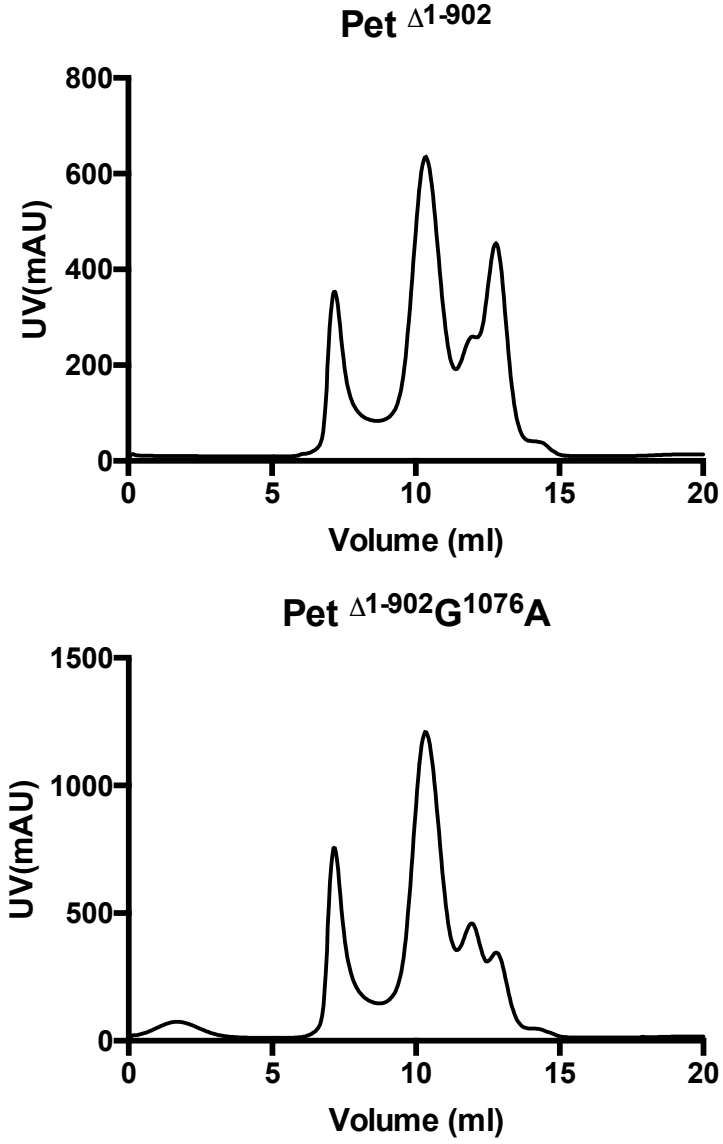


**Figure 2.7** Chromatogram produced from gel filtration experiment for Pet $^{\Delta 1\text{-}902}$ (top panel). It is evident that the peaks are closely spaced and it was not possible to separate a lot of the folded and unfolded protein. The first peak in both chromatograms is the void volume. Chromatogram for gel filtration of Pet $^{\Delta 1\text{-}902}G^{1076}A$ (lower panel). Peaks are closely spaced making it challenging to separate a lot of the folded proteins.

Gel filtration was used to separate folded Pet protein molecules from unfolded ones. Superdex S200 was used to separate the samples, and Figure 2.7 shows the chromatogram for both Pet $^{\Delta 1\text{-}902}$ and Pet $^{\Delta 1\text{-}902}G^{1076}A$. The first peak in both chromatograms (Figure 2.7) is from the void volume of the column being used. In general, the larger the molecule, the faster it moves through the column because it tends to not traverse through the pores within the resins in the column.

In this case, the unfolded protein runs at 43 kDa and folded, cleaved protein runs at about 30kDa. This suggests that the 43 kDa sized protein will move faster through the column. One of the issues with the collection of these data was the elution of the folded and the unfolded protein were very close to each other. However, we were able to collect enough folded protein to run thermal denaturation of protein using circular dichroism.

### 2.3.4. Folding of Pet $^{\Delta 1\text{-}902}G^{1061}A$

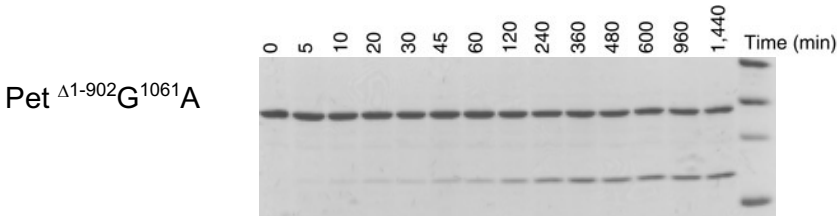


**Figure 2.8** 0 min to 24 hours folding and the folding of Pet $^{\Delta 1\text{-}902}G^{1061}A$. The folded and cleaved barrel appears early on and the folding efficiency is much closer to Pet $^{\Delta 1\text{-}902}$ than to the Pet $^{\Delta 1\text{-}902}G^{1076}A$. That's one of the reasons this was not further investigated.

One further mutant of the Pet protein was explored: Pet $^{\Delta 1\text{-}902}G^{1061}A$, although this generated far less interesting data than for those shown in the previous sections. The same panel of experimental tests were performed as for the other folding experiments. SDS-PAGE analysis (Figure 2.8) showed that the folding rate is very close to wild type, and mutation at this position did not appear to disrupt the folding process.

The mutation of $G^{1061}A$ seems to be not as disruptive as the mutation of $G^{1076}A$. The $G^{1061}A$ mutation was in the second transmembrane strand and it is hypothesised that locational difference meant that it did not have as much of an effect in protein folding compared to the mutation in the fourth transmembrane strand. Since the folding efficiency was close to that of the wild type Pet $^{\Delta 1\text{-}902}$, this mutant was not investigated further.

## 2.4 Discussion

In this chapter, we reported the kinetic analysis, stability, and the secondary structure of Pet $^{\Delta 1\text{-}902}G^{1061}A$ was explored in order to address the role of some of the conserved residues within the β-barrel domain in folding and stability of Pet proteins. In order to understand the thermal and kinetic stability of Pet β-barrel protein and its variants, it was necessary to fold the protein to its functional form. Previous studies had shown that an outer membrane protein (OmpA) could be successfully folded in the detergent micelles and liposomes. Our experiments were designed in a similar fashion, where it was demonstrated that cleavage of the passenger domain can be used to confirm the native conformation of the Pet proteins. In line with OmpA protein folding, the folding process here did not require a significant amount of urea in the refolding buffer: final refolding yields of Pet $^{\Delta 1\text{-}902}$ and Pet $^{\Delta 1\text{-}902}G^{1076}A$ were 46% and 35% respectively, which are not significantly different.

However, there *was* a significant difference in the kinetic pathways of protein folding. In the case of of Pet $^{\Delta 1\text{-}902}$, the kinetic pathway was described by double exponential function after the burst phase. The majority (22%) of proteins were cleaved with a faster rate constant, 13% were already folded in the burst phase and ~11% were cleaved with a slower rate. Pet $^{\Delta 1\text{-}902}G^{1076}A$ (mutated) cleavage was described by a single exponential function with a rate constant of 0.004 $min^{-1}$. Formation of native structure is limited over the slow phase and Pet $^{\Delta 1\text{-}902}G^{1076}A$ most likely does not have a native conformation which impaired

the cleavage compared to the native folded pet protein. Far UV-CD spectra showed very little difference in secondary structure of Pet $^{\Delta 1\text{-}902}$ and of Pet $^{\Delta 1\text{-}902}G^{1076}A$, which means they both achieve β-sheet structure to a very similar extent.

However, the tryptophan fluorescence data suggested there is a difference in the structure between the two Pet proteins used in this study. Tryptophan residues are buried in the β-barrel domain and these residues are excited to obtain fluorescence spectra, and these gives us more accurate state and their surroundings. Since these tryptophan residues are spread out within the structure, the difference in fluorescence spectra of Pet $^{\Delta 1\text{-}902}$ and Pet $^{\Delta 1\text{-}902}G^{1076}A$ confirms the difference in their structure.

Limited treatment of folding sample at different time points with trypsin generated different sets of footprints. Trypsin cannot access the part of protein that is folded in the LDAO. It targets the part of the protein that is exposed and only recognizes certain residues to digest. Pet $^{\Delta 1\text{-}902}$ had dominant fragments at ~ 30 kDa (size of the β-barrel) and 26 kDa and two other fragments at 25kDa and 24 kDa. However, Pet $^{\Delta 1\text{-}902}G^{1076}A$ generated dominant fragments initially at 25 and 24 kDa. There was a delay in the appearance of 30 kDa fragment which was present in case of Pet $^{\Delta 1\text{-}902}$ at t=0. This obviously suggests that the β-barrel folding is not native because there is no cleavage of the passenger domain at t=0 (dead time of the experiment). To further understand the folding and the cleavage, N-terminal sequencing was undertaken (through the Monash proteomics facility). N-terminal sequence revealed all fragments (30, 26, 25 and 24 kDa) of Pet $^{\Delta 1\text{-}902}$ generated during trypsinolysis were cleaved at the site sequence $N^{1019}$LNKRM. The 30 kDa fragment of Pet $^{\Delta 1\text{-}902}G^{1076}A$ also started at the same sequence. However, 25/24 kDa forms initiated the cleavage at $I^{1040}$ within the first transmembrane sequence. If β-barrel domain was folded in its native state $I^{1040}$ residue would not be accessible for trypsin to cleave.

There has been further study on the Pet barrel domain stability and pet translocation by Dr. Denisse Leyton [14]. Microbiology assays have been used to further understand the stability and additional mutational studies have been undertaken as well.

Results discussed in this chapter indicate that conserved motifs promote efficient folding of an autotransporter protein. According to these results and those presented in Leyton *et al.* [10], the removal of conserved residues increases misfolding of the protein as shown by trypsin assay, N-terminal sequencing, and also the decrease in thermal stability.

## 2.5 References


1. Daggett, V. and A. Fersht, The present view of the mechanism of protein folding. Nat Rev Mol Cell Biol, 2003. **4**(6): p. 497-502.
2. Lindorff-Larsen, K., *et al.*, Protein folding and the organization of the protein topology universe. Trends Biochem Sci, 2005. **30**(1): p. 13-9.
3. Tamm, L.K., H. Hong, and B. Liang, Folding and assembly of beta-barrel membrane proteins. Biochim Biophys Acta, 2004. **1666**(1-2): p. 250-63.
4. Desvaux, M., *et al.*, Secretion and subcellular localizations of bacterial proteins: a semantic awareness issue. Trends Microbiol, 2009. **17**(4): p. 139-45.
5. Wimley, W.C., Toward genomic identification of beta-barrel membrane proteins: composition and architecture of known structures. Protein Sci, 2002. **11**(2): p. 301-12.
6. Fan, E., *et al.*, Type V Secretion Systems in Bacteria. Microbiol Spectr, 2016. **4**(1).
7. Desvaux, M., N.J. Parham, and I.R. Henderson, Type V protein secretion: simplicity gone awry? Curr Issues Mol Biol, 2004. **6**(2): p. 111-24.
8. Leo, J.C., I. Grin, and D. Linke, Type V secretion: mechanism(s) of autotransport through the bacterial outer membrane. Philos Trans R Soc Lond B Biol Sci, 2012. **367**(1592): p. 1088-101.
9. Yuan, X., *et al.*, Molecular basis for the folding of beta-helical autotransporter passenger domains. Nat Commun, 2018. **9**(1): p. 1395.
10. Leyton, D.L., *et al.*, A mortise-tenon joint in the transmembrane domain modulates autotransporter assembly into bacterial outer membranes. Nat Commun, 2014. **5**: p. 4239.
11. Leyton, D.L., A.E. Rossiter, and I.R. Henderson, From self sufficiency to dependence: mechanisms and factors important for autotransporter biogenesis. Nat Rev Microbiol, 2012. **10**(3): p. 213-25.
12. Hussain, S. and H.D. Bernstein, The Bam complex catalyzes efficient insertion of bacterial outer membrane proteins into membrane vesicles of variable lipid composition. J Biol Chem, 2018. **293**(8): p. 2959-2973.
13. Sikdar, R., *et al.*, Folding of a bacterial integral outer membrane protein is initiated in the periplasm. Nat Commun, 2017. **8**(1): p. 1309.
14. Junker, M., *et al.*, Pertactin beta-helix folding mechanism suggests common themes for the secretion and folding of autotransporter proteins. Proc Natl Acad Sci U S A, 2006. **103**(13): p. 4918-23.
15. Roman-Hernandez, G., J.H. Peterson, and H.D. Bernstein, Reconstitution of bacterial autotransporter assembly using purified components. Elife, 2014. **3**: p. e04234.
16. Ruiz-Perez, F., I.R. Henderson, and J.P. Nataro, Interaction of FkpA, a peptidyl-prolyl cis/trans isomerase with EspP autotransporter protein. Gut Microbes, 2010. **1**(5): p. 339-344.
17. Ruiz-Perez, F., *et al.*, Roles of periplasmic chaperone proteins in the biogenesis of serine protease autotransporters of Enterobacteriaceae. J Bacteriol, 2009. **191**(21): p. 6571-83.
18. Celik, N., *et al.*, A bioinformatic strategy for the detection, classification and analysis of bacterial autotransporters. PLoS One, 2012. **7**(8): p. e43245.
19. Yen, Y.T., *et al.*, Common themes and variations in serine protease autotransporters. Trends Microbiol, 2008. **16**(8): p. 370-9.
20. Yen, Y.T., *et al.*, Importance of conserved residues of the serine protease autotransporter beta-domain in passenger domain processing and beta-barrel assembly. Infect Immun, 2010. **78**(8): p. 3516-28.

21. Pavlova, O., *et al.*, Mechanistic link between β barrel assembly and the initiation of autotransporter secretion. Proceedings of the National Academy of Sciences, 2013: p. 201219076.
22. Henderson, I.R., *et al.*, Type V protein secretion pathway: the autotransporter story. Microbiol Mol Biol Rev, 2004. **68**(4): p. 692-744.
23. Leyton, D.L., *et al.*, The unusual extended signal peptide region is not required for secretion and function of an Escherichia coli autotransporter. FEMS Microbiol Lett, 2010. **311**(2): p. 133-9.
24. Leyton, D.L., *et al.*, Size and conformation limits to secretion of disulfide-bonded loops in autotransporter proteins. J Biol Chem, 2011. **286**(49): p. 42283-91.
25. Sarkar, G. and S.S. Sommer, The "megaprimer" method of site-directed mutagenesis. Biotechniques, 1990. **8**(4): p. 404-7.
26. Zhai, Y., *et al.*, Autotransporter passenger domain secretion requires a hydrophobic cavity at the extracellular entrance of the beta-domain pore. Biochem J, 2011. **435**(3): p. 577-87.
27. Inouye, M. and M.L. Yee, Homogeneity of envelope proteins of Escherichia coli separated by gel electrophoresis in sodium dodecyl sulfate. J Bacteriol, 1973. **113**(1): p. 304-12.
28. Nicolay, T., *et al.*, Probing the applicability of autotransporter based surface display with the EstA autotransporter of Pseudomonas stutzeri A15. Microb Cell Fact, 2012. **11**: p. 158.

# Chapter 3. Different factors affecting Pet protein folding

## 3.1. Introduction

In the previous chapter, β-barrel protein folding in LDAO detergent micelles was explored. Mutational studies in the barrel region of the Pet protein showed that sequence changes in this region can lead to inefficient and misfolding [1, 2]. As seen in the SDS-PAGE data, CD spectra and fluorescence spectra, folding of the beta barrel protein is apparently rapid and spontaneous [1, 3]. Changes in tryptophan fluorescence result from the burial of these residues in the hydrophobic environment of the micelle, and this has been used to study the kinetics of Pet protein [3-5].

Armed with this knowledge, in this chapter, a range of different factors affection Pet protein folding are studied. The full-length Pet protein is 136 kDa, of which 30 kDa is the β-domain and 106 kDa is the passenger domain [6, 7]. The previously studied protein had a truncated (13 kDa) version of the passenger domain (see Figure 3.1). For this study however, we used protein constructs containing longer passenger domain including a full-length pet protein (Pet 966β). Pet 232 β contains a barrel domain that is 30 kDa and ~36 kDa of passenger domain. Pet 464β contains a barrel domain that is 30 kDa and ~72 kDa of passenger domain (see Figure 3.1). Pet 966β is a full-length protein and contains 30 kDa of β-barrel and ~ 106 kDa of passenger domain [7]. In addition to these protein constructs, we also studied folding of passenger domain only to understand protein folding in the absence of the beta barrel domain in the outer membrane protein.

In this chapter, we studied protein folding at lower temperatures (15 and 4° C) in order to slow down the kinetics of protein folding and get useful information on the dynamics and progress of this process [8]. Folded protein samples (all versions including the full-length pet protein and passenger domain only) were digested with trypsin to test the folded protein's

resistance to this process [9-11]. If folded in its native state, most of the protein is purportedly inaccessible to trypsin [9]. When such proteins are not folded in their native state, trypsin can cleave proteins at certain sites (mostly C-terminal sites of lysine and arginine residues) and generates a fingerprint of characteristic fragments [1].

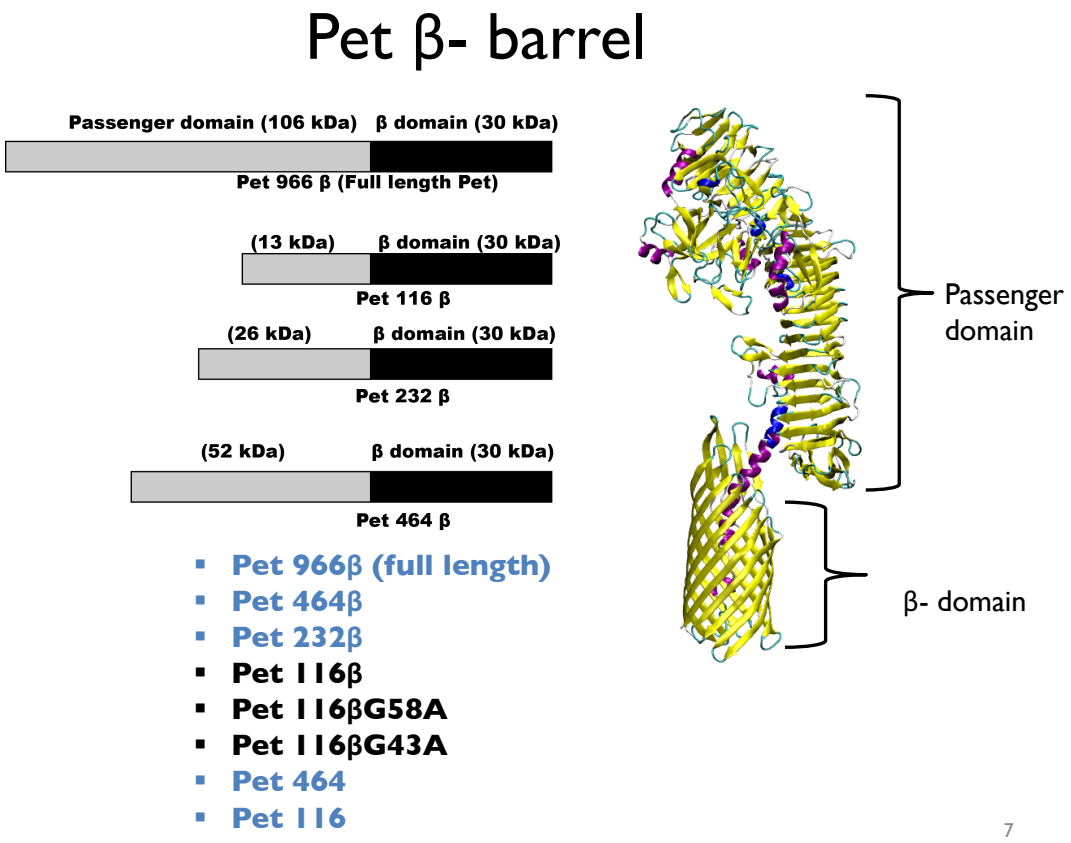


**Figure 3.1.** Schematic representation comparing the proteins explored in Chapters 1 and 2. Ultimately, we studied the folding of the passenger domain of Pet protein in the absence of the β-barrel domain as a comparative case.

## 3.2. Materials and Methods

### 3.2.1 Materials

The following protein constructs were used for this study:

- Pet 116β : 30 kDa β-barrel, 13kDa Passenger domain (116 residues)

- Pet 232β : 30 kDa β-barrel, 26 kDa Passenger domain (232 residues)
- Pet 464β : 30 kDa β-barrel, 52 kDa Passenger domain (464 residues)
- Pet 966β (full length pet protein): 30 kDa β-barrel, 106 kDa Passenger domain (966 residues)

#### 3.2.1.1 Detergent

N,N-dimethyldodecylamine N-oxide solution (LDAO) ~30% in $H_2O$ and Triton X-100 (>98%) were purchased from Sigma-Aldrich and used as received.

#### 3.2.1.2 Media

For Luria–Bertani medium (LB), 10 g tryptone, 5 g yeast extract and 10 g NaCl were dissolved in approximately 950 mL deionized water. The pH was adjusted to 7.0 with concentrated NaOH. The volume was adjusted to 1 L and the medium was autoclaved.

#### 3.2.1.3 Antibiotics

Ampicillin was solubilized up to 10 mg/mL in water, filter sterilized (0.2 μm filter) and frozen at –20 °C.

#### 3.2.1.4 Marker

Precision plus protein dual color standards were purchased from Bio-rad and used for all SDS-PAGE gels unless otherwise stated.

### 3.2.2 Methods

#### 3.2.2.1 Protein expression and purification

To begin the process, 800 mL of LB was inoculated with starter in a 2 L flask, incubated at 37 °C, with stirring at 200 rpm to OD600 = 0.3–0.4 in the presence of ampicillin. This was then induced with 0.5 mM IPTG for 4 hours. Cells were pelleted at 4200×g for 15 minutes. Pellets were resuspended in 30 mL of buffer 1 (recipe below). To each sample was

added 1 mg DNASE, 4 mM $MgCl_2$ and 10 mM DTT. Samples were placed on a rotary wheel for 20 min at room temperature. Cells were lysed by sonication, and the supernatant was collected after centrifugation at 10,000×g for 15 min. Pellets were resuspended in buffer 1 (50 mM Tris-HCl, pH 8.0, 0.5% v/v Triton X-100, 100 mM NaCl, 1 mM EDTA, 1 mM DTT, 0.2 mM PMSF), and again spun at 10,000×g for 15 min. This last step was repeated a total of 3 times. The final collected pellet was resuspended in wash buffer 2 (50 mM Tris-HCl, pH 8, 1 mM EDTA, 1 mM DTT, 0.2 mM PMSF) spun at 10,000×g for 15 mins and the supernatant discarded. The pellet was resuspended in 50 mM Tris-HCl, pH 8, 8 M urea, 0.5 mM EDTA, 1 mM DTT. This was put on rotating wheel for 2 hr at room temperature, after which the sample usually became optically clear. Finally, the sample was centrifuged at 30,000×g for 30 min, and the supernatant was discarded. The pellet was stored at –80 °C until use.

#### 3.2.2.2 Sodium dodecyl sulphate-polyacrylamide gel electrophoresis (SDS-PAGE)

All protein samples were resolved on 12% SDS polyacrylamide gels unless otherwise stated. 12 % SDS gel was prepared using acrylamide (40% 29:1, Bio-rad), stacking buffer (375 mM Tris, pH 6.8, 0.02% SDS and 0.5 mM EDTA) and separating buffer (375 mM Tris pH 8.8, 0.1% SDS and 0.5 mM EDTA). The gels were run in a standard 1 × SDS running buffer. The composition used for 10× SDS PAGE running buffer was 30.0 g of Tris base, 144.0 g of glycine and 10.0 g of SDS in 1000 mL of $H_2O$.

#### 3.2.2.3 Immunoblotting

Proteins were transferred to nitrocellulose membranes from SDS-PAGE gels in transfer buffer (25 mM Tris, 190 mM glycine and 10% methanol) over the course of 1 to 1.5 hr. Membranes were blocked using Tris buffered saline containing 0.1% Tween-20 and 5% skim milk. Membranes were incubated with primary antibodies, and detection was achieved using secondary antibody and ECL solution. Immediately before this, equal volumes of ECL 1 and 2 were mixed and added to the membrane. Excess ECL solution was removed, and the membrane was exposed to Fuji X-ray film and developed.

#### 3.2.2.4 Protein folding

The concentration of unfolded protein (in 8 M urea) was 1 mg/mL. Folding of Petβ-barrel proteins was initiated by 10× rapid dilution into Tris buffer containing 0.5% LDAO (detergent micelles) v/v, at a final concentration of 0.1 mg/mL. All samples were incubated for 24 hr at 37 °C and aliquots of refolding reaction mixture were removed at the following time points: 0, 5, 10, 20, 30, 45, 60, 120, 240, 360, 480, 600, 960, 1400 minutes. Samples were boiled, quenched with SDS loading buffer, heated at 100 °C and visualized using 12 % sodium dodecyl sulphate–polyacrylamide gel electrophoresis (SDS-PAGE) and Coomassie staining. Folded and unfolded protein band intensities were determined by densitometry, and this was achieved in collaboration with Gerard Huysmans at the Pasteur Institute (see below). Pet β-barrel wild-type folding dynamics were fitted using a double exponential equation, and Pet β-barrel G1076A mutant was fitted using a single exponential equation. Some of the folded protein samples were further purified to separate the folded from the unfolded protein using a Ni affinity column and by gel filtration chromatography (using a Superdex s200-10/300 column, GE healthcare).

### 3.2.3 Biophysical assays

#### 3.2.3.1 Densitometry

Densitometry analysis was performed on the SDS-PAGE of the folded/unfolded samples. This was undertaken in order to determine the fraction of protein that had been cleaved for each time point (0 min to 24 hrs). Note: I ran all of the folding experiments and SDS-PAGE determinations for all samples (3x for each protein); the densitometry was performed in collaboration with Gerard Huysmans at the Pasteur Institute.

#### 3.2.3.2 CD spectroscopy

A 1 mm fused silica cuvette with ~0.1 mg/mL protein was used to obtain far-UV CD spectra, recorded on a Jasco J-815 Spectropolarimeter. CD scans were recorded from 190 nm to 260 nm at 1 nm/step with an integration time of 1 sec. Background spectra of either 8 M urea, or Tris buffer with detergent micelles were recorded and subtracted from protein spectra. Three scans were averaged, and the spectrum was subtracted for buffer contribution. Thermal denaturation of the sample was performed at 218 nm as a function of temperature from 25–100 °C at a temperature change of 1 °C/min. The spectra were normalized to the mean residue ellipticity. Thermal unfolding was found to be irreversible. Note: thermal denaturation CD spectra shown in the paper were collected by Matthew Johnson. However, I did perform the same experiment at a different time.

#### 3.2.3.3 Fluorescence spectroscopy

All fluorescence spectra were recorded on a Varian Cary Eclipse fluorimeter. Protein samples of ~0.01 mg/mL in a 1 cm cuvette were excited with photons of $\lambda$= 295 nm (5 nm

bandpass) and emission was recorded from 300 nm to 500 nm, with an integration time of 0.1 s. Similarly to CD spectroscopy, background spectra were recorded and subtracted in the analysis. The emission spectra were collected from excitation of tryptophan residues.

## 3.3 Results

### 3.3.1. Pet β-barrel protein folding, different length of passenger domains

In this study, we focus on the folding of Pet β-barrel protein with increasing passenger domain lengths. Previously, we looked at folding of the Pet β-barrel with a single, short passenger domain. The Pet protein that was used to study mutational affects in the previous chapter is 43 kDa in total, of which 13 kDa is the passenger domain [1]. The β-barrel is present in all the proteins being studied in this section, but here, passenger domain length varies between the different proteins explored.

Previously, we studied the folding of the Pet 116β protein and found that the folding was essentially immediate [1]. Once folded, the passenger domain is cleaved from the barrel domain [12]. This process of cleavage in Pet protein is autocatalytic [13, 14]. The barrel (β) domain is 30 kDa in size, as shown in SDS-PAGE in Figure 3.2 A and the passenger domain is 13 kDa. Since the size of the passenger domain is comparatively small, it is not seen in SDS-PAGE. Folding of the protein, as seen from SDS-PAGE analysis, is apparently immediate, at least on the timescale of the measurements performed. In this case, protein was seen to be folded as soon as it was mixed with the detergent micelles.

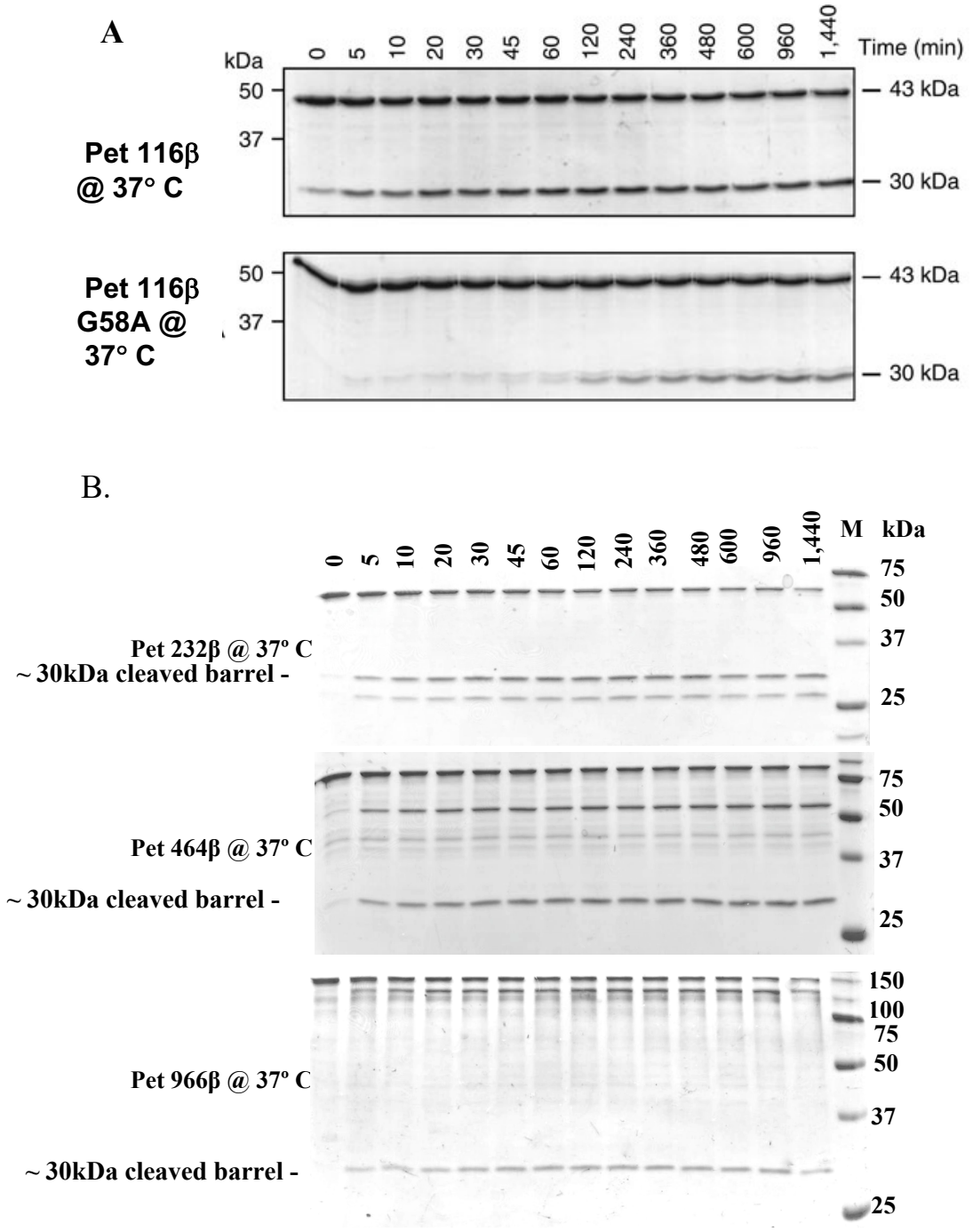


**Figure 3.2 A.** SDS-PAGE of Pet 116β and Pet 116β G58A (mutation in the barrel domain) folding at 37° C. **B.** Protein folding studies as the length of passenger domain was increased from 13 kDa (Pet 116β) to 26 kDa (Pet 232β) , 52 kDa (Pet 464β and 106 kDa (full length Pet 966β). Please note the marker lane on far right of each gel. 3 replicates were performed.

It has been known that the β-barrel plays an essential role in outer membrane protein folding [15, 16]. For that reason, G to A mutation (in the barrel domain) was introduced in order to understand the Pet β-barrel's role in protein folding, and additionally to understand

why some of the residues have been conserved through evolution, and their significance during Pet protein folding and assembly [1]. SDS-PAGE of the folded mutant protein showed slower cleavage of the barrel from the pet protein. This suggested that the protein folding is not native [16]. Autoproteolytic cleavage of the passenger domain is an indication of a correctly (native like) folded barrel [12, 14, 17].

To contextualise these findings, we sought to understand if the size of the passenger domain affects the folding and the cleavage of the passenger domain, initially by comparing Pet 232β and Pet 116β. The passenger domain in Pet 232β is double the size of Pet 116β. The protein was folded in folding buffer containing LDAO micelles at 37 °C. Figure 3.2 A and B show SDS-PAGE gel analysis of Pet protein folding. The efficiency and the delay in different folding reactions was monitored and distinguished based on the appearance of the autocatalytic cleavage product in the form of the ~30 kDa β-barrel.

Pet 232β shows delayed cleavage of the passenger domain (Fig. 3.2.B). In the case of Pet 232β ,the folded, cleaved barrel (~30 kDa) only appears at the 5 minute time point, compared to 0 min (during the mixing step of the reaction) of Pet 116β (Fig. 3.2 A, B). This delay in protein folding may be due to the longer passenger domain size, which evidently has an impact on folding kinetics.

As we increase the passenger domain size to 52 kDa (Pet 464β), folding and cleavage of the passenger domain is very similar to that seen for Pet 232β (26 kDa passenger domain). The appearance of the folded 30 kDa barrel within the first 5 mins suggests that the folding and the cleavage of the passenger domain is quite similar to Pet 232β.

The full-length Pet (Pet 966β) also shows the appearance of the β-barrel (~30 kDa in size) within the first 5 minutes. Pet 966β is 136 kDa in size, of which, 106 kDa is the passenger domain. Even though the folded barrel appears at around 5 minutes (as for Pet

232β and Pet 464β), the intensity of the folded barrel in the SDS-PAGE analysis at around 5 min is lower than that seen for Pet 232β and Pet 464β. The cleavage of the passenger domain only occurs when the protein is folded in its native state. Two possible hypotheses consistent with this observation are that the protein is being misfolded or is folding more slowly. We examine these possibilities in more detail in the following sections.

### 3.3.2 Protein folding at lower temperatures (15° C and 4° C)

To further understand the kinetics of the Pet protein folding, we folded Pet protein in LDAO at lower temperatures (15 °C and 4 °C). Folded protein was resolved in SDS-PAGE to understand the kinetics of folding at these lower temperatures. All protein constructs have the same barrel domain but different passenger domains. Pet 116β has 116 (13 kDa) residues of passenger domain immediately N-terminal to the barrel domain, Pet 232β has 232 (26 kDa) residues of passenger domain immediately N-terminal to the barrel domain, Pet 464β has 464 (52 kDa) residues of passenger domain immediately N-terminal to the barrel domain, and Pet 966β is the full-length Pet protein and has 966 (106 kDa) residues of passenger domain.

Pet 116β folds slower at 15 °C as seen in SDS-PAGE data (Fig. 3.3A). The folded, cleaved barrel domain appears at around 10 mins, and the folded barrel intensity at 24 hours is less than the folded protein at 37 °C. Pet 116β G58A (mutant) folds slower than Pet 116β at 37 °C (Fig. 3.3B). This was due to the misfolding of the barrel domain as shown by the trypsin assays (previous chapter) and tryptophan fluorescence assays.

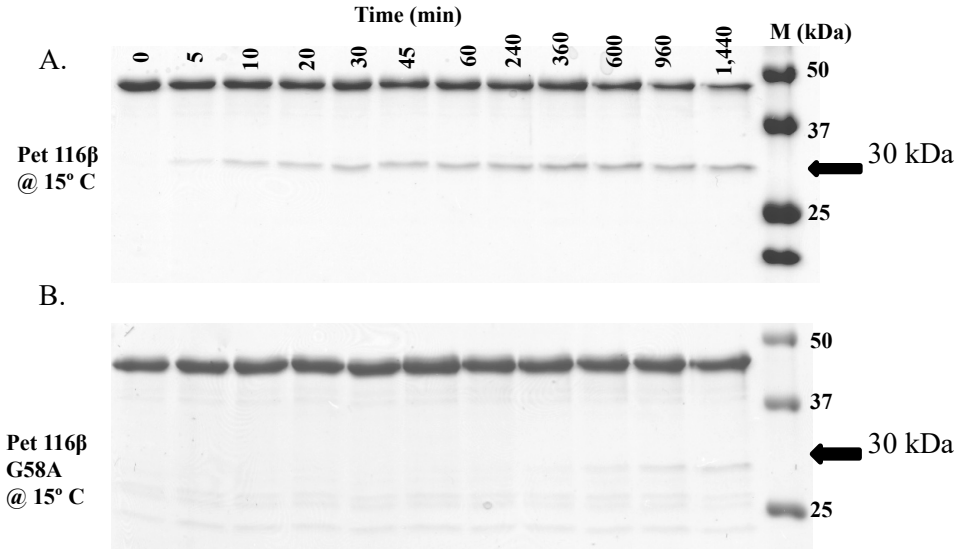


**Figure 3.3 A.** Pet 116β folding at 15 °C and **B.** Pet 116β G58A folding at 4 °C. The right lane in the gel is the marker. Folded Pet barrel appears at ~30 kDa. A small amount of folded beta barrel appears in Pet 116β G58A SDS – PAGE.

Pet 116β and Pet 116β G58A was folded at 4 °C to further slow down the kinetics of Pet folding. β-barrel in Pet 116β appears at around 45 minutes compared to ~10 minutes at 15 °C, and folds immediately after mixing at 37 °C.

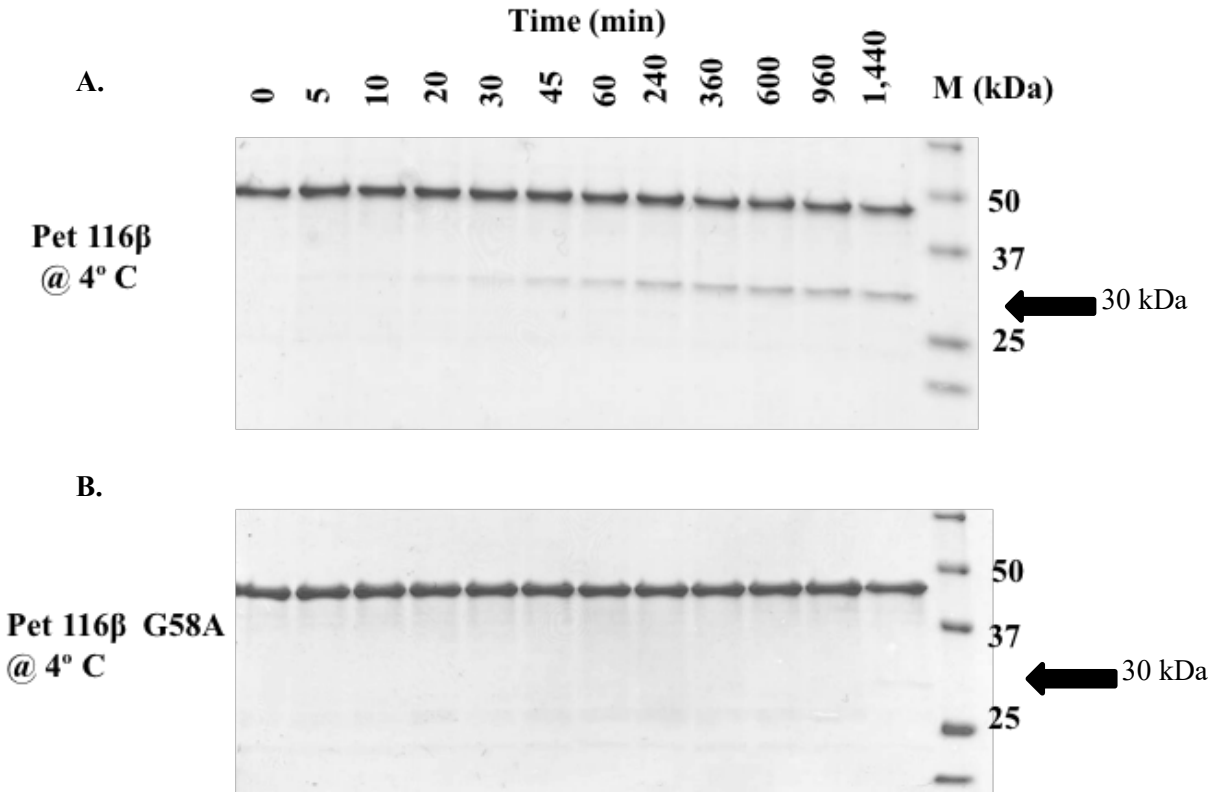


**Figure 3.4 A.** Pet 116β folding at 15 °C and **B.** Pet 116β G58A folding at 4 °C. The right lane in the gel is the marker. Folded Pet barrel appears close to the 30 kDa marker. Only a small amount of folded β-barrel appears in Pet 116β G58A SDS – PAGE.

The passenger domain in Pet proteins cleaves autocatalytically once folded in its native state. Pet 116β folds and autocatalytically cleaves the passenger domain after ~45 minutes as suggested by the appearance of 30 kDa barrel fragment (Fig. 3.4 A). However, no such bands are present in case of Pet 116β G58A folding at 4 °C (Fig. 3.4 B). This suggests that the barrel domain is either misfolded or there is a significant delay in the cleavage of the passenger domain.

### 3.3.3 Pet 232β, Pet 464β and Pet 966β folding @ 15° C

Pet 232β folds more slowly at 5 °C as seen by the delayed appearance (around 20 mins) of the 30 kDa β-barrel (Fig 3.5 A). The folded passenger domain also appears in the SDS-PAGE analysis. The passenger domain is ~26 kDa in size and appears just below the 30 kDa barrel in SDS-PAGE.

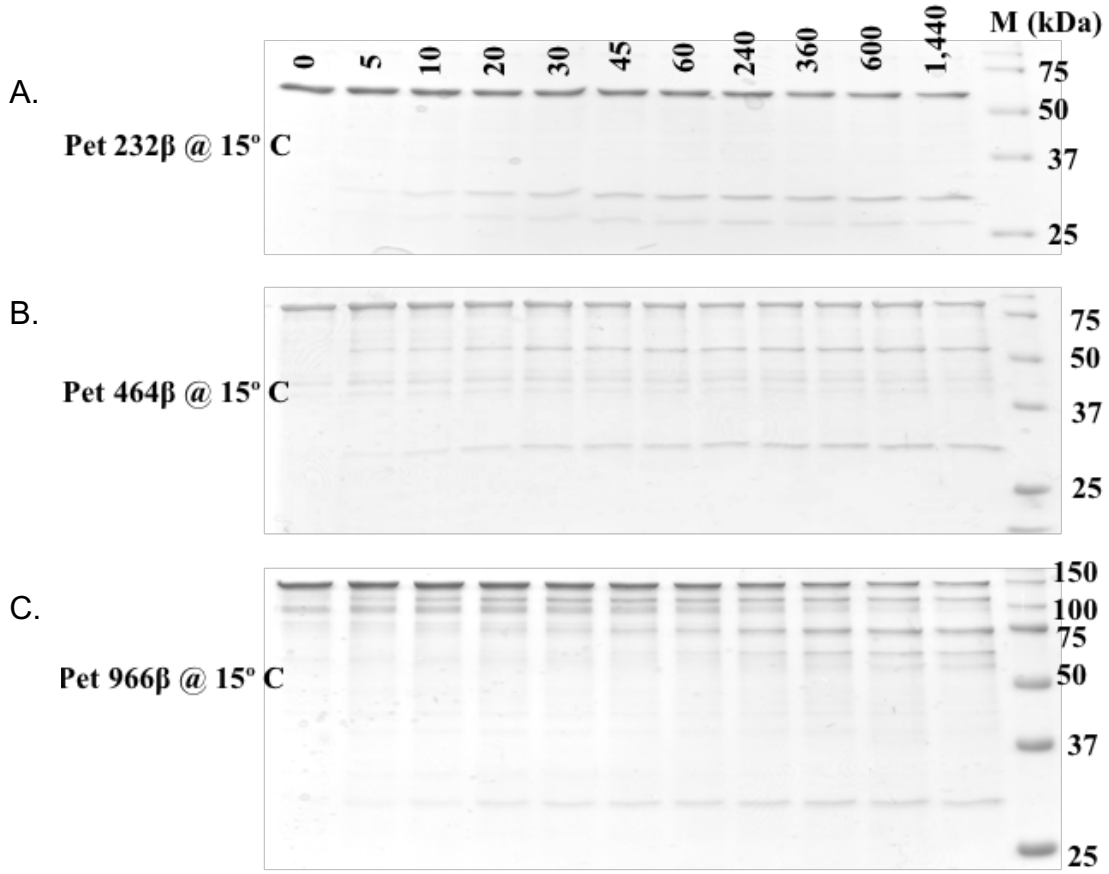


**Figure 3.5** An exploration of the effect of length of passenger domain on Pet protein folding. **A**. SDS- PAGE of Pet 232β folded at 15 °C. Pet 232β has 232 (26 kDa) residues of passenger domain. **B**. SDS-PAGE of Pet 464 folded at 15 °C. Pet 464β has 464 (52 kDa) residues of passenger domain. **C**. SDS-PAGE of Pet 966 folded at 15 °C. Pet 966β has 966 (106 kDa) residues of passenger domain. Pet 966β is the full length of Pet barrel protein. Right lane in the SDS-PAGE is the marker, and the 30 kDa barrel is clearly visible in each SDS-PAGE.

Pet 464β also appears to fold more slowly at 15 °C than at 37 °C, as shown in Figure 3.6 B. A significant amount of folded barrel appears around the 10 min time point, as seen in SDS-PAGE. The total amount of protein folded at around 24 hr time point is also significantly lower compared to the folded protein at 37 °C. Folding of Pet 464β at 15 °C generated multiple bands in addition to the 30 kDa folded barrel. Unfolded Pet 464β is ~82 kDa in size and runs above the 75 kDa marker as seen in Figure 3.5 B. The folded passenger domain of Pet 464β runs at ~52 kDa as seen in Figure 3.5 B. There are multiple bands (~40 kDa and ~45 kDa) that suggest the misfolding of Pet 464β. Curiously, these bands are less significant when the protein is folded at 37 °C.

Pet 966β (136 kDa) is the full-length Pet protein. The folding of Pet 966β is even slower than Pet 464β and 232β at the same temperature (Fig. 3.5 C). The folded barrel appears ~20 mins into the folding reaction, as shown in Fig 5C. The full-length Pet protein (136 kDa) and folded passenger domain (106 kDa) run true to their size as seen in Fig 3.5 C. There are multiple bands around 100 kDa, 75 kDa, 45 kDa and 44 kDa, which suggest the misfolding of the Pet protein. Such misfolding was not an issue for Pet 116β and Pet 232β. We can therefore summarise these observations that as we increased the length of the passenger domain, protein misfolding became more obvious.

### 3.3.4 Pet 232β, Pet 464β and Pet 966β tertiary structure using circular dichroism and fluorescence spectroscopy.

CD spectra for β-sheet proteins show a characteristic minimum at ~218 nm [18, 19], which is what we saw with Pet 116β protein. Pet 116β mostly folds to β-sheet because of the presence of the 30 kDa barrel.

A.

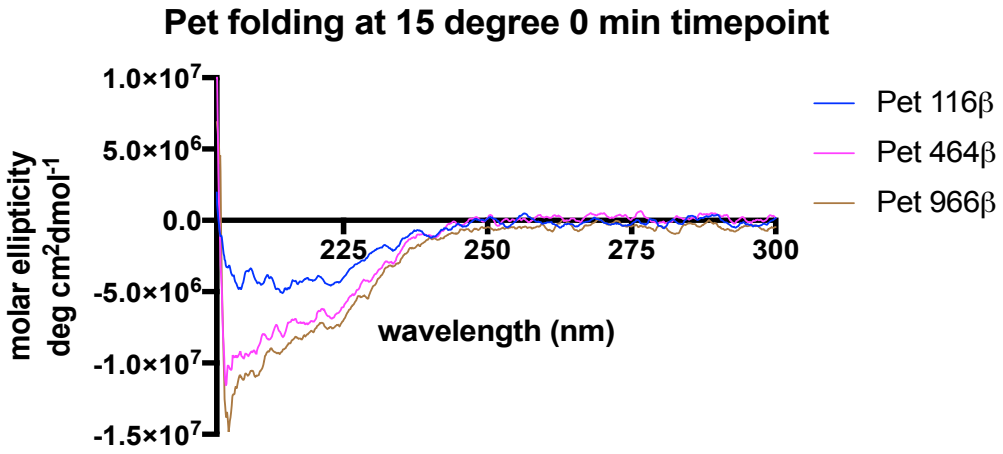


B.

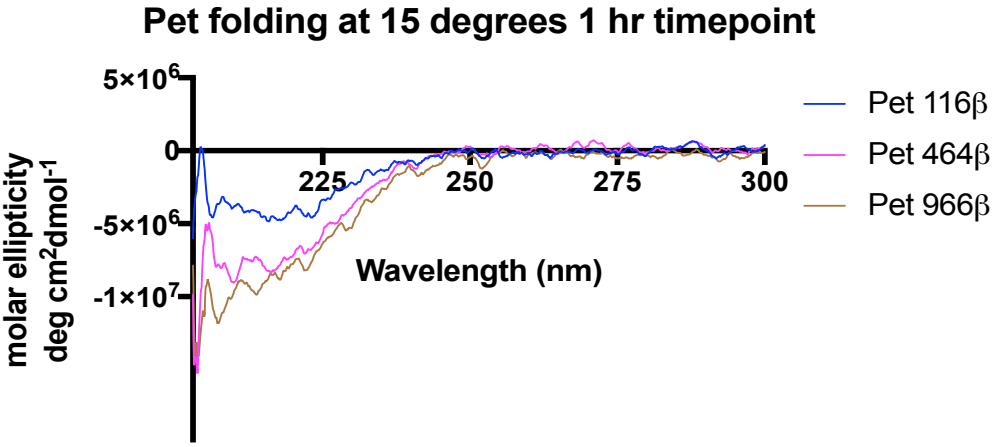


C.

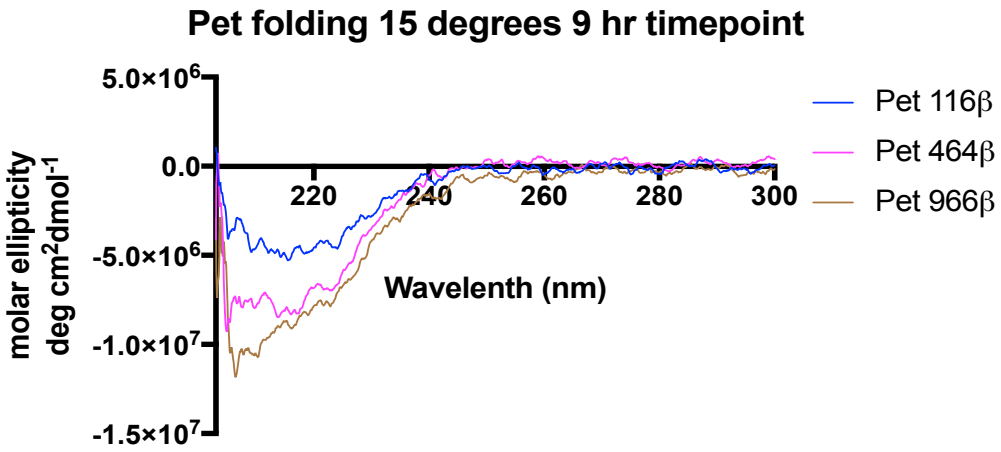


**Figure 3.6** CD spectra of folded Pet 116β, Pet 464β and Pet 966β at 15 °C. **A**. Protein samples collected immediately after the mixture of the protein with the protein folding buffer. **B**. Samples collected at 1 hr time point and **C**. Samples collected at 9 hr time point. Blue line = Pet 116β, magenta line = Pet 464β and brown line = Pet 966β. Data shown here is the average of 3 different experiments.

However, the folded passenger domain could be a mixture of β-sheets, α-helices and random coils. Figure 3.6 A, B and C show CD spectra of Pet 116β, 464β and Pet 966β. CD spectra of Pet 116β suggest that the secondary structure is achieved during the mixing of the protein. CD spectra of Pet 464β and Pet 966β show that only part of the protein is structured. At 0 min and 1 hr time point, a significant amount of Pet 464β and Pet 966β is still unstructured, which is obvious from the CD spectra. The difficulty at this point is to determine the contribution of the passenger domain and the barrel domain in the collected spectra. To do this, it is necessary to fold the passenger domain by itself and subtract its contribution from the spectra.

To this end, passenger domains (232, 464 and 966) only were purified, and folding was attempted in similar conditions. However, it was quickly seen that the passenger domains were aggregating, and SDS-PAGE showed that they were appearing at higher molecular weights than their individual masses. This appears to indicate that the passenger domain cannot achieve the native structure in the absence of beta barrel domain, a crucial and interesting observation.

A.

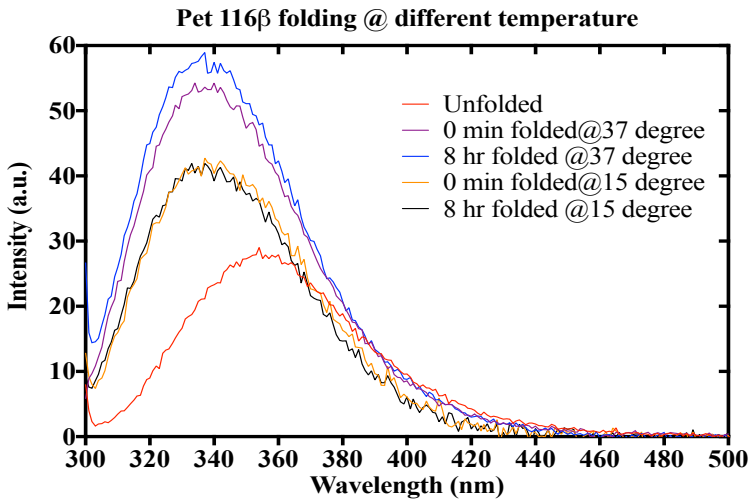


B.

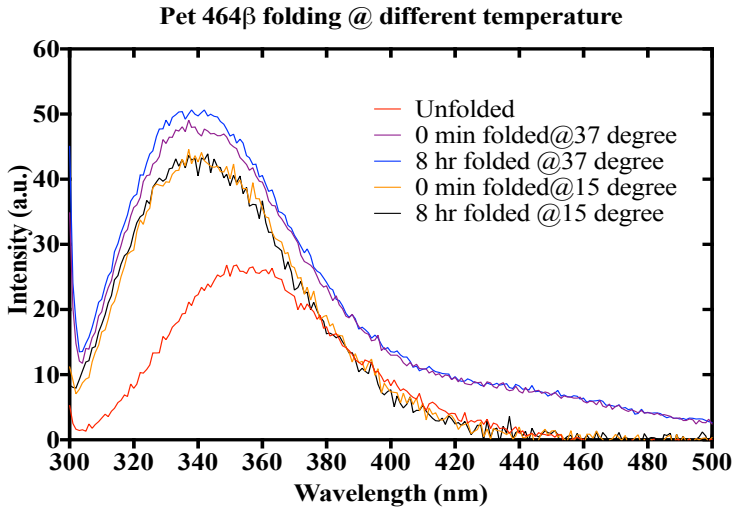


C.

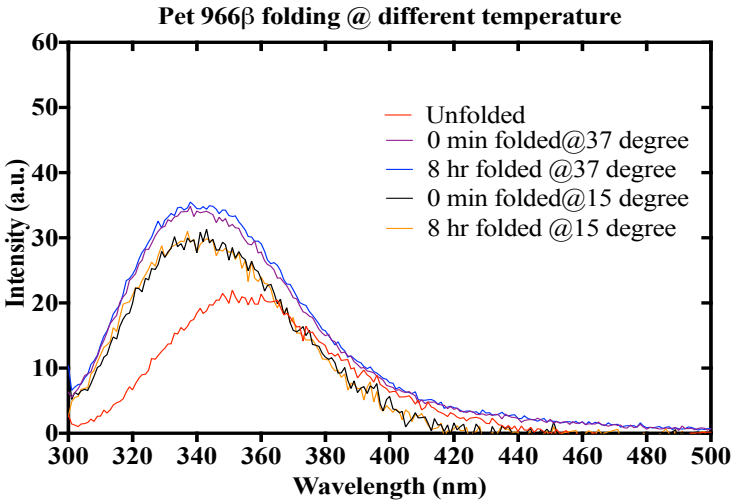


**Figure 3.7** Tryptophan fluorescence spectra showing: **A**. Pet 116β folding at 15 °C; **B.** Pet 464β folding at 15 °C; and **C**. Pet 966β folding at 15 °C. Data shown here is the average of 3 different experiments.

### 3.3.5 Tertiary structure using tryptophan fluorescence

There are four tryptophan (Trp) residues in the barrel domain of Pet, and four tryptophan residues in the full-length passenger domain. Tryptophan fluorescence monitors the sum of the local environments of each tryptophan [20, 21]. When tryptophan residues move to hydrophobic environments such as a lipid bilayer, their fluorescence emission becomes blue shifted and increases in intensity [4, 20, 21]. Compared to other fluorescent amino acids, the use of Trp as an intrinsic probe of protein microenvironment is advantageous due to its fluorescence sensitivity to the polarity of its location [21].

Unfolded Pet 116β, Pet 464β and Pet 966β exhibit a maximum emission wavelength around 355 nm, and the intensity is about the same in all cases. If the tryptophan residues are still in contact with the buffer, intensity is low, whereas the intensity starts to increase when the protein starts to fold in LDAO. In all cases where folding was explored in LDAO detergent micelles, (Pet116βm, Pet 464β and Pet 966β), the fluorescence spectra increase over time at 15 °C as seen in Fig 3.7.

Folded Pet 466β and Pet 966β had a diminished intensity at 9 hr, relative to Pet 116β folded both at 37 °C and 15 °C (Fig. 3.7). This suggests that it takes longer for Pet 464β and Pet 966β to fold and thereby bury their tryptophan residues. The intensity of tryptophan residues in Pet 966β is significantly reduced compared to Pet 116β. This could be because of the slow folding of the full-length protein, or as a result of the misfolding seen above.

### 3.3.6 Pet 232β, Pet 464β and Pet 966β folding @ 4 °C

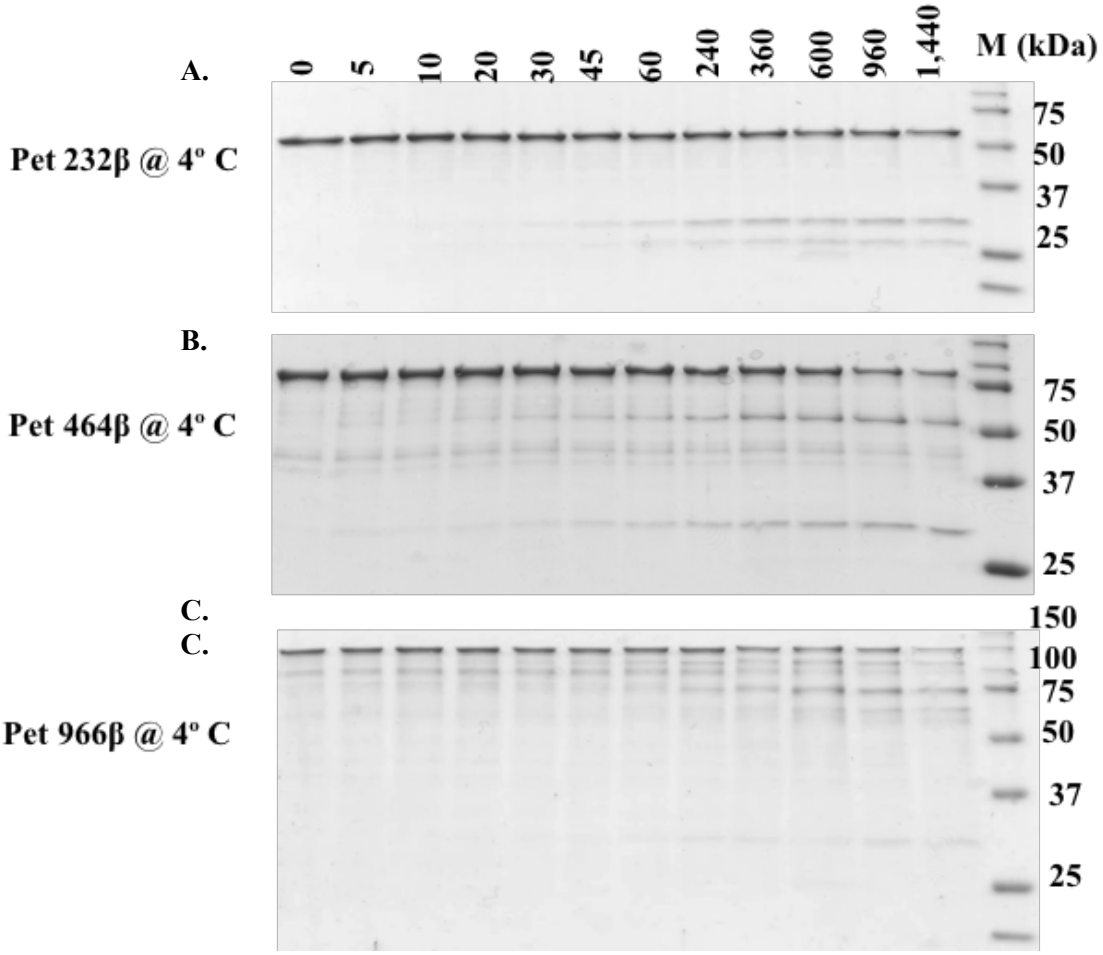


**Figure 3.8** Pet protein folding at 4 °C. **A**. Pet 232β folding at 4 °C, **B**. Pet 464β folding at 4 °C and **C**. Pet 966β folding at 4 °C. Data shown here is the average of 3 different experiments.

Evidence of Pet protein (Pet 232β, Pet 464β and Pet 966β) folding and the appearance of the 30 kDa barrel is significantly less at 4 °C as seen in Fig. 3.9. As seen previously at 15 °C, cleavage and appearance of the folded barrel at 30 kDa is significantly less compared to the folding at 37 °C.

Pet proteins attain native structure when folded at 37 °C in the presence of micelles (LDAO). The appearance of the folded barrel domain (~ 30kDa in SDS-PAGE) confirms the native structure because autoproteolytic reaction of passenger domain is only possible when the β-barrel is folded in the membrane and acts as a passage for passenger domain translocation across the membrane [1, 7]. The β-barrel domain is thereby embedded in the membrane and acts as a pore for passenger domain translocation [16, 22].

At 37 °C, Pet protein folds rapidly. In fact, some of it is folded within the mixing time (mixing unfolded protein in the folding buffer) as shown in SDS PAGE (Fig. 3.2 A). Initially, we wanted to fold Pet proteins at lower temperature in order to slow the kinetics and identify different folding steps. Our protein folding results at lower temperature suggest that β-barrel is partially misfolded and most likely does not become embedded in the membrane.

### 3.3.6 Folded proteins digested with trypsin

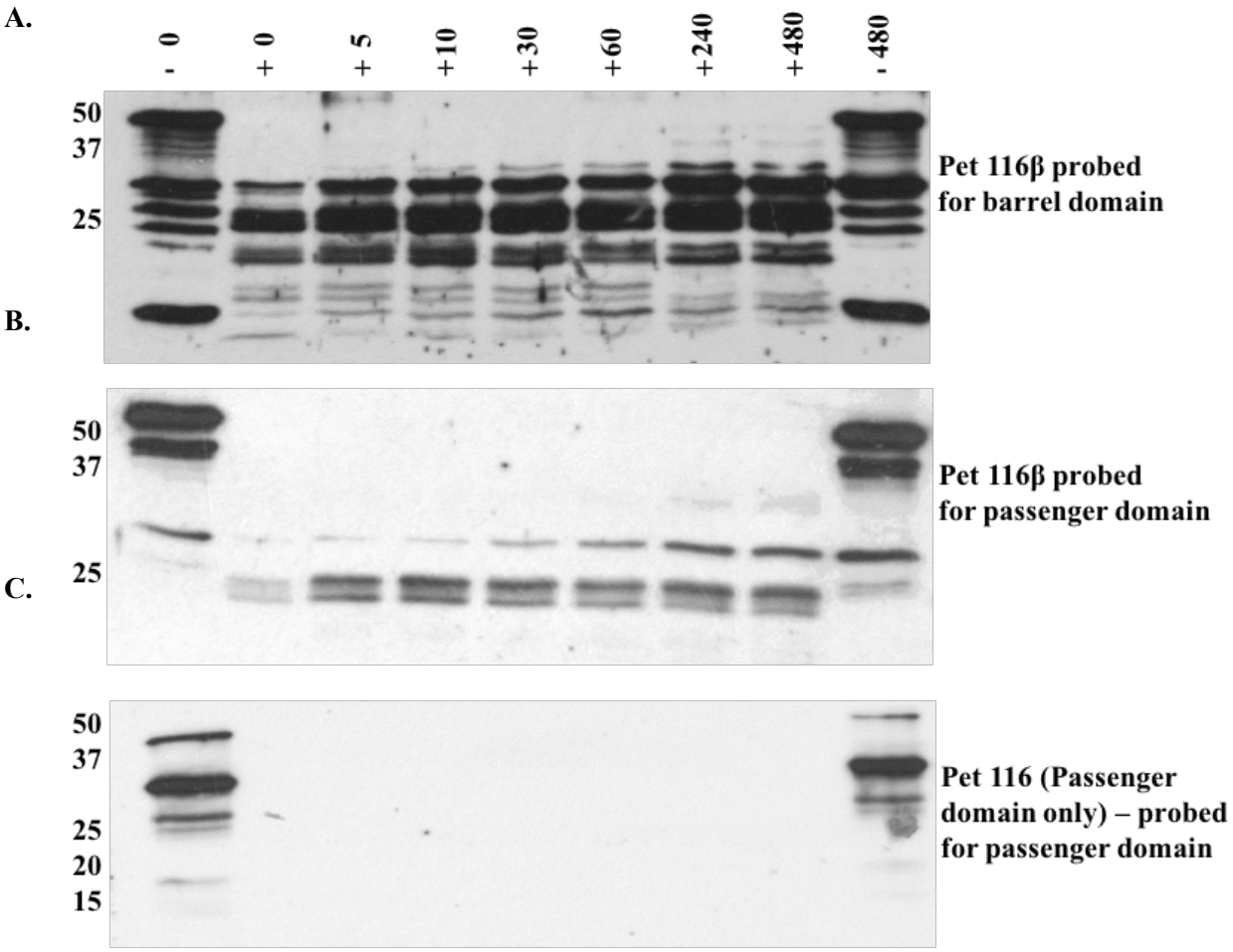


**Figure 3.9** Trypsin treated samples probed for barrel and passenger domain. **A)** Pet 116β probed with barrel antibody. **B)** Pet 116β probed with passenger antibody and **C)** Pet 116 (passenger domain only) probed with passenger antibody. The negative is not treated with trypsin and positive is treated with trypsin.

Pet proteins folded in LDAO were incubated with a limited amount (20 μg $mL^{-1}$) of trypsin for 20 min. Trypsin cleaves unfolded or partially folded proteins, generating

proteolytic products of different sizes [7, 12]. These samples are then probed with barrel and passenger domain antibody separately. Barrel antibody only binds to the β-barrel domain of the Pet protein, and passenger domain antibody only binds to the passenger domain part of the protein. Barrel and passenger domain folding can thereby be monitored separately.

Pet 116β generates multiple bands when treated with trypsin. When folded into LDAO, some parts of the barrel are still exposed to be cleaved by trypsin. When trypsin cleaves off different sections of the exposed barrel domain, it generates multiple fragments. As seen in our sequencing data in the previous chapter, all of these fragments (24–30 kDa) start from the same residue. This suggests that β-barrel is folded correctly.

The passenger domain of Pet 116β is ~13 kDa and 116 residues in size. Folded proteins were treated with trypsin, and the trypsin treated samples were analysed using Western blotting (Fig. 3.9). When we probed the trypsin treated Pet 116β with passenger domain antibody, Pet 116β showed multiple fragments that ranged between 25–30 kDa. This was unusual because the passenger domain of Pet 116β is just 13 kDa in size. It is hard to say whether the protein was aggregated or running as dimers, or potentially that the antibody was recognizing the passenger domain still attached to the barrel domain.

Folding just the passenger domain (116 residues, 13 kDa) was also attempted. Once folded, it was incubated in trypsin and when resolved in SDS-PAGE, where no bands were seen. This suggests that the passenger domain was unfolded and it was accessible to trypsin, and the trypsin fully digested the passenger domain to fragments too small to be seen using SDS-PAGE.

#### 3.3.6.1 Pet 232β folding and treatment with trypsin

Pet 232β was probed with barrel domain antibody and passenger domain antibody (Fig. 3.10). The β-barrel appears at the 0 min time point, whereas the passenger domain

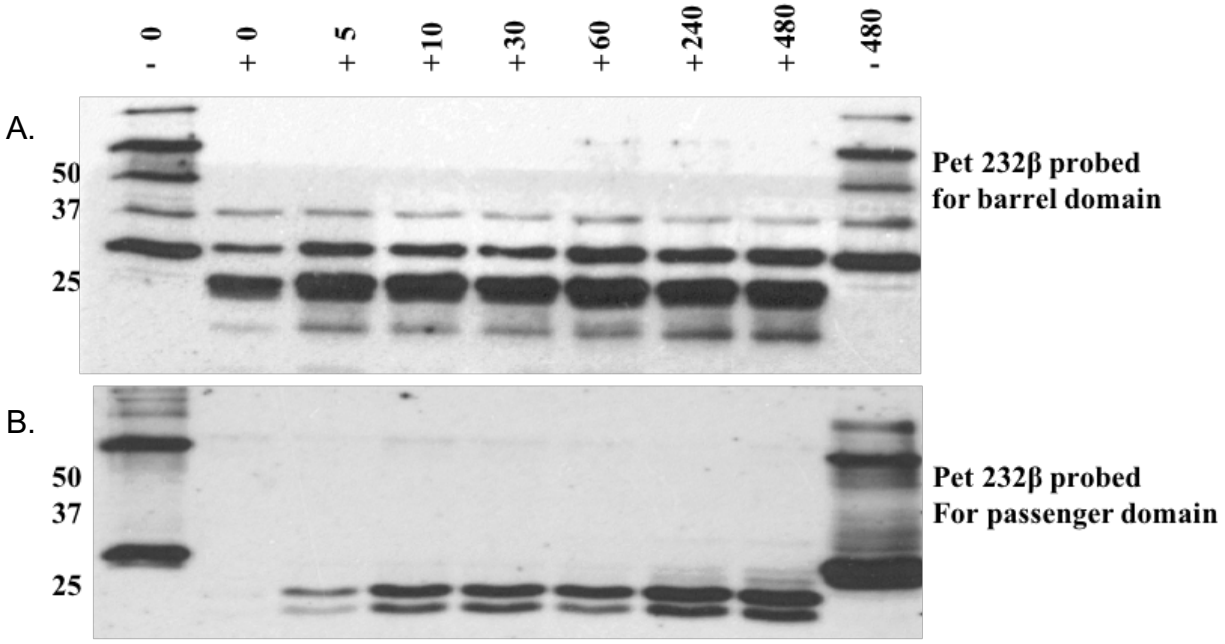


starts to appear around the 5 min time point. At 5 min, the passenger domain is not digested, and it is picked up when probed with passenger domain antibody. This suggests that the barrel folds first and its presence may therefore be essential to passenger domain folding.

**Figure 3.10** Trypsin treated samples probed for barrel and passenger domain. **A)** Pet 232β probed with barrel antibody. **B)** Pet 232β probed with passenger antibody; negative is not treated with trypsin and positive is treated with trypsin.

### 3.3.6.2. Pet 464β folding and treatment with trypsin

Pet 464β was probed with barrel domain antibody and passenger domain antibody. Parts of the barrel domain are accessible to trypsin, which cleaves part of the protein generating multiple fragments as shown in Figure 3.11.

When probed with barrel domain antibody, the protein fragments that appear in Western blotting contain barrel domain. Whereas, when proteins are probed with passenger

domain antibody, the protein fragments that appear in Western blotting contain passenger domain. Pet 464β was probed with β-barrel antibody that identified fragments between ~24 kDa and 35 kDa. However, the strongest bands appear around 30 kDa, which corresponds to the size of the β-barrel itself. Pet 464β was then probed with passenger domain antibody, which identified fragments between 37 kDa to 24 kDa. The passenger domain of 464β is ~52 kDa. However, the fragments with highest molecular weight appear at ~37 kDa. This suggest that part of the passenger domain is also cleaved by trypsin. At the 0 min time point, all the samples are digested by trypsin. This suggests that the passenger domain was not folding until ~5 mins into the folding reaction.

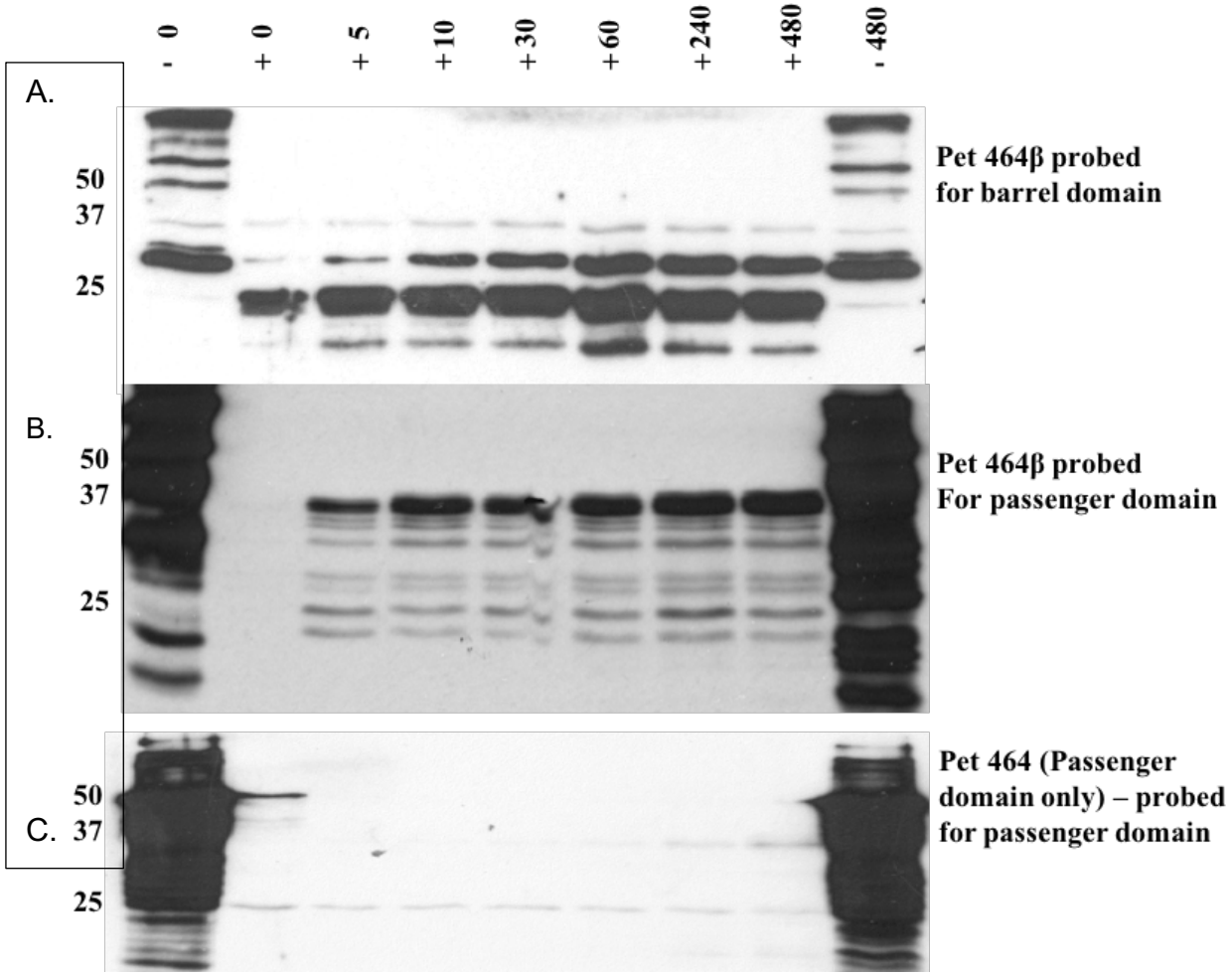


**Figure 3.11** Trypsin treated samples probed for barrel and passenger domain. **A)** Pet 464β probed with barrel antibody. **B)** Pet 464β probed with passenger antibody and **C)** Pet 464

(passenger domain only) probed with passenger antibody. Negative is not treated with trypsin and positive is treated with trypsin. 3 different experiments were performed.

### 3.3.6.3. Pet 966β folding and treatment with trypsin

Pet 966β (136 kDa) is the full-length Pet protein, of which 106 kDa is the passenger domain. Pet 966β was probed with barrel domain antibody which identified fragments between 24–30 kDa. As seen in Figure 3.12, there was some delay before the appearance of folded β-barrel.

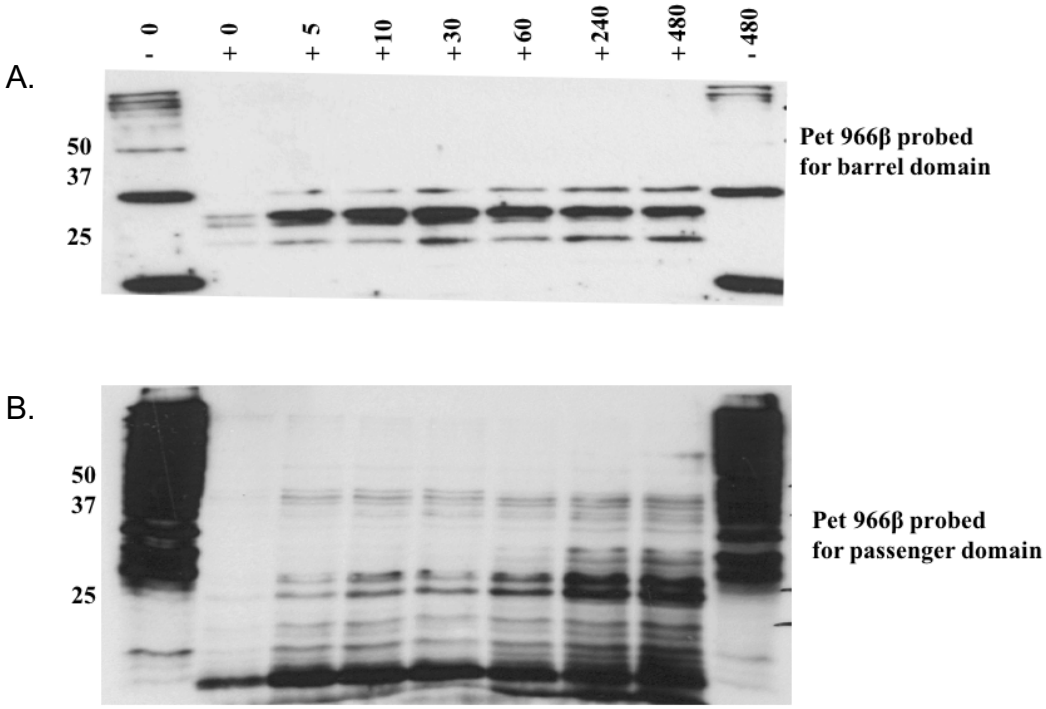


**Figure 3.12** Trypsin treated samples probed for barrel and passenger domain. **A)** Pet 966β probed with barrel antibody. **B)** Pet 966β probed with passenger antibody; negative is not treated with trypsin and positive is treated with trypsin.

When probed with passenger domain antibody, the Western blot shows multiple fragments of passenger domain containing protein. Trypsin most likely accessed the

unfolded parts of the protein and digested it. This led to the appearance of multiple fragments of passenger domain containing Pet protein.

### 3.4. Discussion and conclusion

The first autotransporter protein was discovered about 30 years ago, however the mechanism of passenger domain translocation across the outer membrane is still debated [23]. To date, studies of folding of autotransporter β-barrel membrane proteins have been mostly focussed on insertion of the β-barrel into the membrane. Recent studies have focussed on the different factors catalysing folding and insertion of β-barrel proteins into the outer membrane [24]. BAM complex and chaperone proteins such as SurA, Skp and DegP are known to be involved in inserting β-barrel in the outer membrane [24-26].

In the previous chapter, we discussed conserved motifs and residues in Pet β-barrel protein [1]. Conserved Glycine residues were mutated to better understand the β-barrel folding. We concluded that the mutation of conserved glycine residues leads to some misfolding of the β-barrel domain, which leads to slower passenger domain translocation, and fewer proteins translocating across the membrane.

In this chapter, we studied different factors that can affect Pet β-barrel folding. For the proteins explored here, the size of the β-barrel remained the same but the size of the passenger domain was increased, to determine whether an increase in the size of passenger domain delays translocation of the passenger domain. It has been previously shown that integration of β-barrel into the membrane and secretion of the passenger domain in autotransporter proteins is not affected by a truncated version of the passenger domain [2, 12]. Large segments of passenger domain can be deleted without affecting the folding of the β-barrel and the secretion of the truncated passenger domain [2, 12].

Particularly relevant previous work studied foliding of EspP, a protein that is highly homologous to Pet protein. The Bernstein lab showed that EspP protein (bearing different lengths of passenger domain) folds at around 2 mins and when treated with proteinase K, stable fragments appear after around 5 mins [2]. Notably, these reactions were performed in the presence of BamABCDE (*E. coli* BAM complex) and chaperone SurA. Bam complex and SurA are known to assist in autotransporter folding [2, 27].

With this context in mind, in this chapter, Pet proteins (bearing different sizes of passenger domain) were folded in the absence of Bam complex and other chaperone proteins that are known to assist in autotransporter folding. Pet protein folded rather quickly when the size of the passenger domain was only 13 kDa. However, when the size of the passenger domain was increased, the appearance of the folded and cleaved barrel was slower. Western blotting confirmed the appearance of the folded β-barrel and the passenger domain at around 5 mins after mixing. To differentiate the folded barrel from the cleaved passenger domain, Western blot samples were probed by both β-barrel and passenger domain antibody.

Pet proteins folded slower at lower temperature. By decreasing temperature, we sought to study the kinetics and acquisition of secondary and tertiary structure on a more amenable time-scale. Since we were unable to successfully fold the passenger domain by itself, we did not have enough information to subtract the contribution of passenger domain in CD spectra and fluorescence spectroscopy. However, we did find that at lower temperatures, the achieved secondary structures in the presence of longer passenger domains were different from the Pet protein containing a shorter passenger domain. Fluorescence spectra confirmed that the protein folding was distorted. The spectra for protein containing longer passenger domain had lower intensity compared to Pet 116β, the protein with shortest passenger domain.

When we probed Pet proteins with barrel domain and passenger domain antibody, we found out that there was a delay in passenger domain folding. In most cases, we found out that barrel domain appeared at 0 mins, whereas the passenger domain appeared only after around 5 mins. Pet proteins showed more fragments when probed with passenger domain antibody. This could be because the passenger domain did not achieve native structure and was exposed for trypsin to digest the protein.

Overall, these results indicate some crucial differences between folding behaviour and kinetics of Pet when compared to other autotransporter proteins that have been previously studied. Pet folding is uniquely more sensitive to the size of the passenger domain, and this provides insight into potential methods for manipulation of this protein. Moreover, these differences suggest that further studies on autotransporter folding are vital, as one mechanistic envelope does not accurately describe or predict the behaviour of this crucial class of proteins.

## 3.5. References


1. Leyton, D.L., *et al.*, A mortise-tenon joint in the transmembrane domain modulates autotransporter assembly into bacterial outer membranes. Nat Commun, 2014. **5**: p. 4239.
2. Roman-Hernandez, G., J.H. Peterson, and H.D. Bernstein, Reconstitution of bacterial autotransporter assembly using purified components. Elife, 2014. **3**: p. e04234.
3. Gerlach, L., *et al.*, Folding of beta-Barrel Membrane Proteins into Lipid Membranes by Site-Directed Fluorescence Spectroscopy. Methods Mol Biol, 2019. **2003**: p. 465-492.
4. Kim, J.E., *et al.*, Probing folded and unfolded states of outer membrane protein a with steady-state and time-resolved tryptophan fluorescence. J Phys Chem B, 2006. **110**(35): p. 17656-62.
5. Kleinschmidt, J.H., *et al.*, Outer membrane protein A of Escherichia coli inserts and folds into lipid bilayers by a concerted mechanism. Biochemistry, 1999. **38**(16): p. 5006-16.
6. Eslava, C., *et al.*, Pet, an autotransporter enterotoxin from enteroaggregative Escherichia coli. Infect Immun, 1998. **66**(7): p. 3155-63.
7. Yuan, X., *et al.*, Molecular basis for the folding of beta-helical autotransporter passenger domains. Nat Commun, 2018. **9**(1): p. 1395.
8. Schiffrin, B., D.J. Brockwell, and S.E. Radford, Outer membrane protein folding from an energy landscape perspective. BMC Biol, 2017. **15**(1): p. 123.
9. Voss, B.J., *et al.*, Analysis of surface-exposed outer membrane proteins in Helicobacter pylori. J Bacteriol, 2014. **196**(13): p. 2455-71.
10. Junker, M., *et al.*, Pertactin beta-helix folding mechanism suggests common themes for the secretion and folding of autotransporter proteins. Proc Natl Acad Sci U S A, 2006. **103**(13): p. 4918-23.
11. Oliver, D.C., *et al.*, A conserved region within the Bordetella pertussis autotransporter BrkA is necessary for folding of its passenger domain. Mol Microbiol, 2003. **47**(5): p. 1367-83.
12. Dautin, N., *et al.*, Cleavage of a bacterial autotransporter by an evolutionarily convergent autocatalytic mechanism. EMBO J, 2007. **26**(7): p. 1942-52.
13. Barnard, T.J., *et al.*, Molecular basis for the activation of a catalytic asparagine residue in a self-cleaving bacterial autotransporter. J Mol Biol, 2012. **415**(1): p. 128-42.
14. Tajima, N., *et al.*, A novel intein-like autoproteolytic mechanism in autotransporter proteins. J Mol Biol, 2010. **402**(4): p. 645-56.
15. Ricci, D.P. and T.J. Silhavy, Outer Membrane Protein Insertion by the beta-barrel Assembly Machine. EcoSal Plus, 2019. **8**(2).
16. Bernstein, H.D., Type V Secretion in Gram-Negative Bacteria. EcoSal Plus, 2019. **8**(2).
17. Ieva, R. and H.D. Bernstein, Interaction of an autotransporter passenger domain with BamA during its translocation across the bacterial outer membrane. Proc Natl Acad Sci U S A, 2009. **106**(45): p. 19120-5.
18. Greenfield, N.J., Using circular dichroism spectra to estimate protein secondary structure. Nat Protoc, 2006. **1**(6): p. 2876-90.
19. Ranjbar, B. and P. Gill, Circular dichroism techniques: biomolecular and nanostructural analyses- a review. Chem Biol Drug Des, 2009. **74**(2): p. 101-20.
20. Vivian, J.T. and P.R. Callis, Mechanisms of tryptophan fluorescence shifts in proteins. Biophys J, 2001. **80**(5): p. 2093-109.

21. Doring, K., *et al.*, A long lifetime component in the tryptophan fluorescence of some proteins. Eur Biophys J, 1995. **23**(6): p. 423-32.
22. Pavlova, O., *et al.*, Mechanistic link between beta barrel assembly and the initiation of autotransporter secretion. Proc Natl Acad Sci U S A, 2013. **110**(10): p. E938-47.
23. Pohlner, J., *et al.*, Gene structure and extracellular secretion of Neisseria gonorrhoeae IgA protease. Nature, 1987. **325**(6103): p. 458-62.
24. Hagan, C.L., T.J. Silhavy, and D. Kahne, beta-Barrel membrane protein assembly by the Bam complex. Annu Rev Biochem, 2011. **80**: p. 189-210.
25. Wagner, J.K., *et al.*, Contribution of the periplasmic chaperone Skp to efficient presentation of the autotransporter IcsA on the surface of Shigella flexneri. J Bacteriol, 2009. **191**(3): p. 815-21.
26. Ruiz-Perez, F., *et al.*, Roles of periplasmic chaperone proteins in the biogenesis of serine protease autotransporters of Enterobacteriaceae. J Bacteriol, 2009. **191**(21): p. 6571-83.
27. Hussain, S. and H.D. Bernstein, The Bam complex catalyzes efficient insertion of bacterial outer membrane proteins into membrane vesicles of variable lipid composition. J Biol Chem, 2018. **293**(8): p. 2959-2973.

# Chapter 4. Introduction to carbon nanomaterials and their interactions with cell membrane lipids

## 4.1 Cells and cell membranes: a biological interface

Cells were first discovered by Robert Hooke in 1665 and they are the basic functional and structural units of living organisms. In most cells, the structure of the cell membrane is remarkably similar, and this will be a focus of our study in the next chapters.

The cell membrane is a protective layer of the cell, which separates the inside and outside of an organism [1]. It acts as a selective permeable membrane, by allowing gradients of ions to be created across the membrane. The cell membrane controls the diffusion of molecules into the cell [1]. The cell membrane also recognizes, transmits, and transduce signals. Cell membranes comprise assemblies of different kind of lipid bilayers which are stabilised by hydrophobic interactions. Proteins are embedded in the lipid bilayer which sometime acts as an anchor and provides mechanical support for the cell. The self-assembled bilayers that form the structural basis of the membrane are usually 4–10 nm thick, and as suggested by the term ‘bilayer’ are composed of a two-molecule thick layer [2]. Membrane proteins and sugars that are part of the membrane help maintain the structural integrity of the membrane. The fluid mosaic model that was introduced in the early 1970s still holds true in many aspects, however the complexity of cell membranes is accepted to be far more complex. The cell membrane contains a large number of different lipid molecules that are distributed throughout the membrane and host a range of other components.

Lipids are important fatty molecules that have different roles in the human body, and they are the major components of all cell membranes. There are three main types of lipids: a) triglycerides, b) phospholipids, and c) sterols. Triglycerides arise from dietary routes, where they are mostly found in fried foods, (plant) oils and some meats. Sterols are the least

common type of lipids, but within this vital class, cholesterol is one of the most widely known sterols. Cholesterol is also an important component of the cell membrane.

### 4.1.1. Phospholipids, Liposomes and lipid bilayers

Phospholipids are essential to building a protective barrier around cells and are synthesized in the body to form protective barriers around all cells and organelles. Understanding the physicochemical properties of cell membrane lipids is critical to understand their function, and how they interact with exogenous materials. However, interrogating lipids natively at the surface of cells raises many complications in terms of morphology, robustness and chemical identity. Thus, scientists have used supported lipid bilayers (SLBs, Fig. 4.1A) and liposomes (Fig. 4.1 B.) to mimic biological cell membranes consisting of various structurally similar phosphatidylcholines as the main component [3].

Phosphatidylcholines are one of the most commonly encountered classes of phospholipid in the biological cell membrane [4]. Most of the lipids utilised in our experiments are from the phosphatidylcholine family. Their polar head groups are made up of various hydrophilic moieties and their non-polar hydrocarbon chains can differ in their degree of unsaturation and length. This affects the bilayer integrity, permeability, mechanical properties, and structure in cells, and also the surface charge of liposomes and supported lipid bilayers [5].

Phospholipids tend to form closed structures when they are hydrated in water or other aqueous solutions. Lipids have a hydrophobic tail and a hydrophilic head, rendering their structure amphiphilic, like detergents; when they are exposed to water, their hydrophobic tails are attracted toward each other, while the heads are exposed to the aqueous environment (both external and internal). Thus, forming a bilayer that is enclosed to a spherical structure with water both inside and outside is a highly preferable mode of self-assembly for such molecules.

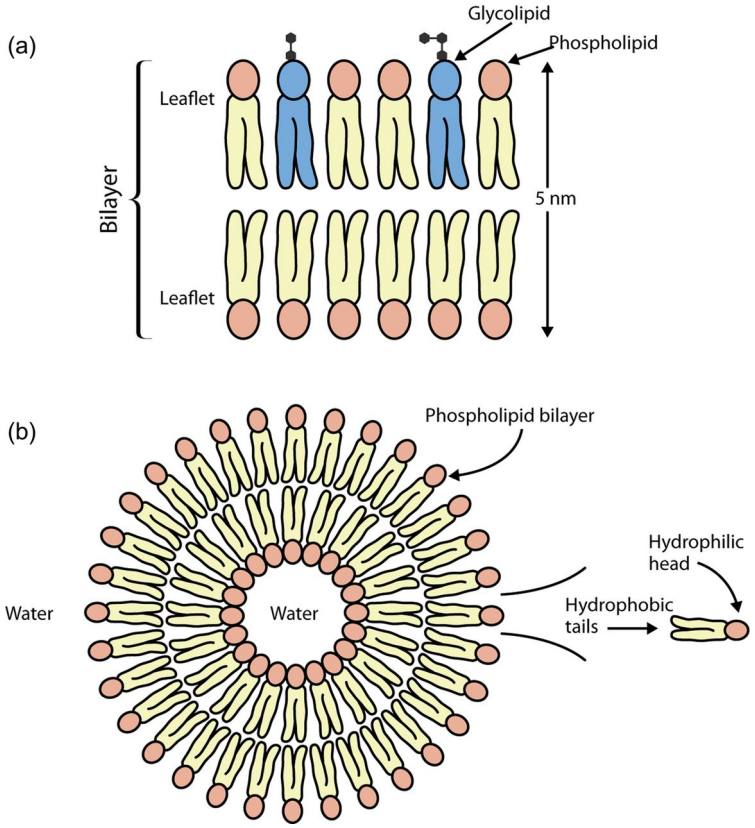


**Figure 4.1**: Liposomes are therefore formed as spheres comprising a 'capsule' of lipid bilayer surrounding an aqueous phase droplet, as depicted in Figure 1(b), and are often used as models for biological membranes in biomedical/biological research.

Liposomes and their interactions with proteins, nanomaterials, *etc.* can be much more easily studied *in vitro* using model systems within laboratories than using real biological membranes that are far more complicated to both interrogate and harvest [6, 7]. Permeability, lamellarity, size and enclosed volumes in liposomes can be controlled through lipid choice and preparation method, which makes them ideal for research. The interplay of chain lengths, charge on the head groups, and different ratios of phospholipids is of much interest in biomedical and biological research [8]. When dispersed in water (or a hydrophilic environment) at the right conditions, many phospholipids can spontaneously form liposomes. It is energetically favourable for the hydrophobic tails of the phospholipids to arrange on the inside of a bilayer, creating its own hydrophobic microenvironment, while the

hydrophilic heads protect this from the aqueous solution. The size of liposomes can be controlled by preparation method, commonly sonication and extrusion. In recent years, these methods have been extensively used for drug studies of newly synthesized molecules [9].

Liposomes have been extensively studied for their resemblance to the cell membrane and also as a drug delivery system. They are most commonly characterised by their size, where size is an important factor in determining the liposome's applications. Size can range from about 30 nm to several microns, with commensurate changes in flexibility and stability. Three major types of liposomes are typically encountered: small unilamellar vesicles (SUV), large unilamellar vesicles (LUV), and multilamellar vesicles (MLV). Small unilamellar vesicles usually have a diameter less than 100 nm [10], although these sizes can vary depending on the ionic strength and the lipids being used [10]. By definition, liposomes have at least one bilayer, although certain preparation conditions may favour multilamellar systems with multiple stacked membranes like the layers of an onion; here the biomolecular layers of lipid are separated by aqueous layers, the thickness of which is modulated by repulsions between lipid headgroups [11]. Phosphatidylcholines are a naturally abundant class of phospholipid and contain two hydrophobic acyl hydrocarbon chains and a hydrophilic polar head group as shown in Figure 4.2.

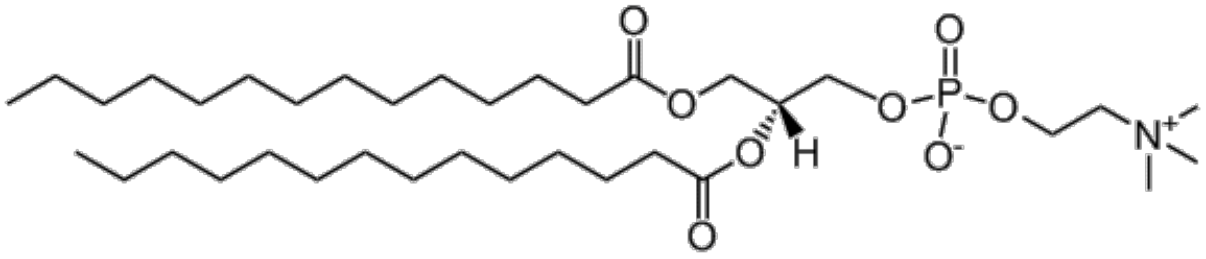


**Figure 4.2** The structure of a phosphotidylcholine (1,2- dimyristoyl-sn-glycero-3-phosphocholine).

Specifically, targeted drug delivery can be achieved using liposomes [12]. They are the ideal carriers for hydrophobic compounds and amphipathic compounds between the aqueous phase and the lipid membrane [12, 13]. Liposome have also been used for the delivery of dyes, pesticides to plants, cosmetic formulations and other materials [14].

Lipids can group together to form different structures which depend on different factors such as concentration, structure of the lipids and solution conditions. In the present work, we are mostly interested in lipid bilayers and liposomes. Lipid bilayers represent the natural, energetically favoured form of lipids when mixed with water or buffer. Van der Waals forces, electrostatic forces, hydrophobic interactions and hydrogen bonds can contribute to the formation of a lipid bilayer. Supported bilayers can occur on surfaces that are hydrophilic, where vesicles from a dispersion contacting the surface tend to fuse together to form a bilayer. This is because vesicles that are adsorbed on hydrophilic surfaces flatten and extend to maximise their contact with the surface, and eventually rupture to form the supported bilayer.

Such supported bilayer membranes are used as an experimental model to study protein and nanomaterial interactions with lipids. Lipid membrane interactions with nanoparticles and their possible toxicity is one vital area of research at a time when proliferation of nanomaterials for healthcare and technology is occurring at an unprecedented rate [15-17].

Structures of some typical phospholipids (used in our experiments) are shown in Figure 4.3. POPC is the most common phospholipid used to mimic the mammalian cell bilayer due to its widespread role in biological membranes and highly consistent and reproducible properties.

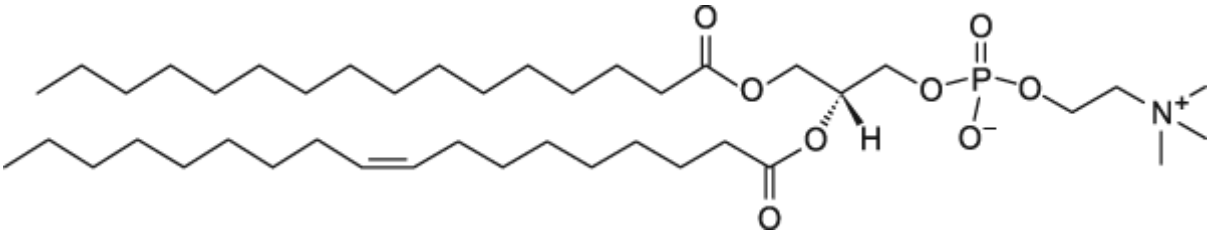

1-palmitoyl-2-oleoyl-*sn*-glycero-3-phosphocholine (POPC)

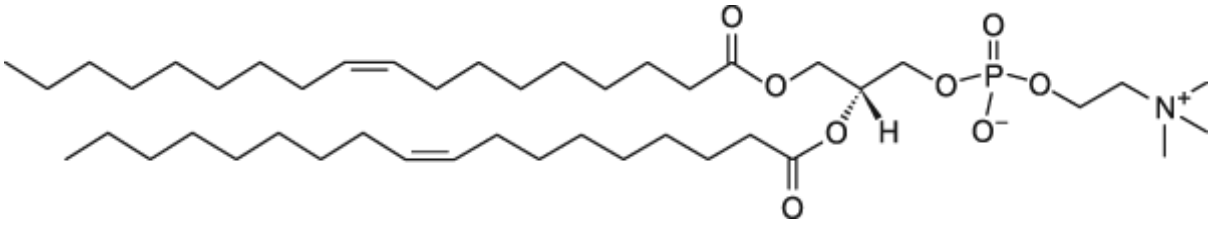

1,2-dioleoyl-**sn**-glycero-3-phosphocholine (DOPC)

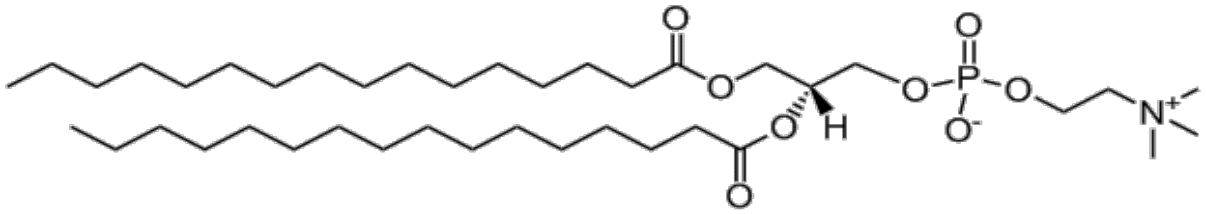

1-palmitoyl-2-oleoyl-**sn**-glycero-3-phospho-L-serine (sodium salt) (POPS)

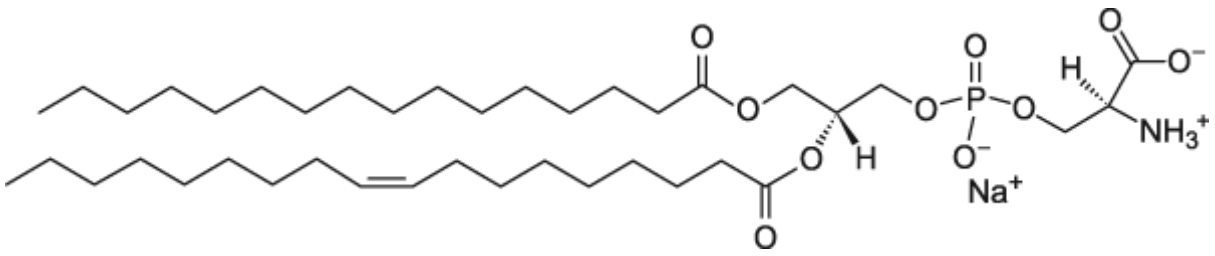

1,2-dipalmitoyl-sn-glycero-3-phosphocholine (DPPC)

**Figure 4.3**: Chemical structures of the phospholipids used in this work. POPC, DOPC and DPPC are all zwitterionic phospholipids that have different acyl chain lengths, and a mixture of saturated and unsaturated chains as shown. POPS is a negatively charged phospholipid that is mixed with POPC to produce anionic liposomes.

## 4.2. Graphene, Graphene Oxide and Reduced Graphene Oxide

Graphene is a single layer of graphite that has unique mechanical, electrical and optical properties. It is a one atom thick planar sheet of $sp^2$ hybridized carbon atoms that shows a unique combination of electrical, thermal and mechanical properties [18]. Usually, a carbon atom offers its four outer shell electrons for bonding. However, carbon atoms in graphene are bonded to three other carbon atoms with very strong covalent bonds, resulting in delocalisation of electrons that results in exceptional conductivity within the basal plane. Graphite is a 3D crystal lattice structure formed by stacking parallel 2D graphene sheets. The adjacent graphene sheets are held together by van der Waals forces, and graphene sheets achieve their lowest energy state when completely flat [19].

Graphene sheets tend to form aggregates in solvents (notably water) because of strong intermolecular van der Waals interactions and the material's high specific surface area [19]. Graphene has been a subject of intense research since its isolation by Novoselov *et al.* in 2004. It exhibits novel physiochemical properties such as high fracture toughness, thermal conductivity, Young's modulus and electrical conductivity [20, 21]. Graphene nanosheets have been adapted for variety of applications including in biomedicine, energy storage, nano-devices, renewable energy and sensing applications [22, 23]. However, to date very few research groups have used graphene to study membrane interactions. Instead, graphene oxide (GO) and reduced graphene oxide (rGO) are largely used as model graphene materials as they are readily available, easy to produce, and much more stable in aqueous systems.

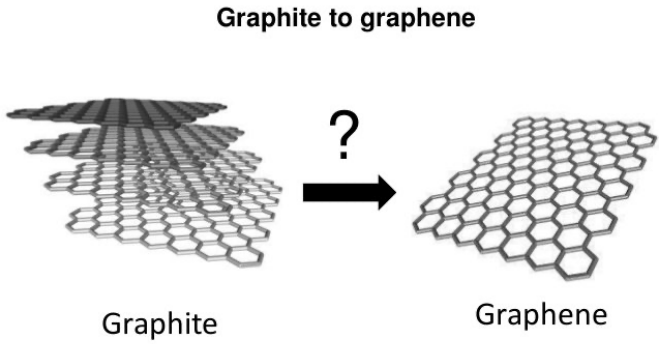


**Figure 4.4:** Each layer of Graphite is made up of carbon atoms linked together in a hexagonal lattice. The carbon atoms are linked together by $sp^2$ hybridised bonds in a single layer of atoms. A single layer of graphite is known as graphene. Graphite is a very brittle compound and may not be useful as a structural material on its own. However, graphene is one of the strongest known materials. Monolayer graphene sheets can be produced by mechanical exfoliation of graphite or by chemical vapour deposition.

Graphene oxide (GO) is an oxidised form of graphene, normally produced by exfoliation of graphite in highly oxidising conditions. It is negatively charged due to the presence of carboxylic acid groups around the periphery of its sheets and is rendered hydrophilic due to hydroxyl and epoxy functionalities that decorate its basal plane. Graphene oxide (GO) promises to be an alternative to graphene because it is easier and cheaper to synthesise via the oxidation of graphite. It can be manipulated more easily due to its dispersibility in many common solvents including water, and GO sheets can be further chemically functionalised, or reduced back to a graphene-like material (reduced graphene oxide, rGO). GO is not chemically similar to graphene, having very different chemistry and physical properties. However, reduced graphene oxide resembles graphene structure and it is essential to understand biomimetic membrane interactions with both GO and rGO.

The high surface area and the amphiphilicity of GO makes it an ideal substrate for biosensors, environmental and biomedical applications. Recent work has shown that carbon based fluorescent materials show greater stability, biocompatibility, and lower toxicity [24, 25]. If these materials were to be used in our day to day lives, their interaction with live cells and membranes needs to be better understood. We aim to study their interaction with

biomimetic membranes extensively in order to better understand the affects they will have on living cells and thereby the environment.

Graphite is a naturally occurring material, and graphene (a single layer of graphite), oxidised graphene (graphene oxide) and reduced GO (rGO) are still being studied to better understand their interaction with the membrane and their cytotoxicity. It has been seen that GO can cross cell membranes easily, and its high surface area provides multiple sites for drug targeting [26, 27]. Due to electrostatic interactions, several studies suggest that positively charged lipids have higher affinity with GO compared to the negatively charged lipids [28-30]. GO sheets have been shown to induce rupture of liposomes, which initiates the formation of fragmentary or supported bilayers and potentially lipid-graphene layers [29]. Previous studies using quartz crystal microbalance with dissipation monitoring have shown that GO induces the rupture of liposomes and results in a formation of bilayers [31].

Liposomes also serve as a simple model system for the biological membrane that is amenable for use in bulk (as opposed to surface) measurements. With the widespread use of nanoparticles in our daily lives and environment, understanding their interaction with the cell membrane is of the utmost importance, whether it is to be able to assess their risks (toxicity) or their benefits in nanomedicine. For this reason, it is necessary to understand the dynamics of nanoparticle interactions with membranes, along with structural and transport features. Proteins, polymers and nanoparticles are known to interact with lipid bilayers or lipid vesicles in various ways, intercalating into the membrane, hosting in the vesicle or causing vesicle rupture [32, 33]. Fundamental understanding of these interactions is critically important to identifying the drug and gene delivery capabilities of composite systems.

In the last decade, graphene-based materials have been an intense area of research and the area of its applications are wide [34]. Graphene and its derivatives have many desirable properties such as high surface area, its electrical conductivity, low cost, bio

compatibility and ability to further functionalise it [35, 36]. The oxidised layers of graphite oxide can be exfoliated in ultrasonication to produce a few layers of carbon atoms which is called Graphene Oxide [37]. GO are inexpensive and abundant, and it is easily dispersible in water. GO can also be reduced to Graphene like sheets by reducing the oxygen containing groups[38]. GO/rGO has both been studied and can be potentially used for biosensing applications, early detection of diseases and detecting other relevant biological molecules in humans [39-41]. GO has been successfully used in biosensors for the detection of DNA and protein [42]. Both rGO and GO can be functionalised to be used in different applications. Functionalised rGO has been used as a semi-conductor in biosensors to detect catecholamine molecules, avidin and DNA [43-45]. GO has been studied to be used in different biomedical applications, in water purifications among some of the applications [46-48]. These nanomaterials have been a target to be used in different biomedical applications, its essential to understand how they interact with cell membrane. In our study we will be using biomimetic membranes and liposomes to study how GO and rGO interact with the cell membrane.

### 4.3. Aims:

In the next two chapters, we hope to gain a more complete understanding of the interactions of GO and rGO with lipid membranes using AFM and scattering measurements. The interactions between supported lipid bilayers, liposomes and nanoparticles are of particular interest, as bilayers and liposomes can serve as a model system for biological cells. Lipid bilayer and liposome integrity will be explored in the presence of both GO and rGO, and the charges in the size and structure of liposomes (zwitterionic, different carbon chain length and anionic) will be varied to better understand the interactions responsible for structural changes. We wish to determine the average radius, polydispersity, and the

thickness of the hydrophobic and hydrophilic parts of the bilayer before and after the addition of GO and rGO, along with overall liposome integrity, to develop an understanding of how nanomaterial chemistry affects interactions with lipids.

## 4.4 References


1. Freedman, J.C., Chapter 3 - Cell Membranes, in Cell Physiology Source Book (Fourth Edition), N. Sperelakis, Editor. 2012, Academic Press: San Diego. p. 49-59.
2. Nielsen, J.S.H.a.C.H., Creating Scalable and Addressable Biomimetic Membrane Arrays in Biomedicine. Advances in Biomimetic, ed. A. George. 2011: Intech.
3. Kiessling, V., S.T. Yang, and L.K. Tamm, Supported lipid bilayers as models for studying membrane domains. Curr Top Membr, 2015. **75**: p. 1-23.
4. van der Veen, J.N., *et al.*, The critical role of phosphatidylcholine and phosphatidylethanolamine metabolism in health and disease. Biochim Biophys Acta Biomembr, 2017. **1859**(9 Pt B): p. 1558-1572.
5. Perrie, Y. and T. Rades, Themed issue: improve dissolution, solubility and bioavailability of poorly soluble drugs. J Pharm Pharmacol, 2010. **62**(11): p. 1517-8.
6. Enoch, H.G., P.J. Fleming, and P. Strittmatter, The binding of cytochrome b5 to phospholipid vesicles and biological membranes. Effect of orientation on intermembrane transfer and digestion by carboxypeptidase Y. J Biol Chem, 1979. **254**(14): p. 6483-8.
7. Enoch, H.G. and P. Strittmatter, Formation and properties of 1000-A-diameter, single-bilayer phospholipid vesicles. Proc Natl Acad Sci U S A, 1979. **76**(1): p. 145-9.
8. Pagano, R.E. and J.N. Weinstein, Interactions of liposomes with mammalian cells. Annu Rev Biophys Bioeng, 1978. **7**: p. 435-68.
9. Torchilin, V.P., Fluorescence microscopy to follow the targeting of liposomes and micelles to cells and their intracellular fate. Adv Drug Deliv Rev, 2005. **57**(1): p. 95-109.
10. Akbarzadeh, A., *et al.*, Liposome: classification, preparation, and applications. Nanoscale Res Lett, 2013. **8**(1): p. 102.
11. Bangham, A.D., M.M. Standish, and J.C. Watkins, Diffusion of univalent ions across the lamellae of swollen phospholipids. J Mol Biol, 1965. **13**(1): p. 238-52.
12. Deshpande, P.P., S. Biswas, and V.P. Torchilin, Current trends in the use of liposomes for tumor targeting. Nanomedicine (London, England), 2013. **8**(9): p. 1509-1528.
13. Bozzuto, G. and A. Molinari, Liposomes as nanomedical devices. International journal of nanomedicine, 2015. **10**: p. 975-999.
14. Simão, A.M.S., *et al.*, Liposomal systems as carriers for bioactive compounds. Biophysical reviews, 2015. **7**(4): p. 391-397.
15. Heikkila, E., *et al.*, Atomistic simulations of anionic Au144(SR)60 nanoparticles interacting with asymmetric model lipid membranes. Biochim Biophys Acta, 2014. **1838**(11): p. 2852-60.
16. He, X.C., *et al.*, Advances in studies of nanoparticle-biomembrane interactions. Nanomedicine (Lond), 2015. **10**(1): p. 121-41.
17. Karlsson, H.L., *et al.*, Cell membrane damage and protein interaction induced by copper containing nanoparticles--importance of the metal release process. Toxicology, 2013. **313**(1): p. 59-69.
18. Dreyer, D.R., *et al.*, The chemistry of graphene oxide. Chem Soc Rev, 2010. **39**(1): p. 228-40.
19. Stankovich, S., *et al.*, Graphene-based composite materials. Nature, 2006. **442**(7100): p. 282-6.
20. Geim, A.K. and K.S. Novoselov, The rise of graphene. Nat Mater, 2007. **6**(3): p. 183-91.

21. Tombros, N., *et al.*, Electronic spin transport and spin precession in single graphene layers at room temperature. Nature, 2007. **448**(7153): p. 571-4.
22. Hollister, S.J., Porous scaffold design for tissue engineering. Nat Mater, 2005. **4**(7): p. 518-24.
23. Holzinger, M., A. Le Goff, and S. Cosnier, Nanomaterials for biosensing applications: a review. Front Chem, 2014. **2**: p. 63.
24. Bhunia, S.K., *et al.*, Carbon nanoparticle-based fluorescent bioimaging probes. Sci Rep, 2013. **3**: p. 1473.
25. Liu, J., R. Li, and B. Yang, Carbon Dots: A New Type of Carbon-Based Nanomaterial with Wide Applications. ACS Central Science, 2020. **6**(12): p. 2179-2195.
26. Chung, H.T., J.H. Won, and P. Zelenay, Active and stable carbon nanotube/nanoparticle composite electrocatalyst for oxygen reduction. Nat Commun, 2013. **4**: p. 1922.
27. Krishna, K.V., *et al.*, Graphene-based nanomaterials for nanobiotechnology and biomedical applications. Nanomedicine (Lond), 2013. **8**(10): p. 1669-88.
28. Li, S., *et al.*, Head Groups of Lipids Govern the Interaction and Orientation between Graphene Oxide and Lipids. The Journal of Physical Chemistry C, 2013. **117**(31): p. 16150-16158.
29. Frost, R., *et al.*, Graphene oxide and lipid membranes: interactions and nanocomposite structures. Nano Lett, 2012. **12**(7): p. 3356-62.
30. Huang, P.J., F. Wang, and J. Liu, Liposome/Graphene Oxide Interaction Studied by Isothermal Titration Calorimetry. Langmuir, 2016. **32**(10): p. 2458-63.
31. Frost, R., *et al.*, Graphene Oxide and Lipid Membranes: Size-Dependent Interactions. Langmuir, 2016. **32**(11): p. 2708-17.
32. Jackman, J.A., *et al.*, Rupture of lipid vesicles by a broad-spectrum antiviral peptide: influence of vesicle size. J Phys Chem B, 2013. **117**(50): p. 16117-28.
33. Lee, Y.K., H. Lee, and J.-M. Nam, Lipid-nanostructure hybrids and their applications in nanobiotechnology. NPG Asia Materials, 2013. **5**(5): p. e48-e48.
34. Tiwari, S.K., *et al.*, Current Research of Graphene-Based Nanocomposites and Their Application for Supercapacitors. Nanomaterials (Basel), 2020. **10**(10).
35. Jiang, H., Chemical preparation of graphene-based nanomaterials and their applications in chemical and biological sensors. Small, 2011. **7**(17): p. 2413-27.
36. Guo, S. and S. Dong, Graphene nanosheet: synthesis, molecular engineering, thin film, hybrids, and energy and analytical applications. Chem Soc Rev, 2011. **40**(5): p. 2644-72.
37. Novoselov, K.S., *et al.*, Electric field effect in atomically thin carbon films. Science, 2004. **306**(5696): p. 666-9.
38. Eda, G. and M. Chhowalla, Chemically derived graphene oxide: towards large-area thin-film electronics and optoelectronics. Adv Mater, 2010. **22**(22): p. 2392-415.
39. Sharma, D., *et al.*, Insight into the biosensing of graphene oxide: Present and future prospects. Arabian Journal of Chemistry, 2016. **9**(2): p. 238-261.
40. Szunerits, S. and R. Boukherroub, Graphene-based biosensors. Interface Focus, 2018. **8**(3): p. 20160132.
41. Bai, Y., T. Xu, and X. Zhang, Graphene-Based Biosensors for Detection of Biomarkers. Micromachines (Basel), 2020. **11**(1).
42. Lu, C.H., *et al.*, A graphene platform for sensing biomolecules. Angew Chem Int Ed Engl, 2009. **48**(26): p. 4785-7.
43. Cai, B., *et al.*, Ultrasensitive label-free detection of PNA-DNA hybridization by reduced graphene oxide field-effect transistor biosensor. ACS Nano, 2014. **8**(3): p. 2632-8.

44. He, Q., *et al.*, Centimeter-long and large-scale micropatterns of reduced graphene oxide films: fabrication and sensing applications. ACS Nano, 2010. **4**(6): p. 3201-8.
45. He, Q., *et al.*, Transparent, flexible, all-reduced graphene oxide thin film transistors. ACS Nano, 2011. **5**(6): p. 5038-44.
46. Buelke, C., *et al.*, Graphene oxide membranes for enhancing water purification in terrestrial and space-born applications: State of the art. Desalination, 2018. **448**: p. 113-132.
47. Hazell, G., *et al.*, Responsive materials based on magnetic polyelectrolytes and graphene oxide for water clean-up. J Colloid Interface Sci, 2016. **464**: p. 285-90.
48. McCoy, T.M., *et al.*, Noncovalent magnetic control and reversible recovery of graphene oxide using iron oxide and magnetic surfactants. ACS Appl Mater Interfaces, 2015. **7**(3): p. 2124-33.

# Chapter 5. Interactions of biomimetic membranes with carbon nanomaterials: graphene oxide (GO) and reduced graphene oxide (rGO)

## 5.1 Introduction

Carbon nanomaterials are being widely studied for their potential applications in biomedical and biological fields, including as scaffolds, in drug delivery, as sensors and emitters for bio-imaging, *etc.* [1-3]. However, the interaction of carbon nanomaterials with biological molecules including proteins and biological membranes needs to be addressed before any of these applications can be achieved [4, 5]. Little is known about the specific interaction of carbon nanomaterials (CNMs) with cell membranes. In the present chapter, we address some of these fundamental questions regarding the interaction of carbon nanomaterials (specifically graphene oxide, GO, and reduced graphene oxide, rGO) with biomimetic membranes using AFM imaging and force spectroscopy measurements.

### 5.1.1 Carbon nanomaterials

Graphene consists of one-atom thick, planar $sp^2$ hybridized carbon atoms, and it has attracted researchers for its novel optical, electronic, thermal and biological properties [6, 7]. Graphene oxide, an oxidized form of graphene is similar in structure, but it possesses oxygen containing functional groups such as carboxyls on the edges and hydroxyls and epoxies on the basal plane [6, 8]. GO is therefore a 2D atomically thin carbon nanomaterial and has extremely large surface area, high water dispersibility and excellent biocompatibility [9]. It has been the focus of researchers in the fields of biosensing and biomedical applications due to its low manufacturing cost, colloidal dispersibility, high adsorption capacity and fluorescence quenching [10, 11]. Recent studies suggest that carbon nanomaterials (including GO) could be applied for cellular imaging, drug and gene delivery [12]. Exploration of GO for drug delivery has included functionalization with chitosan, folic

acid and poly(N-isopropylacrylamide), demonstrating pH-controlled or thermally responsive drug release [13-16].

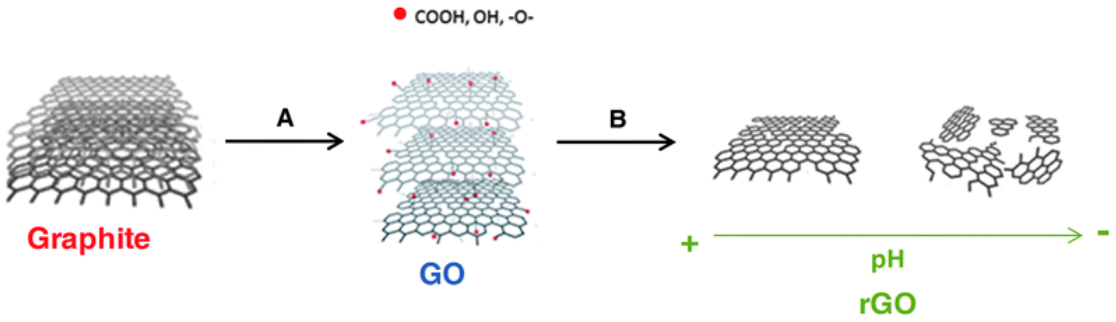


**Figure 5.1** Schematic representation of graphite, GO and rGO. Graphite comprises only stacked layers of carbon sheets. Graphene oxide bears oxygen-containing groups like COOH, OH and -O- and can be dispersed in water easily. Reduced graphene is closely related to graphene, though may retain irreversible deformation and some oxygen containing groups [17]. This figure was reproduced from Bisch-Navarro et al. [17].

### 5.1.2 Atomic Force Microscopy (AFM) for lipid studies

Lipid molecules in cell membranes are amphipathic, meaning that they have both hydrophobic groups (acyl chains) and hydrophilic groups (e.g. a polar head group). This is crucial for their self-assembly into different structures including bilayers. One abundant class of zwitterionic glycerolipids in animal cell membranes is phosphatidylcholines (PCs), which have two acyl chains and are appropriate model molecules for investigating the surface organization, properties and interactions of lipids with nanomaterials [18]. A model physical system that closely resembles the biological membrane is the supported lipid bilayer formed on a flat support (typically mica, as in our case) [19]. Supported lipid bilayers can be prepared with desired composition and their interaction with carbon nanomaterials can thereby be studied using AFM.

AFM is primarily used to examine surface morphology, topography, and mechanical properties, and is often used as a nano-scale imaging tool. However, the technique can also be used to measure interaction forces between the sharp tip of a micro machined cantilever and a sample, in a mode known as force spectroscopy [19-22].

AFM 'sees' (or rather senses) the sample under investigation via the interaction of a sharp tip with the sample. This technique allows visualization of the sample with nanometre resolution [23]. To achieve this, a sharp AFM tip (radius of curvature ~10 nm) is mounted on the end of a long flexible cantilever, connected to a holder [24, 25]. The back surface of the cantilever is highly reflective, and a beam from a laser diode is directed at the back of the cantilever toward the end where the tip is located [26]. The slightest movement of the tip in the z direction will change the position of the reflected laser beam at a position-sensitive diode, creating a differential voltage signal, used by the AFM to maintain the z-position of the tip via a feedback loop. To perform a measurement, the tip is brought into contact with the sample, and the electronics of the AFM keep the force between the tip and the sample constant at each point by moving the cantilever in the z direction with sub-nanometre precision using a piezoelectric element [26]. By plotting the cantilever motion thus induced by the feedback loop, the AFM height image of the surface is obtained.

In alternating contact (AC or 'tapping') mode, the surface is scanned by a cantilever that is oscillated at or near its resonance frequency, thereby making intermittent contact with the sample surface [27]. Therefore, tapping mode is often preferred for imaging delicate biological samples [28]. Changes in the AFM scanner height in response to modulation of the cantilever oscillation amplitude by interaction with the surface thus generate a topographic image [29].

Using this same remarkable force and positioning sensitivity, the AFM tip can be used to either compress or extend (pull) target molecules within the investigated sample in a controlled manner. The z-position of the cantilever is known at all times, and the spring constant of the cantilever can be determined; the force that the tip exerts on the sample can therefore be calculated.

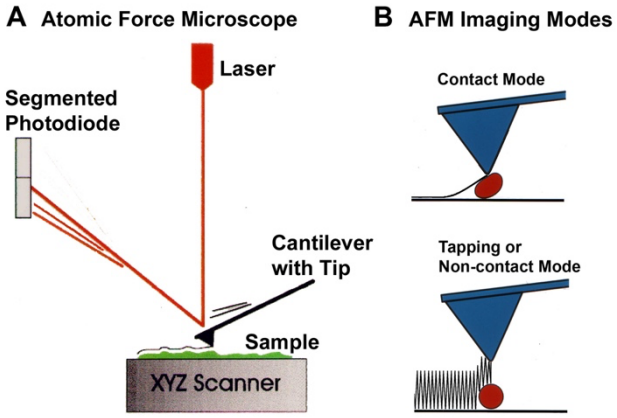


**Figure 5.2 A**) Schematic representation of AFM. **B**) Different imaging modes used in the experiment. Contact mode (top) and tapping mode (bottom).

When used as a force-measuring device, the tip of the cantilever is positioned over the surface of the sample. The tip approaches the sample, makes contact and pushes until a predetermined force or position in the z direction is reached, before retracting. The known positional change of the cantilever along with its measured deflection (force) is used to generate a force-distance curve. According to Hooke's law, the force exerted by the tip on the sample, *F*, is given by:

$$F = dk$$

where *d* is the displacement of the tip and *k* is the spring constant of the cantilever.

When we exert a force on the sample, we can use the tip as a tool to probe local mechanical properties of the sample, such as elasticity, or the force needed to penetrate through the sample. This is of particular relevance to the study of lipid membranes, where we can determine the force needed to penetrate through a bilayer.

## 5.2 Objective

The overarching goal of this piece of work is to investigate the interaction of graphene oxide (GO), reduced graphene oxide (rGO) with lipid bilayers and liposomes. We will explore the physical and chemical basis for the assembly and morphological effects seen through atomic microscopy imaging and force spectroscopy. In order to study carbon nanomaterial interactions with biomimetic membranes, it is first necessary to stably adsorb the membranes on a substrate (mica in our case). Over the years, considerable efforts have been made to examine the properties of natural and synthetic lipid bilayers adsorbed on surfaces, and the literature provides useful protocols to enable us to reliably create model samples for analysis [20]. Nanomaterials can then be reconstituted in a relevant lipid bilayer in order to study their interaction with the membrane. High resolution imaging of the surface of the nanomaterials and bilayer, along with direct measurements of interactions via force spectroscopy will be performed with a JPK Nanowizard 3 AFM.

## 5.3. Experimental design and methodology

### 5.3.1 Phospholipids

Phospholipids used in this study were 1,2-dioleoyl-sn-glycero-3-phosphocholine (DOPC), 1-palmitoyl-2-oleoyl-**sn**-glycero-3-phosphocholine (POPC), 1-palmitoyl-2-oleoyl-**sn**-glycero-3-phosphocholine (POPC) : 1-palmitoyl-2-oleoyl-**sn**-glycero-3-phospho-L-serine (sodium salt) (POPS) (in a 3:1 molar ratio, giving a net negatively charged combination) and 1-palmitoyl-2-oleoyl-**sn**-glycero-3-phosphocholine (POPC) : 1-palmitoyl-

2-oleoyl-**sn**-glycero-3-ethylphosphocholine (chloride salt) (POEPC) (in a 3:1 molar ratio,

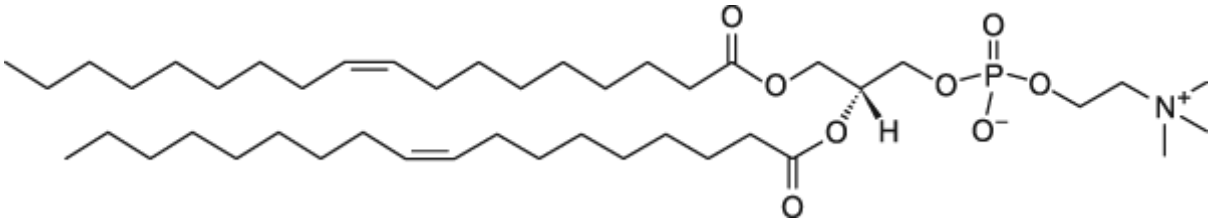

giving a net positively charged combination).

**1,2-dioleoyl-sn-glycero-3-phosphocholine (DOPC)**

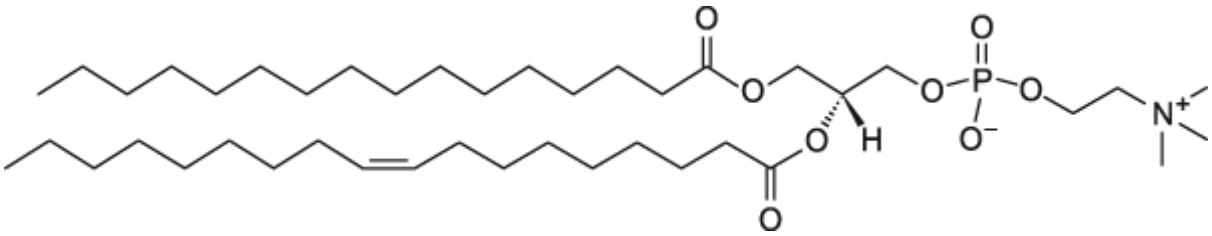

**1-palmitoyl-2-oleoyl-sn-glycero-3-phosphocholine (POPC)**

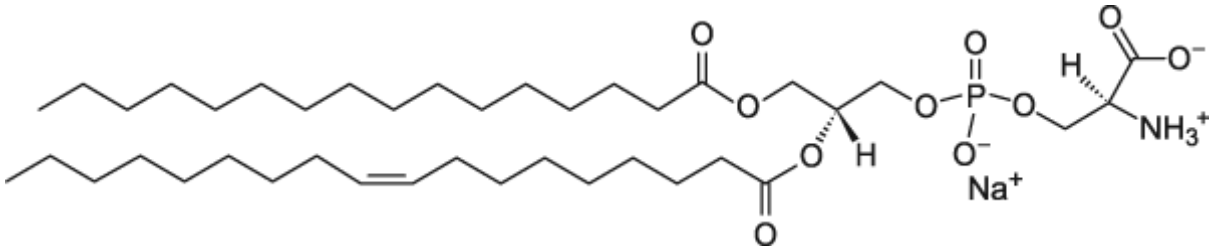

**1-palmitoyl-2-oleoyl-sn-glycero-3-phospho-L-serine (sodium salt) (POPS)**

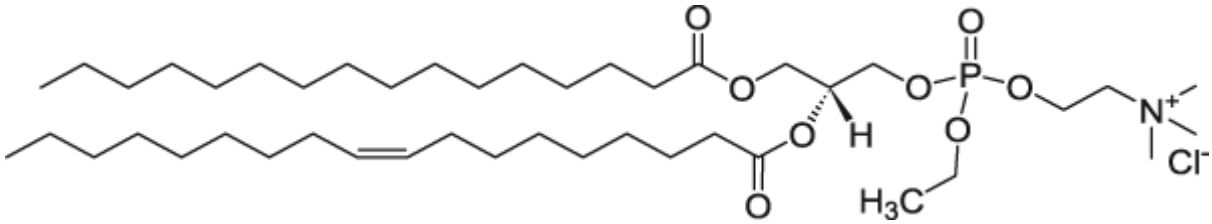

**1-palmitoyl-2-oleoyl-sn-glycero-3-ethylphosphocholine (chloride salt) (POEPC)**

**Figure 5.3** Phospholipids used in this study. DOPC and POPC are zwitterionic phospholipids. POPS is a negatively charged lipid and POEPC is a positively charged lipid.

### 5.3.2 Liposome Preparation

A 20 mg/mL solution of lipid(s) in chloroform (Avanti Polar Lipids) was divided into 1 mL aliquots. A glass syringe was used to transfer the solution to small glass vials. Plastic pipette tips are not recommended since the lipids are in chloroform. By dividing the solution up into batches, we minimized the variations in lipid concentration since chloroform evaporates over time, even when sealed using, e.g. Parafilm. The 1 mL lipid solutions were stored in a –20ºC freezer. The protocol for small, unilamellar vesicle (SUV) preparation is adapted from the literature [30]. Typically, the 1 mL aliquots were dried in a glass vial under a stream of nitrogen followed by vacuum for a few hours.

The dried lipids were hydrated in water (in some experiments Tris buffer was used) to a lipid concentration of 5 mg/mL. The lipid solution was passed through a 100 nm pore membrane (18×) in an extruder. Vesicles were characterized by dynamic light scattering (DLS) to determine their size (generally ~115 nm directly after the extrusion process) and for polydispersity. The samples were mostly diluted to 0.4 mg/mL for AFM and QCM studies. Samples used in FTIR studies were 7 mg/mL.

### 5.3.3 Quartz Crystal Microbalance and Dissipation (QCM-D)

QCM-D is a sensitive technique that measures change in mass and change in dissipation (an indirect measurement of viscoelasticity) of the biomimetic membrane when adsorbed to a solid surface. The changes in mass and viscoelasticity are detected as deviations in frequency (f) and dissipation (D) of the pulsed oscillation (clock) frequency of a silicon crystal sensor. Liposomes are deposited on the silicon sensor, and by exchanging the buffer to induce a chance in ionic strength, osmotic bursting of the liposomes is induced,

forming a flat biomimetic lipid membrane on the crystal surface. We studied the interaction of GO and rGO with biomimetic membranes thus formed.

### 5.3.4 Attenuated total reflectance – Fourier-transform infrared spectroscopy (ATR-FTIR)

FTIR can be used to characterize the chemical identity of species by interrogation of vibrations of the bonds present. FTIR of phospholipids exhibits specific vibrational characteristics that represent the chemical groups present within these molecules. The spectra of phospholipids in the presence of GO and rGO may change in absorption intensities, and a shift of absorption spectra particularly in the $CH_2$ region. Attenuated total reflectance (ATR) is a manifestation of FTIR spectroscopy in which an evanescent wave generated at a surface by total internal reflection of the IR beam inside a solid crystal is used to probe material adsorbed at that surface. ATR-FTIR is thereby sensitive to the chemical identity of materials specifically adsorbed on the crystal, with sensitivity decreasing exponentially away from the crystal surface, giving a typical 'working depth' on the order of 1 μm. By combining a surface-sensitive technique such as ATR-FTIR with AFM and QCM-D, we hope to paint a clear picture of GO and rGO interactions with biomimetic membranes.

## 5.4 Results

### 5.4.1 AFM imaging of lipid bilayer in AC mode

Lipid bilayers in aqueous environment tend to exhibit fluid characteristics and are thereby very difficult to get a good resolution AFM image of. Initially, we worked with dried lipid samples to make sure that we could deposit liposomes on mica surfaces and successfully image the dried sample. The samples were either drop-casted or spin coated. The concentration of the lipid solutions used for these AFM studies was 0.4 mg/mL. Different

lipid concentrations were trialled, but in our case 0.4 mg/mL seemed to be the most effective concentration to facilitate the study of GO and rGO interactions with the lipid bilayers, providing sufficient coverage for a supported bilayer without significant multiple stacking of lipid layers on the surface. Initially, we needed to make sure that the liposomes were depositing on the mica surface.

A. B.

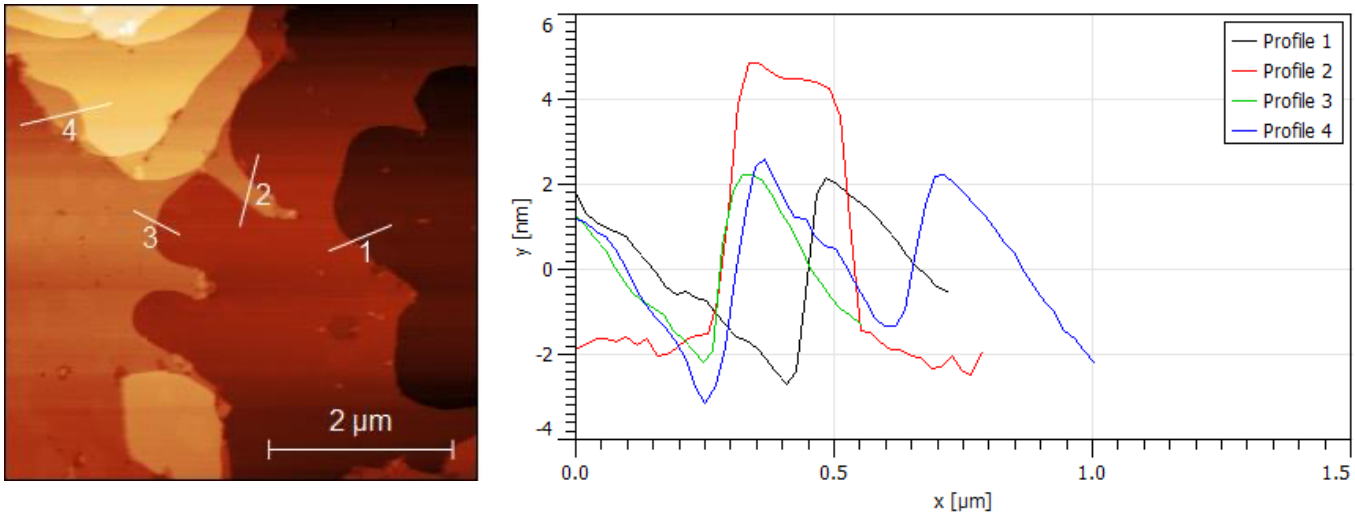


**Figure 5.4** AFM images of DOPC drop-casted, rinsed with water after 60 minutes, dried and imaged in AC mode. A) multiple layers of lipid are seen in the height image. The cross-sectional height profiles shown in B) suggest that these layers are anywhere from 4 to 6 nm, which is consistent with the height of a single bilayer.

Small aliquots of liposome dispersion were drop-casted onto a mica surface and left to settle for about 20 mins before being rinsed with water to get rid of excess lipid from the surface. The sample was then imaged using AFM in alternating contact (AC) mode in order to understand the deposition morphology of the liposomes on the mica surface. Once washed with the water, the samples were left to dry before imaging. Although the dry sample may not be morphologically identical to the hydrated (wet) state, in this instance the dry image

provides a robust method to obtain useful information as to the adsorbed lipid morphology on the surface.

As seen in Figure 5.4.A, liposomes were deposited forming incomplete multilayers on the mica surface. As samples were drop casted, the multilayer surface was not smooth, and some areas on the mica surface appear to have more layers of lipids than others. However, we could clearly image the multilayer lipids deposited on the surface. Figure 5.4.B shows selected cross-sectional height profiles taken from the deposited layer of lipids. Each layer of the deposition is about 4 to 6 nm, and this is consistent with literature values for the thickness of a lipid bilayer [20].

### 5.4.2 Imaging of lipid bilayers in liquid using contact mode AFM

Our ultimate goal was to study the interaction of graphene oxide (GO) and reduced graphene oxide with the bilayer (or multilayer) in a liquid medium. For that reason, the next step was to image bilayers (or multilayers) in liquid. Liposome dispersions (0.4 mg/mL) were incubated on a mica surface for around 20 minutes and excess dispersion was washed off. Instead of letting the surface dry in order to image it, the glass slide containing the mica sheet was placed instead immediately into a Petri dish containing water. The lipid layer was thereby submerged without having fully dehydrated. We expected that the bilayer (or the multilayer) will have cracks because of the de-wetting. Initially, liposomes were washed off with water and for a few seconds (between washing and placing it in the petri dish) the samples were not submerged in water. This results in cracks within the bilayer, and this technique can be used to identify the presence of the bilayer, as a perfectly smooth and featureless bilayer is morphologically similar to the underlying substrate when imaged using AFM. Force measurements can also be used to identify the presence of bilayer (or

multilayer) features and can be used to measure the height of the lipid bilayers (as described later).

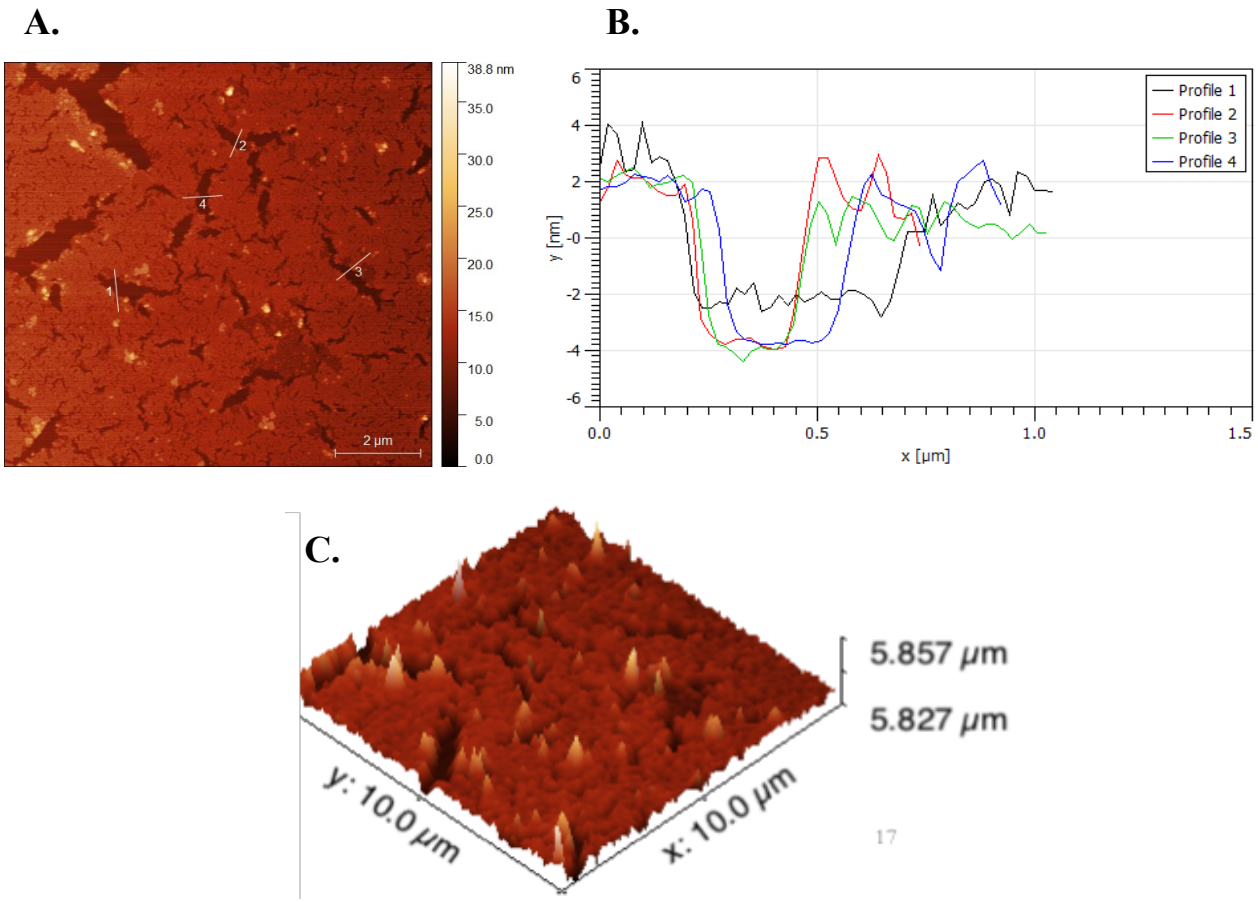


**Figure 5.5** AFM images of DOPC liposome dispersions drop-casted, rinsed with water after 30 mins and placed in a Petri dish containing water. Samples were imaged in contact mode. A) Lipid bilayer showing cracks in the bilayer. The integrity of the bilayer is compromised because of the cracks and this is likely caused by the de-wetting of the lipid bilayer. The line profiles shown in B) suggest that the layers are anywhere from 4 to 6 nm, which is consistent with the expected height of a bilayer. C) 3D reconstruction of the height data emphasising that the bilayer is not smooth.

As a result of initial test measurements, incubation time of the liposome dispersion on the mica surface was reduced to half hour from an hour. This change in incubation time resulted in a bilayer that appeared more uniform and did not have as much stacking as seen in the dried samples in Figure 5.5.A.

Initial AFM images confirmed that the bilayer or multilayer was providing approximately full coverage on the mica surface, and thus represented a suitably stable and measurable substrate for the investigation of the interaction of lipids with carbon nanomaterials. Thus, the research question could now be addressed: what happens to the lipid layer when GO or rGO is added to it?

### 5.4.3 Interaction between GO and supported lipid bilayer

When GO is introduced to a lipid membrane, one possible outcome is that lipid bilayers are pulled out of the surface, resulting in pore formation and deformation of the lipid bilayer. Here, DOPC biomimetic membranes were used to explore interactions with GO to better understand this effect. It is hypothesised that graphene oxide and reduced graphene oxide interaction with cell membranes may be dependent on the membrane lipid composition. Graphene oxide and reduced graphene oxide have been previously found to damage bacterial cell membranes through direct contact of the graphene edges with the membrane [31]. It has also been reported that graphene oxide and graphene solutions inhibit bacterial growth and that they can damage E. coli cell membranes [32]. Multiple studies suggest both GO and rGO exhibit cytotoxic properties when interacting with bacterial membranes [32]. Nanoparticles exhibit toxicity by disrupting cell membranes, cell damage with oxidative reactions, damage to nucleic acids, damage to proteins and mitochondrial function, and oxidative stress among other things. Further study is therefore essential to better understand GO's interaction with mammalian cells. Therefore, it is important to understand the nature of the interaction between graphene oxide (GO) and various lipids and bilayers.

A. B.

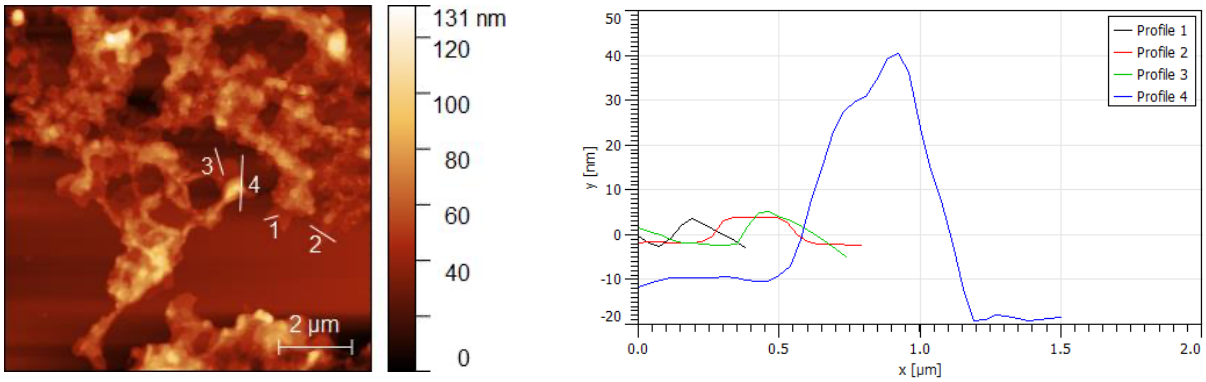


**Figure 5.6** AFM images of DOPC deposited from liposomes that were drop-cast, rinsed with water after 30 mins, incubated with GO for another 30 mins, rinsed and placed in a petri dish containing water. The sample was imaged in contact mode. A) Lipid bilayer showing a completely different structure to pure lipid bilayer (or pure GO sheets). The structure has the appearance of a nanocomposite of lipid and GO. The line profile shown in B) shows that the structure is not the height of a bilayer or the height of individual GO sheets; the height of the composite is several hundred nanometres.

The interaction between GO and a biomimetic DOPC membrane was observed using AFM. From previous literature, it was expected that the formation of layers of distinct graphene oxide on the membrane would be seen [33]. However, what we observed in the present work was quite different. The AFM images showed that the lipid membrane and GO were clumping together to form a nanocomposite structure with complex, convolved (and distinctly non-sheet like) morphology (Figure 5.6). Liposomes are understood to become adsorbed on mica, deform and rupture spontaneously to form a bilayer [34]. It is possible that excess liposomes could be ruptured when GO is introduced to the bilayer.

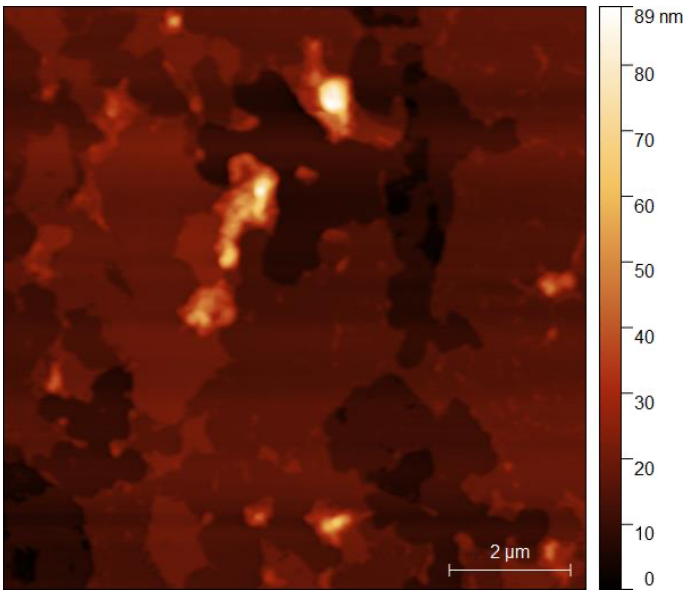


**Figure 5.7** Lipid used for this study was DOPC. Liposomes were drop-casted, rinsed with water after 30 mins, incubated with GO for another 30 mins, rinsed and placed in a petri dish containing water. Then, the sample was imaged in contact mode. The AFM image shows a completely different structure to just lipid bilayer or just GO sheets. The structure looks like a nanocomposite of bilayer and GO.

and form such a nanocomposite structure as observed here [35]. However, this does not explain the lipids having been stripped from the surfaces in much of the sample area, and so this must have been at least accompanied by graphene oxide interacting with the surface-adsorbed bilayer, grossly changing its morphology. For example, the height profile of the nanocomposite in Figure 5.6 suggests that multiple sections of bilayer have formed and clumped together, resulting in structures of different heights [35]. This most likely arises from formation of different multiples of lipid bilayers with graphene oxide layers between. It has been previously suggested that the driving force for the interaction and adsorption of graphene oxide is electrostatic in origin [35], and this may also be the basis for interactions with the lipid headgroups in the present work.

### 5.4.4 Exploration of DOPC and GO interactions using force spectroscopy

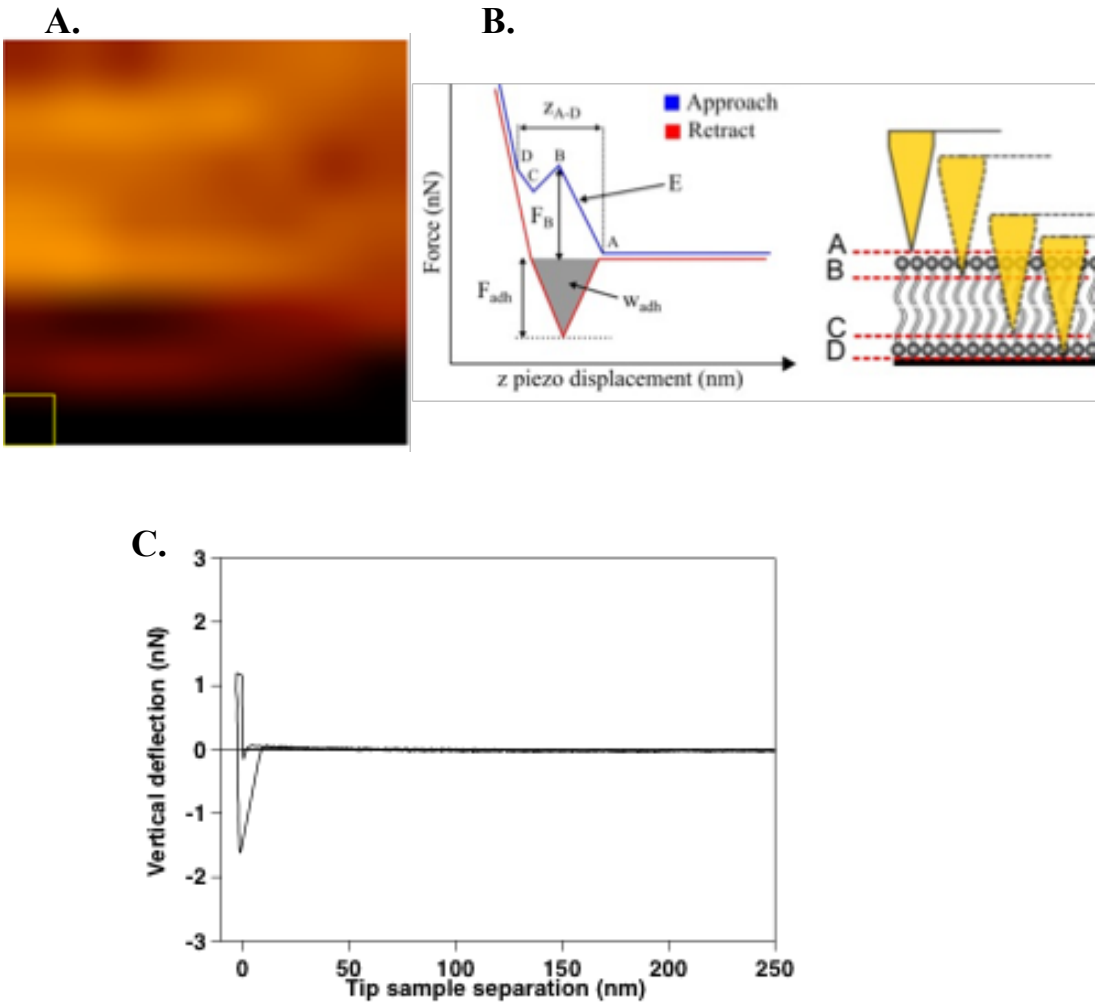


**Figure 5.8** Force curves can be used to calculate the mechanical properties such as adhesive energy, height of the lipid bilayer, Young's modulus, breakthrough force, *etc.* Force curves can also be used to determine the fluidity of a biomimetic membrane. A) Force mapping can be used to collect multiple force curves within a defined area. B) Schematic representation of a force curve with pertinent features labelled. This figure was Adapted from [20]. C) Example of a force curve from a POPC lipid layer without additives.

Mechanical properties of lipid bilayers can be studied using force spectroscopy undertaken with an AFM cantilever. Force mapping allowed us to collect multiple force curves within a

defined area of a sample. Adhesive force between the cantilever and surface (layer), height of the bilayer, and force required to break through the surface layer (breakthrough force) can be calculated from these force curves. Young's modulus (calculated using contact mechanics theory) and adhesion energy (area under the curve) are some other parameters that can be readily obtained from analysis of the force curves.

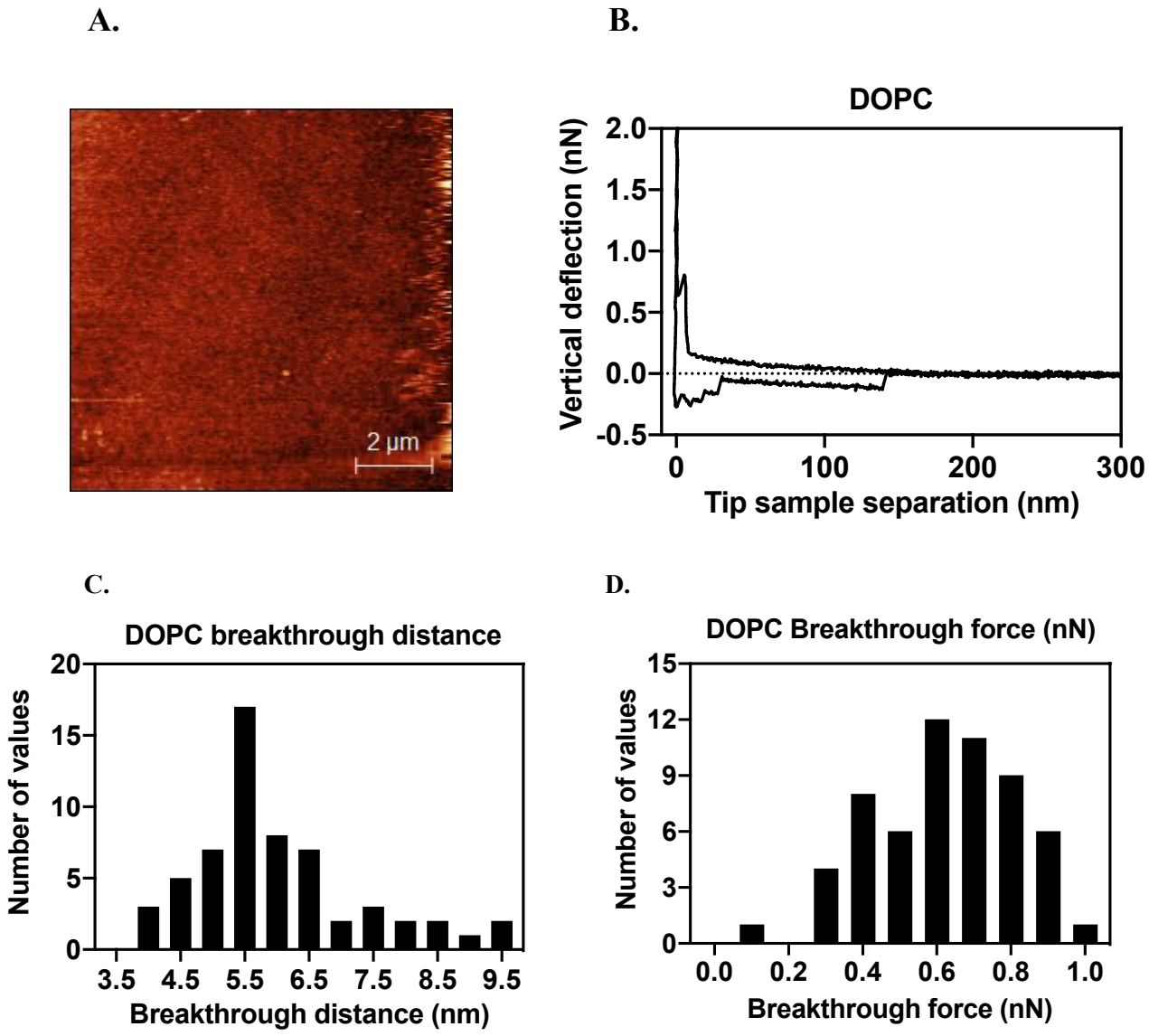


**Figure 5.9** Force curves can be used to calculate the mechanical properties such as adhesive energy, height of the lipid bilayer, Young's modulus, breakthrough force, *etc.* Force curves can also be used to determine the fluidity of a biomimetic membrane. A) AFM image of DOPC bilayer. B) Representative force curve from DOPC bilayer. C) Histogram of breakthrough distance of DOPC bilayer. D) Histogram of breakthrough force (*i.e.* the force

at which the AFM tip penetrated the bilayer). The data shown here is the average of 3 different experiments.

DOPC supported lipid bilayers were used as a model system to study topographical and biomechanical changes on interaction with carbon nanomaterials using AFM imaging and force spectroscopy. A typical AFM image of a DOPC bilayer is shown in Figure 5.9.A, and this indicates a very flat and comparatively featureless surface. The image looks very similar to the mica surface and it can be difficult to differentiate from the actual bilayer without further investigation. Here, force spectroscopy is used to make this distinction clear.

A representative force curve between a contact mode AFM cantilever and DOPC-coated mica surface (Fig. 5.9.B) clearly shows contact with the bilayer, rupture of the bilayer, direct contact between the tip and mica surface, and then significant adhesive events on retraction. The retraction shows multiple steps, and the AFM tip may be picking up lipids as it separates from the bilayer surface. Based on the force curve, breakthrough force (the force at which the bilayer ruptures and the AFM penetrates to the mica surface) and the breakthrough distance (bilayer depth or thickness) can be calculated. The histogram shown in Fig. 5.9C represents the rupture depth of the DOPC bilayer. From the average of the values obtained, the DOPC bilayer appears to be 5.5 nm in thickness, which is within the accepted range as reported in the literature [20, 36-38]. The height of phospholipid bilayers have been reported to be generally 4 to 6 nm, with slight variations based on the length of the carbon chain in the lipids, any water layer within the bilayer, and the compactness of the bilayer [36-38]. DOPC lipid bilayers exist in their fluid (chain melted) phase at room temperature, and the force required to break through the bilayer is commensurate with this at ~0.65 nN (range of 0.5-0.9 nN) as shown in Fig 5.9.D [20, 36-38].

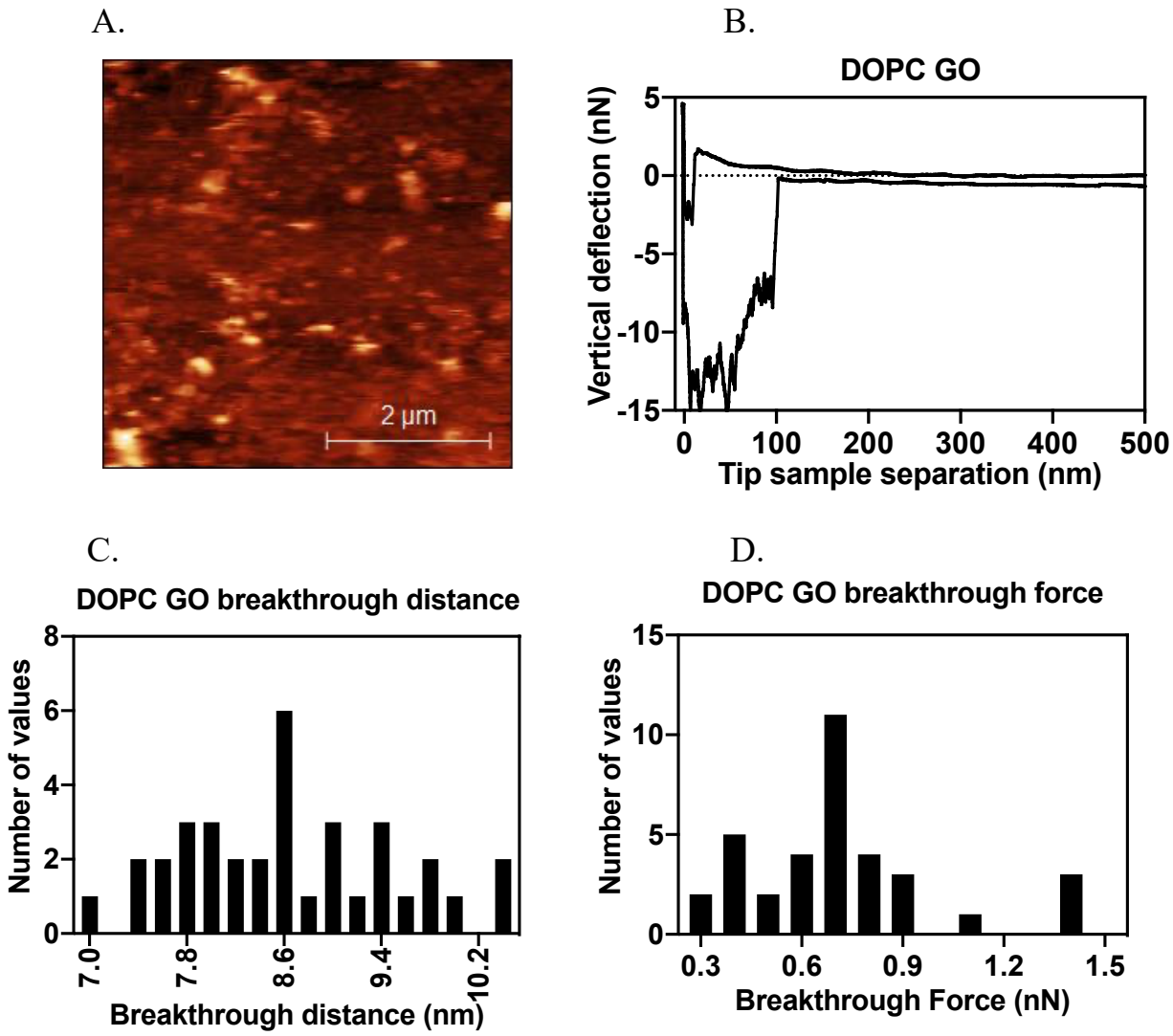


**Figure 5.10** DOPC supported lipid bilayer interaction with GO: A) AFM image of DOPC supporter bilayer interaction with GO obtained in liquid. B) Force curve of DOPC interaction with GO (in liquid). C, D) Histograms of DOPC bilayer thickness (C), and breakthrough force (D). The data shown here is the average of 3 different experiments.

AFM imaging (Figure 5.10.A) of the bilayer after incubation with GO shows the bilayer is no longer flat and appears to contain GO flakes. In this case, the surface looks more like a nanocomposite, but we cannot be certain based on the AFM image only. It is certainly morphologically very different to what was seen in the dried sample after interaction with

GO. Force curves between a sharp tipped cantilever and DOPC with GO show a breakthrough event at low force, and the retraction portion of the force curve shows a great number of poorly defined and highly adhesive events. This may be due to the different interactions between the nanocomposite structure and the cantilever, and appears to signify significant 'peeling' up of the surface material by the cantilever, as far as 100 nm from the surface itself (*i.e.* at least an order of magnitude greater distance than the bilayer itself would be expected to extend). It is clear that the bilayer does not have the same integrity after the introduction of GO to the bilayer. It is possible that GO has extracted or reconfigured the lipid bilayer and formed a nanocomposite structure, and this is consistent with the features observed on cantilever retraction.

The average breakthrough distance (Fig. 5.10 C) is slightly higher for DOPC/GO than DOPC by itself, an observation which makes sense if we consider GO sheets to be incorporated into the lipid/bilayer surface; these sheets are mostly reported to be between 1–1.4 nm in thickness. The range of the bilayer plus GO surface height is measured here to be mostly between 1.8–9.4 nm, which suggests that addition of GO has extracted the lipid bilayer and caused the lipids to clump around the GO. The breakthrough force (Fig. 5.10 D) is slightly lower than the DOPC bilayer by itself, which is again consistent with disruption of the lipid layer. The breakthrough force for the DOPC bilayer in the presence of GO ranges from 0.3–1.5 nN, which is a wide range, indicating a highly heterogeneous surface. It also makes sense that where the bilayer has been extracted by GO, the breakthrough force is lower and where there is a nanocomposite of GO and lipid, the breakthrough force is higher (*i.e.* that bilayer fragments with GO inside have enhanced rigidity or strength).

### 5.4.5 DOPC interaction with rGO

Structurally, reduced graphene oxide (rGO) looks much closer to pristine graphene than graphene oxide. The main difference between GO and rGO is the number of oxygen-containing groups. More hydroxyl, carboxyl and ether functional groups are present on the surface of GO sheets, which can be effective in interaction with polar materials and/or dispersion in water. Highly reduced rGO is almost a superconductor and it structurally and chemically resembles graphene [39]. Given the highly different chemistry and behaviour between GO and rGO, we would anticipate them to interact differently with lipid systems.

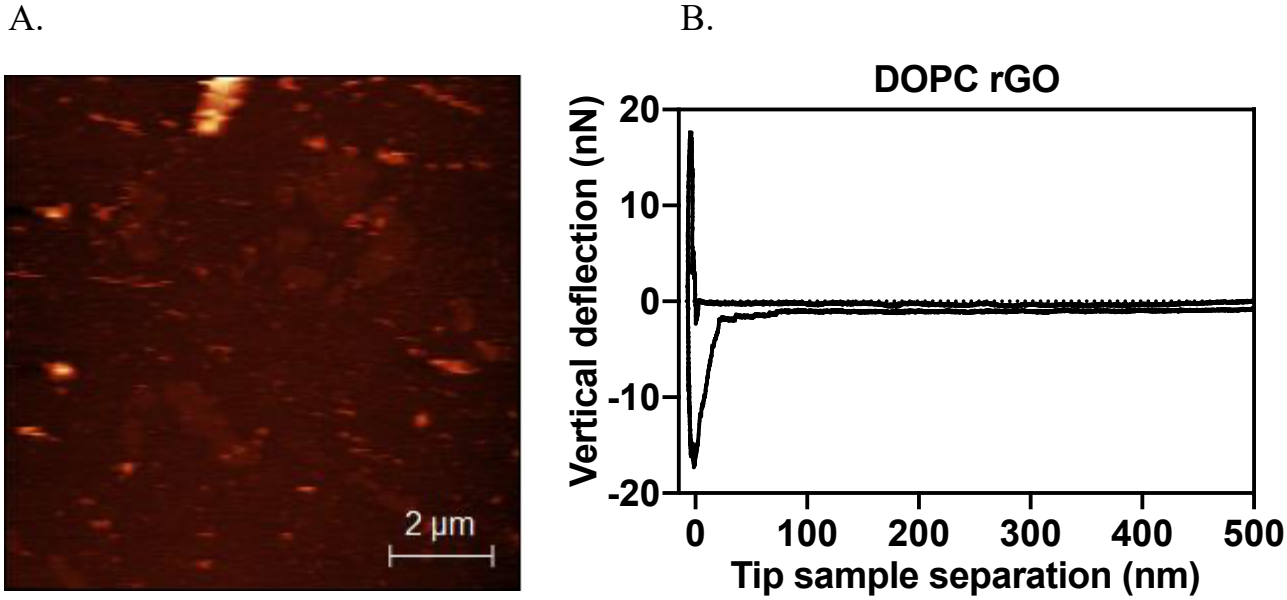


**Figure 5.11** DOPC supported lipid bilayer interaction with rGO. A) AFM image of DOPC interaction with reduced graphene oxide obtained in liquid. B) Force curve of supported lipid bilayer interaction with rGO.

AFM imaging of DOPC's interaction with rGO (Figure 5.11) shows that the lipid layer is no longer flat. As seen in Figure 12, the bilayer membrane is deformed and rGO appears to be embedded in the bilayer, again forming a nanocomposite layer. This interaction is most likely driven by the hydrophobic attraction between lipid tails (interior of the bilayer) and the

surface in rGO which is more hydrophobic than GO. Pristine graphene nanosheets can penetrate into the bilayer and affect the integrity of the membrane [40, 41]. Since rGO resembles pristine graphene sheets, at least in its basal hydrophobicity, interactions with the bilayer membrane are hypothesised to be similar.

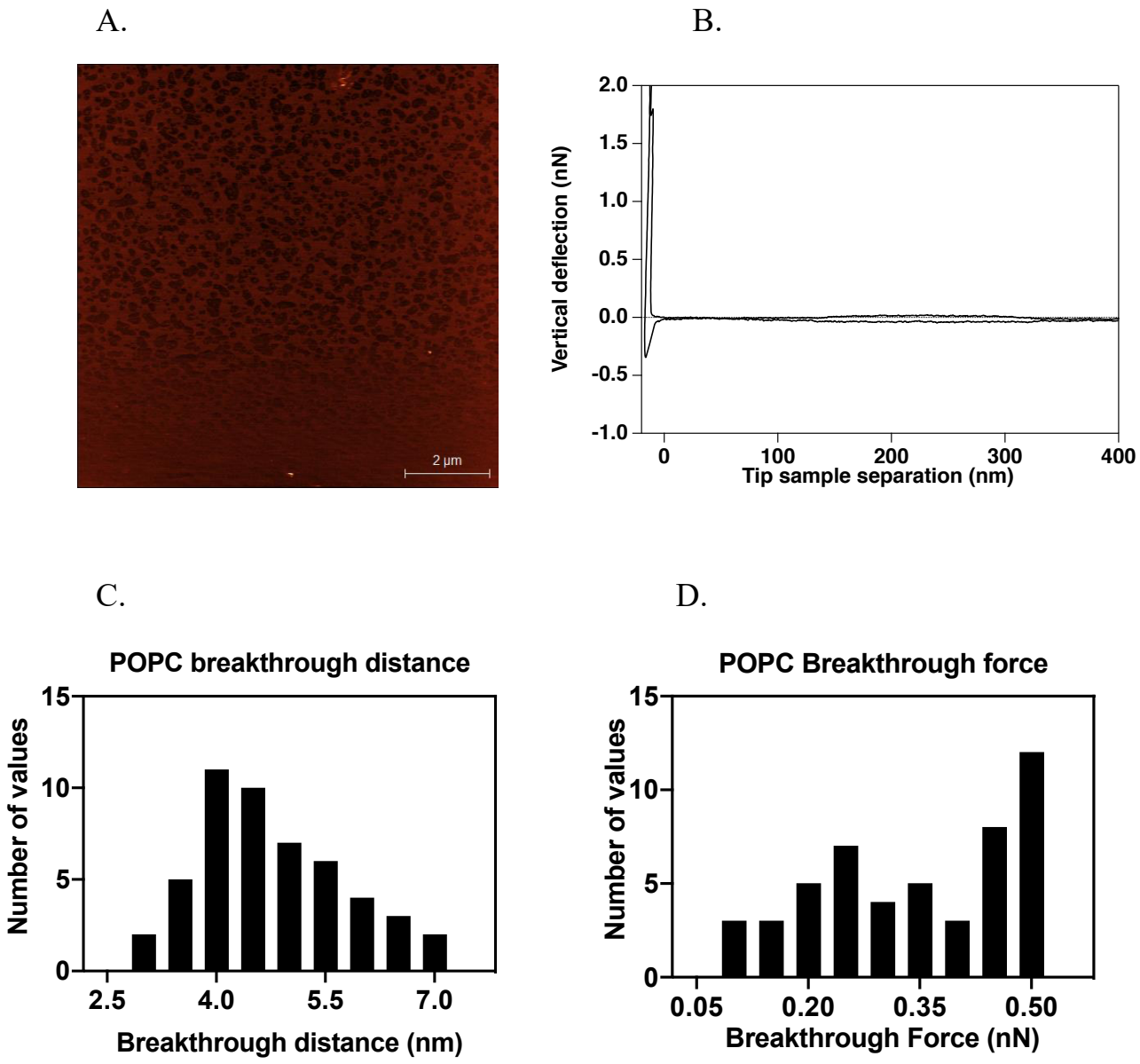


**Figure 5.12** POPC supported lipid bilayer. A) AFM image of POPC by itself. B) Force curve of POPC supported bilayer. C) POPC bilayer distance and D) breakthrough force. The data shown here is the average of 3 different experiments.

### 5.4.6 POPC lipid bilayer integrity

POPC is a commonly used phospholipid to study the interactions of nanomaterials with a supported lipid bilayer. In Fig 5.12 A, AFM imaging of a POPC lipid bilayer indicates a surface that does not look flat, and the integrity of the bilayer appears to be compromised. The surface of the bilayer looks porous, and this is likely due to dewetting of the bilayer during preparation. The measured breakthrough distance and breakthrough force is lower than that of DOPC bilayers. This can be explained as a result of the compromised integrity of the bilayer leading to lower membrane rigidity. Nonetheless, the membrane still represents a sufficiently complete layer as to worthwhile exploring in terms of its interactions with carbon nanomaterials, particularly in light of POPC's different thermal properties (*i.e.* membrane rigidity): POPC's phase transition temperature is at –2 ºC, whereas DOPC's is at –17 ºC, indicating the disorder introduced by unsaturated lipid tail groups.

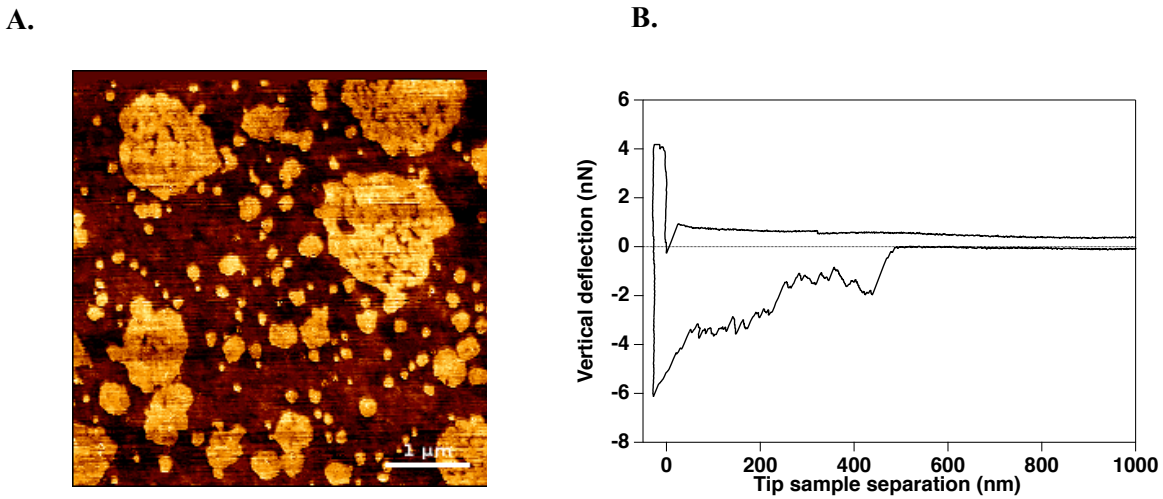


**Figure 5.13** Interactions between POPC supported lipid bilayer GO. A) AFM image showing the morphology of POPC lipid surface after interaction with GO, and B) A representative force curve indicating the interaction between POPC and GO.

### 5.4.7 POPC and GO interactions

An AFM image of a POPC bilayer after interaction with GO is shown in Figure 5.13 A. The supported lipid bilayer's integrity had been previously explored before introducing GO (Figure 5.12 A.) and although the bilayer was imperfect, significant changes are seen on addition of GO. Seen in the image is a pseudo-2D, 'clumped' structure which is presumed to be a combination of POPC and GO. Both in DOPC and POPC supported lipid bilayers, introducing GO significantly compromises the integrity of the bilayer. In this case, pore formation is very clear, and the GO has resulted in significant reconfiguration of the lipids that make up the bilayer. However, in this case it appears that GO stays on top of the bilayer rather than interleaving within the bilayer structure. A representative force curve (Figure 5.13 B) shows multiple steps when retracting but this is most likely because of the composite structure being stuck to the cantilever.

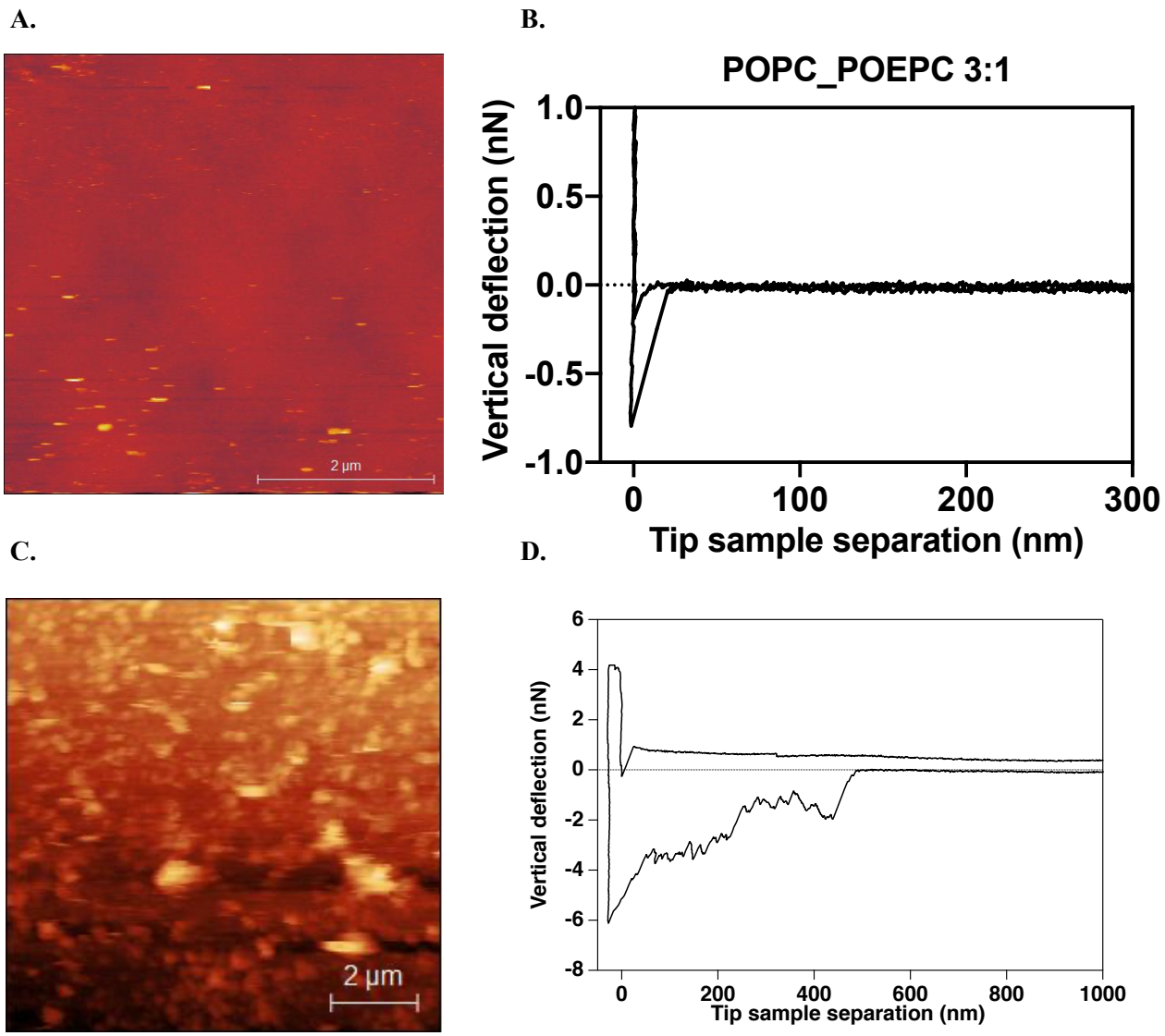


**Figure 5.14** POPC:POEPC (cationic) lipid bilayer. A) AFM image of POPC:POEPC (3:1) bilayer. B) Representative force curve of POPC:POEPC lipid bilayer. C) AFM image after interaction of POPC:POEPC lipid bilayer with GO. D) Representative force curve for POPC:POEPC lipid bilayer after interaction with GO.

### 5.4.8 Positively charged POPC/POEPC interaction with GO

Besides commonly encountered zwitterionic lipid bilayers and their interactions with GO, we also looked at charged bilayer interactions with GO. Just like the other bilayers explored, liposomes spontaneously ruptured to form a supported lipid bilayer on a mica surface. GO interactions with the positively charged lipid bilayer would be anticipated to

arise mostly due to electrostatic forces between the polar head groups of the lipids and (negatively charged) GO sheets [42]. It is notable that this sample was extremely challenging to image, likely due to significant attractive (electrostatic) forces between the lipid surface and the cantilever. Despite the lower fidelity compared to images of previous systems, GO can be seen clumped together (Figure 5.14 C) with the lipid bilayers, as seen with DOPC. Previous studies by Hu *et al.* have shown that GO can detach layers of nonpolar lipid bilayer as well as the positively charged bilayer [33], and this is likely to be what is occurring here. The GO sheets likely become coated by lipid, and it is this composite structure that represents the higher features and ‘bumps’ seen in the AFM image.

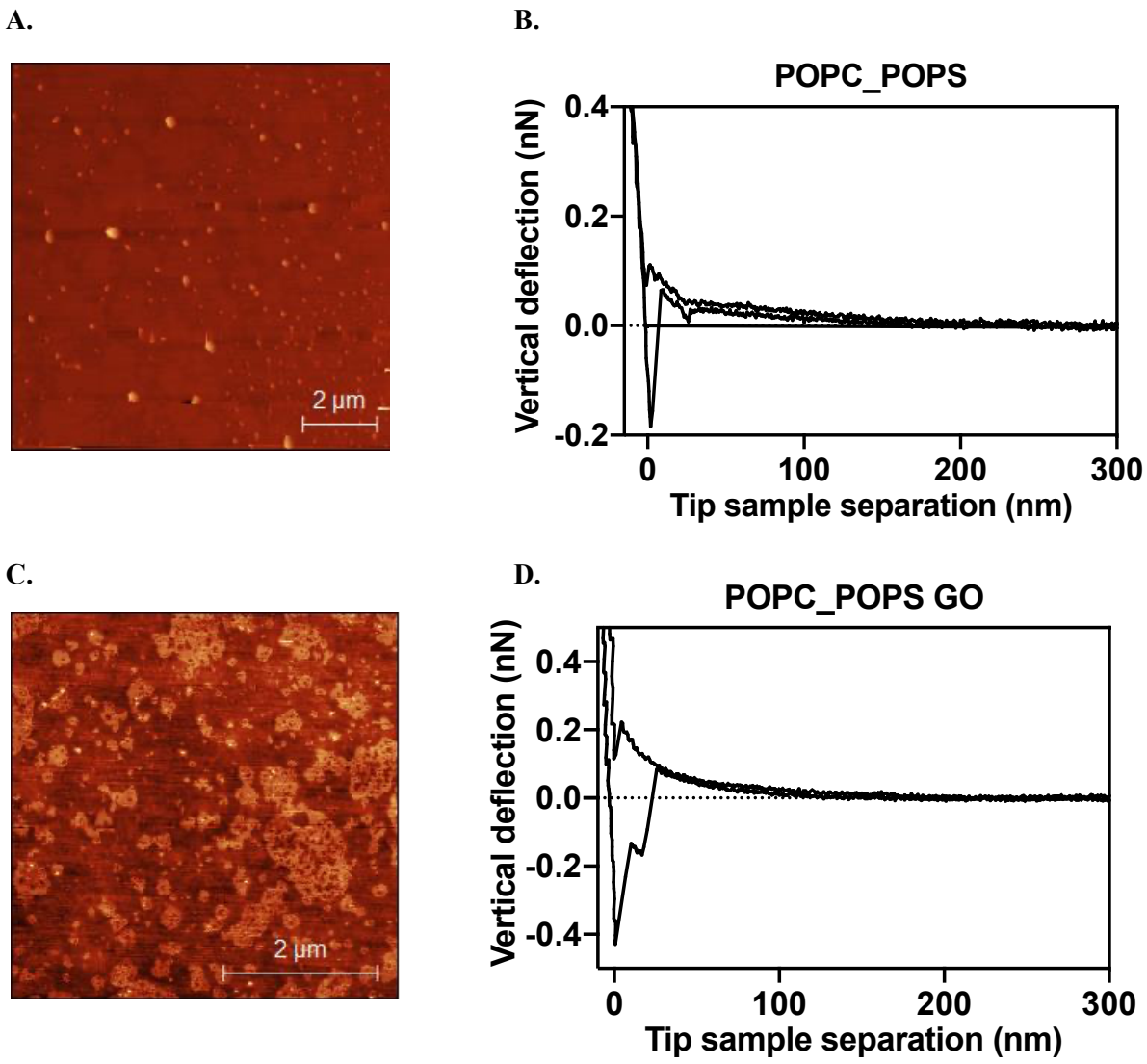


**Figure 5.15** POPC:POPS (anionic) lipid bilayer. A) AFM image of POPC:POPS bilayer. B) Representative force curve of POPC:POPSlipid bilayer. C) AFM image after interaction of POPC:POPS lipid bilayer after incubation with GO. D) Representative force curve for POPC:POPS lipid bilayer after incubation with GO.

### 5.4.9 Negatively charged POPC/POPS interactions with GO

Similarly to other lipid bilayers, negatively charged bilayers were formed by vesicle fusion, which is the spontaneous self-assembly of bilayers from vesicle rupture at a surface. In this method, vesicles adsorb to a surface, followed by rupture and then fusion to form a bilayer. Due to the electrostatic force between GO and the negatively charged bilayer, it

would be anticipated that from an electrostatic basis, GO would not bind to the bilayer. However, after addition of GO, the lipid bilayer clearly shows some defects because of the interaction.

With GO and the biomimetic membrane being negatively charged, GO interaction seems to be weak and not as disruptive as the interactions with zwitterionic biomimetic membrane. The GO interaction is mostly on the bilayer surface and in most of the cases bilayer is somewhat intact but still compromised without being ripped apart.

### 5.4.10 QCM-D study of bilayer interactions with GO

#### 5.4.10.1 Quartz crystal microbalance with dissipation (QCM-D)

Quartz crystal microbalance (QCM) is a highly sensitive instrument that is capable of measuring nanogram quantities of adsorbed materials on surfaces, by monitoring the change in resonance frequency of a quartz crystal resonator [43]. Quartz crystal microbalance with dissipation (QCM-D) in particular is a surface sensitive technique that measures mass (through frequency change) and viscoelastic properties (through energy dissipation) of thin layers such as lipid bilayers deposited on a sensor surface. QCM-D monitors change in frequency ($\Delta f$) and dissipation ($\Delta d$) of a resonating quartz chip while coated with a bilayer [44].

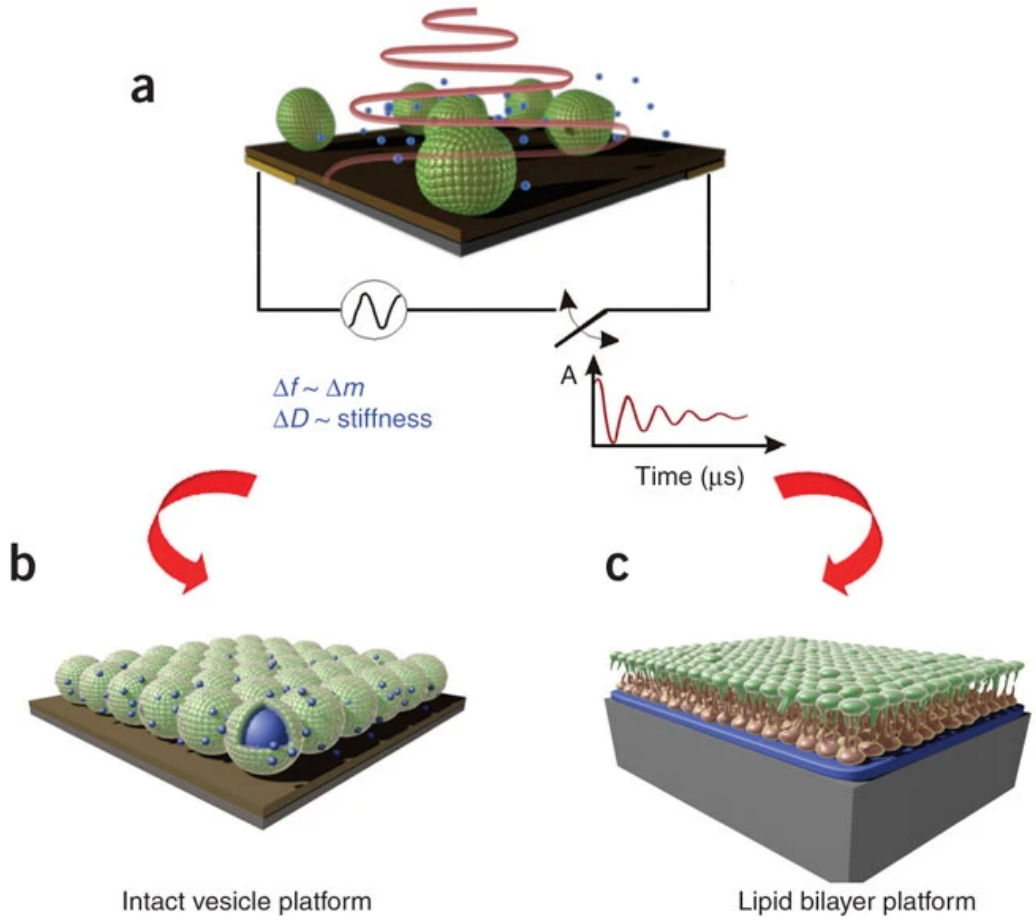


**Figure 5.16** This figure has been reproduced from Cho, *et al.* [45] A) The green spheres represent unruptured liposomes and blue balls are solvent. As liposomes are deposited on the substrate ($SiO_2$), the resonance frequency changes, and these changes are recorded as change in frequency $\Delta f$ (proportional to the adsorbed mass) and change in dissipation $\Delta D$ (loss of energy). B) Schematic indicating unruptured liposomes on $SiO_2$ surface. C) Formation of biomimetic membrane by liposome rupture and fusion.

QCM-D allows for the measurement of small mass changes on the surface of a piezoelectric crystal such as $SiO_2$ [46]. Here we use QCM-D as a complimentary technique to explore the changes to a model supported lipid bilayer on interaction with graphene oxide.

In this experiment, the sensor ($SiO_2$) is undergoing oscillation at its resonant frequency (Figure 5.17, point A) in liquid, and when liposomes are added (point B), their adsorption decreases the frequency and increases the dissipation (*i.e.* the extent to which energy is dissipated by the surface layer). At point C, water is used to wash the fused liposomes until a stable baseline is established. Based on the frequency, it seems that we

have a POPC bilayer. At point D, GO was introduced to the bilayer. If there was a strong interaction with the bilayer, then it would have severely compromised the integrity of the bilayer, and we would anticipate that this would have resulted in a very big change in dissipation and/or mass. However, in step D, the change in dissipation is very small.

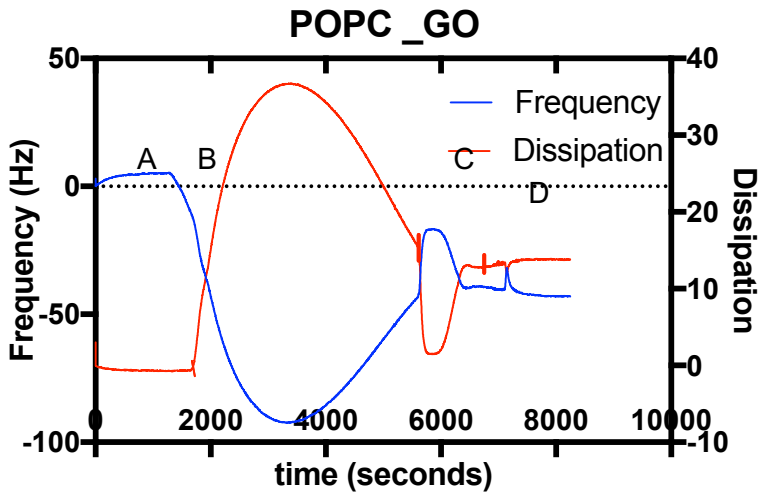


**Figure 5.17** QCM data of POPC interaction with GO. There are multiple steps (stages) in this QCM experiment, and A–D represent the different steps: A) cell with rinsed with buffer (tris); B) liposomes (0.5mg/ml) were added to the cell; C) cell was perfused with water, and D) GO (0.2mg/ml) was added. The y-axis for frequency is on the left of the graph and the Y-axis for dissipation is on the right.

When GO is introduced, there is no significant change in frequency and dissipation. Frequency is slightly higher which means GO is being adsorbed on the bilayer. The dissipation of the system is slightly higher which suggests that the integrity of the bilayer is slightly compromised but not at the level we expected. We expected graphene oxide to significantly disrupt the membrane, whereas looking at the QCM data, there was no substantial change at all. Even if GO is pulling apart the biomimetic membrane, the resulting material is still sitting on top of the crystals.

Despite initially appearing to be incongruent with the AFM data obtained, these observations can be rationalised in terms of a reconfiguration of the lipids rather than their removal. The very small change in frequency indicates that very little mass was gained or lost, which is clearly inconsistent with major portions of the lipid layer being removed entirely. However, in the AFM experiments explored in the previous sections, it appears that lipid nanocomposites with GO are redeposited on the surface, resulting in multilayered lipid fragments along with areas of exposed substrate in many cases. Thus, we hypothesise that the small changes seen with QCM when GO is added to the lipid bilayer arise because the lipids are being reconfigured, *i.e.* the smooth lipid bilayer is disrupted and redeposited as a composite with the GO, but without major loss of lipid mass.

It is notable that because the QCM analysis to obtain mass and dissipation from observed changes in frequency is based on the Sauerbrey equation ($\Delta m = -C_{QCM} \times \Delta f$)[47] and there are some assumptions that need to be made which may not be accurate for all samples or indeed at all times for a given sample:

- Mass is rigidly absorbed;
- Mass is even and homogenous on $SiO_2$;
- Mass is small relative to the mass of the crystal itself.

These assumptions are generally valid for thin, rigidly bound films, but rapidly lose accuracy for weakly bound, nonhomogeneous or viscously dissipative adsorbed materials. Its possible that even a soft lipid bilayer (or compromised bilayers) can exhibit low dissipation values in certain conditions. Due to these limitations, the collection of complementary data is important. We believe that the bilayer integrity has been compromised, and a reconfiguration of the lipid on the surface is consistent with the observation of only minor changes in mass and dissipation using QCM. However, it would be challenging to make this assertion in isolation, *i.e.* without the imaging from AFM, indicating that QCM has limitations

in the study of systems undergoing surface reconfiguration, and is most appropriate where gross mass gains or losses are experienced by the system.

## 5.5 Conclusion

Our goal for this project was to conduct a comprehensive study of GO and rGO interactions with liposome/supported lipid bilayers as a function of lipid headgroup and tailgroup chemistry, offering a panel of different charge and membrane fluidity conditions. Beyond an initial hypothesis that charge should play a role (as anticipated from other experiments of graphene oxide adsorption at interfaces), we remained scientifically agnostic to the outcome of specific experimental conditions.

AFM images in these studies clearly show that GO/rGO interacts with most of the bilayers studied, albeit to a different extent and with different ultimate morphologies as a result. AFM force curves show forces involved during breakthrough of the lipid bilayer, as well as the breakthrough distance of the bilayer. These experiments clearly indicate the integrity of the bilayer and paint a picture of robust layers that were intact before interaction with GO/rGO.

In our study, GO/rGO interacted with lipids and in all cases formed a nanocomposite like structure, where it appeared that lipids were removed from the surface and redeposited on GO sheets, or in the case of rGO, particles perhaps became interleaved in the lipid bilayers.

Images and force curves of lipid bilayers/multilayers were fairly easy to collect. However, in the presence of GO/rGO, samples seemed quite fluid and this resulted in sticking to the cantilever, providing challenging conditions for both imaging and force measurement. For this reason, we did not reuse cantilevers often, resulting in mostly one or two uses per cantilever to avoid some of these inconveniences. In most cases, retraction of

the cantilever from the lipid bilayer surface (in the presence of GO/rGO) was a multiple step event rather than the cleaner single step retraction in case of lipid bilayers only surface.

Many GO/rGO interactions with bilayers led to the formation of a nanocomposite like structure, whereas in some cases the interaction was less significant. When GO was added to zwitterionic biomimetic membranes (POPC and DOPC), the interaction seemed to be strong, and this led to compromised bilayer integrity. rGO also interacted with the bilayers similarly strongly, which led to a formation of stacked bilayers and rGO nano composites.

When GO was added to a negatively charged bilayer, interactions were much weaker and did not result in ripping apart of the bilayer. Instead, GO settled on top of the bilayer and tended to form defects in the bilayer, but not to the same extent as for the zwitterionic biomimetic membrane. Both GO and the anionic lipid are negatively charged, and they tend to repel each other, explaining this weaker interaction. In contrast, GO interacts strongly with positively charged lipids and forms a complex mixture of GO and lipids fragments.

When comparing interactions seen for GO with those of rGO, it is evident that GO is more polar than rGO, and this maybe the reason why it can interact with different lipids more strongly. rGO is less polar because of its fewer oxygen containing groups compared to GO. This may be the reason that rGO generally shows weaker interactions and less disruption of lipid bilayers. In the case of negatively and positively charged lipids interacting with rGO, it seemed that significant quantities of rGO remained dispersed in solution and AFM cantilevers picked it up fairly quickly, making it very challenging to image and record force spectroscopy data.

In this chapter and the next, we present data that further supports the interaction of GO/rGO with biomimetic cell membrane and liposomes. Depending on lipid charges, tail length and different head group chemistries of the biomimetic membranes studied, GO and

rGO interact very differently, indicating a significant role of surface forces and surface chemistry in modulating these interactions.

## 5.6 References


1. Maiti, D., *et al.*, Carbon-Based Nanomaterials for Biomedical Applications: A Recent Study. Front Pharmacol, 2018. **9**: p. 1401.
2. Mohajeri, M., B. Behnam, and A. Sahebkar, Biomedical applications of carbon nanomaterials: Drug and gene delivery potentials. J Cell Physiol, 2018. **234**(1): p. 298-319.
3. Dasari Shareena, T.P., *et al.*, A Review on Graphene-Based Nanomaterials in Biomedical Applications and Risks in Environment and Health. Nanomicro Lett, 2018. **10**(3).
4. Saptarshi, S.R., A. Duschl, and A.L. Lopata, Interaction of nanoparticles with proteins: relation to bio-reactivity of the nanoparticle. J Nanobiotechnology, 2013. **11**: p. 26.
5. Zeinabad, H.A., *et al.*, Interaction of single and multi wall carbon nanotubes with the biological systems: tau protein and PC12 cells as targets. Sci Rep, 2016. **6**: p. 26508.
6. Dreyer, D.R., *et al.*, The chemistry of graphene oxide. Chem Soc Rev, 2010. **39**(1): p. 228-40.
7. Sreeprasad, T.S. and V. Berry, How do the electrical properties of graphene change with its functionalization? Small, 2013. **9**(3): p. 341-50.
8. Dimiev, A.M. and J.M. Tour, Mechanism of graphene oxide formation. ACS Nano, 2014. **8**(3): p. 3060-8.
9. Liu, Z., *et al.*, PEGylated nanographene oxide for delivery of water-insoluble cancer drugs. J Am Chem Soc, 2008. **130**(33): p. 10876-7.
10. Morales-Narvaez, E. and A. Merkoci, Graphene oxide as an optical biosensing platform. Adv Mater, 2012. **24**(25): p. 3298-308.
11. Nguyen, P. and V. Berry, Graphene Interfaced with Biological Cells: Opportunities and Challenges. J Phys Chem Lett, 2012. **3**(8): p. 1024-9.
12. Sun, X., *et al.*, Nano-Graphene Oxide for Cellular Imaging and Drug Delivery. Nano Res, 2008. **1**(3): p. 203-212.
13. Zhang, L.L., *et al.*, Layered graphene oxide nanostructures with sandwiched conducting polymers as supercapacitor electrodes. Langmuir, 2010. **26**(22): p. 17624-8.
14. Liu, J., L. Cui, and D. Losic, Graphene and graphene oxide as new nanocarriers for drug delivery applications. Acta Biomater, 2013. **9**(12): p. 9243-57.
15. Daniyal, M., B. Liu, and W. Wang, Comprehensive Review On Graphene Oxide For Use In Drug Delivery System. Curr Med Chem, 2019.
16. Muthoosamy, K., R.G. Bai, and S. Manickam, Graphene and graphene oxide as a docking station for modern drug delivery system. Curr Drug Deliv, 2014. **11**(6): p. 701-18.
17. Bosch-Navarro, C., *et al.*, Influence of the pH on the synthesis of reduced graphene oxide under hydrothermal conditions. Nanoscale, 2012. **4**(13): p. 3977-82.
18. Mason, A.J., A. Marquette, and B. Bechinger, Zwitterionic phospholipids and sterols modulate antimicrobial peptide-induced membrane destabilization. Biophys J, 2007. **93**(12): p. 4289-99.
19. Mingeot-Leclercq, M.P., *et al.*, Atomic force microscopy of supported lipid bilayers. Nat Protoc, 2008. **3**(10): p. 1654-9.
20. Attwood, S.J., Y. Choi, and Z. Leonenko, Preparation of DOPC and DPPC Supported Planar Lipid Bilayers for Atomic Force Microscopy and Atomic Force Spectroscopy. Int J Mol Sci, 2013. **14**(2): p. 3514-39.
21. Dufrene, Y.F., *et al.*, Imaging modes of atomic force microscopy for application in molecular and cell biology. Nat Nanotechnol, 2017. **12**(4): p. 295-307.

22. Hoh, J.H. and C.A. Schoenenberger, Surface morphology and mechanical properties of MDCK monolayers by atomic force microscopy. J Cell Sci, 1994. **107 ( Pt 5)**: p. 1105-14.
23. Lee, C.K., *et al.*, Atomic force microscopy: determination of unbinding force, off rate and energy barrier for protein-ligand interaction. Micron, 2007. **38**(5): p. 446-61.
24. Geibel, J., Modern advances in microscopy: from animal to atom. Braz J Med Biol Res, 1993. **26**(11): p. 1133-9.
25. Yang, J. and Z. Shao, Recent advances in biological atomic force microscopy. Micron, 1995. **26**(1): p. 35-49.
26. Vahabi, S., B. Nazemi Salman, and A. Javanmard, Atomic force microscopy application in biological research: a review study. Iran J Med Sci, 2013. **38**(2): p. 76-83.
27. Dufrene, Y.F., Recent progress in the application of atomic force microscopy imaging and force spectroscopy to microbiology. Curr Opin Microbiol, 2003. **6**(3): p. 317-23.
28. Dufrene, Y.F. and G.U. Lee, Advances in the characterization of supported lipid films with the atomic force microscope. Biochim Biophys Acta, 2000. **1509**(1-2): p. 14-41.
29. Alonso, J.L. and W.H. Goldmann, Feeling the forces: atomic force microscopy in cell biology. Life Sci, 2003. **72**(23): p. 2553-60.
30. Surrey, T. and F. Jahnig, Refolding and oriented insertion of a membrane protein into a lipid bilayer. Proc Natl Acad Sci U S A, 1992. **89**(16): p. 7457-61.
31. Akhavan, O. and E. Ghaderi, Toxicity of graphene and graphene oxide nanowalls against bacteria. ACS Nano, 2010. **4**(10): p. 5731-6.
32. Hu, W., *et al.*, Graphene-based antibacterial paper. ACS Nano, 2010. **4**(7): p. 4317-23.
33. Hu, X., *et al.*, Strong hydrophobic interaction between graphene oxide and supported lipid bilayers revealed by AFM. Microsc Res Tech, 2016. **79**(8): p. 721-6.
34. Richter, R.P., R. Berat, and A.R. Brisson, Formation of solid-supported lipid bilayers: an integrated view. Langmuir, 2006. **22**(8): p. 3497-505.
35. Frost, R., *et al.*, Graphene oxide and lipid membranes: interactions and nanocomposite structures. Nano Lett, 2012. **12**(7): p. 3356-62.
36. Dols-Perez, A., *et al.*, Ultrathin spin-coated dioleoylphosphatidylcholine lipid layers in dry conditions: a combined atomic force microscopy and nanomechanical study. Langmuir, 2011. **27**(21): p. 13165-72.
37. Dekkiche, F., *et al.*, Stability and tribological performances of fluid phospholipid bilayers: effect of buffer and ions. Colloids Surf B Biointerfaces, 2010. **80**(2): p. 232-9.
38. Leonenko, Z.V., *et al.*, Investigation of temperature-induced phase transitions in DOPC and DPPC phospholipid bilayers using temperature-controlled scanning force microscopy. Biophys J, 2004. **86**(6): p. 3783-93.
39. Rodriguez-Perez, L., M.A. Herranz, and N. Martin, The chemistry of pristine graphene. Chem Commun (Camb), 2013. **49**(36): p. 3721-35.
40. Tu, Y., *et al.*, Destructive extraction of phospholipids from Escherichia coli membranes by graphene nanosheets. Nat Nanotechnol, 2013. **8**(8): p. 594-601.
41. Santiago, R. and R. Reigada, Interaction modes between nanosized graphene flakes and liposomes: Adsorption, insertion and membrane fusion. Biochim Biophys Acta Gen Subj, 2019. **1863**(4): p. 723-731.
42. Accardo, A., *et al.*, Probing droplets on superhydrophobic surfaces by synchrotron radiation scattering techniques. J Synchrotron Radiat, 2014. **21**(Pt 4): p. 643-53.

43. Castano, S., B. Desbat, and J. Dufourcq, Ideally amphipathic beta-sheeted peptides at interfaces: structure, orientation, affinities for lipids and hemolytic activity of (KL)(m)K peptides. Biochim Biophys Acta, 2000. **1463**(1): p. 65-80.
44. Rodahl, M., F. Hook, and B. Kasemo, QCM Operation in Liquids: An Explanation of Measured Variations in Frequency and Q Factor with Liquid Conductivity. Anal Chem, 1996. **68**(13): p. 2219-27.
45. Cho, N.J., *et al.*, Quartz crystal microbalance with dissipation monitoring of supported lipid bilayers on various substrates. Nat Protoc, 2010. **5**(6): p. 1096-106.
46. Johannsmann, D., Viscoelastic, mechanical, and dielectric measurements on complex samples with the quartz crystal microbalance. Phys Chem Chem Phys, 2008. **10**(31): p. 4516-34.
47. Huang, X., *et al.*, A Practical Model of Quartz Crystal Microbalance in Actual Applications. Sensors (Basel), 2017. **17**(8).

# Chapter 6. Graphene oxide and reduced graphene oxide interaction with liposomes – a stopped-flow SANS experiment

## 6.1 Introduction

In the previous chapter we studied the interactions of GO (and rGO) with supported lipid bilayers. These supported lipid bilayers were used to mimic cell membrane, which serves as the functional boundary between the cell and its exterior [1]. The major component of a cell membrane is a lipid bilayer, comprising molecules with both hydrophobic and hydrophilic regions, facilitating self-assembly and allowing selective transmission of a diverse range of molecules. Glycerophospholipids are abundantly found in cell membranes, and these lipids specifically have a hydrophilic head group and two hydrophobic tails. Lipids can be zwitterionic, positive or negatively charged [2]. Under physiological conditions, phosphatidylcholines are zwitterionic lipids, while phosphatidylglycerols carry a net charge. Based on these charges, we anticipate that such lipids could interact with carbon nanomaterials such as graphene oxide (GO) and reduced graphene oxide (rGO) differently. To add to the complexity of this interaction, acyl-chains vary in length and can be saturated or unsaturated. In the previous chapter we looked at nanomaterials (GO and rGO) and their interaction with lipid bilayers (zwitterionic, negatively and positively charged). In this chapter, our aim is to look at liposome interactions with GO (and rGO) using small-angne neutron scattering SANS.

Graphene based nanomaterials have been a subject of intense research since their isolation (in the case of graphene itself by Novoselov *et al.* in 2004) [3]. Graphene exhibits exceptional physiochemical properties such as high fracture toughness, thermal conductivity, Young's modulus and electrical conductivity [4, 5]. Graphene nanosheets have been adapted for a variety of application including in biomedicine, energy storage, nano-devices, renewable energy and sensing applications [6, 7].

Compared to hydrophobic graphene, the high surface area and the amphiphilicity of GO makes it an ideal substrate for biosensors, environmental and biomedical applications. Recent work has shown that carbon based fluorescent materials show greater stability, biocompatibility and lower toxicity than their inorganic counterparts [8, 9]. If these materials were to be used in our day to day lives, their interaction with live cells and membranes needs to be better understood. We aim to study the interaction of prototypical carbon nanomaterials with biomimetic lipid membranes extensively, in order to better understand the affects that such materials will have on living cells and the broader environment.

With the increasingly widespread use of nanoparticles in our daily lives and in the environment, understanding their interaction with the cell membrane is of the utmost importance, whether it is to be able to assess their risks (toxicity) or their benefits in nanomedicine. For this reason, it is necessary to understand both equilibrium and dynamic interactions of nanoparticles with cell membranes, along with structural and transport features. Proteins, polymers and nanoparticles are known to interact with lipid bilayers or lipid vesicles in various ways, intercalating into the membrane, hosting into vesicles or causing vesicle rupture. Fundamental understanding of these interactions is therefore critically important to identifying the drug and gene delivery capabilities of composite systems.

In recent years, several different groups have studied the interactions of graphene based nanomaterials with liposomes, biomimetic membranes and sometimes even entire (live) bacterial cells. In 2013 and 2014, several studies suggested that graphene based nanomaterials can be cytotoxic to cell membranes, can penetrate the membrane and extract phospholipids [10-12]. We aim to study the interaction of graphene based nanomaterials with zwitterionic and negatively charged liposomes that are typical of mammalian cell membranes. Several recent studies suggest that positively charged lipids have higher

affinity with GO compared to the negatively charged lipids [2, 13, 14]. GO sheets induced rupture of the liposomes which initiated the formation of bilayer and potentially lipid–graphene composite layers [2]. Previous studies using quart crystal microbalance with dissipation monitoring have shown that GO induces the rupture of liposomes and results in the formation of surface bilayers [15].

**Aim:** In this work we hope to gain a more complete understanding of the interactions of GO and rGO with lipid membranes using holistic scattering measurements. The interactions between liposomes and nanoparticles are of particular interest, as liposomes can serve as a model system for biological cells. Liposome integrity will be explored in the presence of both GO and rGO, and charges in the size and structure of liposomes (zwitterionic and anionic with different carbon chain length) will be varied to better understand the interactions responsible for structural changes. We wish to determine the average radius, polydispersity, and the thickness of the hydrophobic and hydrophilic parts of the bilayer before and after the addition of GO and rGO, along with the overall liposome integrity, to understand the extent of change brought about by carbon nanomaterial addition.

## 6.2 Methods

### 6.2.1 Small-angle neutron scattering (SANS)

Over the years, neutron scattering has evolved to meet growing scientific need. Neutrons were first discovered in 1932 by Chadwick [16] and four years later two other groups discovered that neutrons can be used for diffraction [17, 18]. However, SANS was developed approximately 30 years later in the 1960s. Sturhmann et al were one of the first pioneers to demonstrate neutrons were a powerful tool to investigate materials based on

the variation of scattering length densities within a sample [19]. Neutrons lack any charge and this is what allows them to penetrate deeply into bulk matter. Due to their amenable wavelength range on the order of a few Ångstroms, SANS is ideally suited to the study of microstructures such as nanoparticles, micelles, proteins and many other soft and self-assembled systems [20]. Neutrons interact with nuclei via a very short-range nuclear force which means that they can penetrate more deeply than either x-rays of electrons. The benefits of neutron scattering are:

- Neutron probes are non-destructive even for biological samples due to low levels of energy transfer. However, high energy x-rays can damage samples.
- Neutrons can penetrate to greater depth and can be used to study thick samples which may or may not be studied using x-rays.
- Detailed structural information can be obtained using selective isotopic labelling to vary neutron scattering length density.

However, compared to synchrotron x-ray measurements, neutron scattering requires long data collection to achieve good signal to noise ratio.

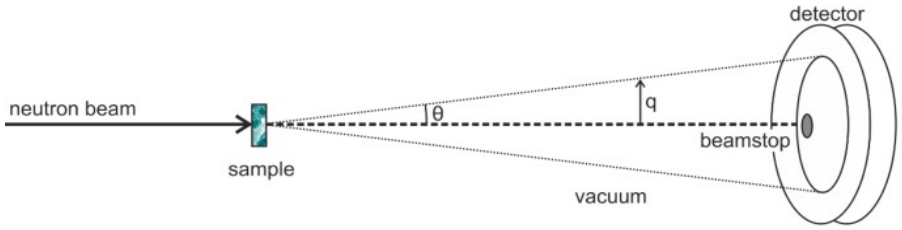


**Figure 6.1** Schematic representation of a SANS setup

Structural details are obtained by measuring the intensity of scattered neutrons through a small angle between 0.2 to 2 degrees. Neutrons are useful for analysing nanoparticles, micelles and liposomes because their wavelength, $\lambda$ is usually smaller than the materials of interest [21]. This allows the nuclei to act as point scatter, which produces interference at a (distant) detector. This is explained by the Bragg equation:

$$\lambda = 2d \sin\theta \qquad \text{Eq. 1}$$

where $\theta$ is the neutron scattering angle and $d$ is the distance between point scatterers. For convenience, the scattering vector $\vec{Q}$ is used to account for the wavelength of the incident neutron beam with the following equation:

$$|\vec{Q}| = \frac{4\pi}{\lambda} \sin\left(\frac{\theta}{2}\right) \qquad \text{Eq. 2}$$

where $|\vec{Q}|$ is the magnitude of scattering vector (typically in $Å^{-1}$), $\theta$ is again the scattering angle and $\lambda$ is the neutron wavelength (in Å) [20, 22]. Scattered neutrons are measured as a function of $|\vec{Q}|$ (henceforth abbreviated for simplicity as $q$) and are combined to provide overall intensity. Low $q$ values indicate scattering correlations that correspond to larger features and scattering at high $q$ values suggests correlations from small structures.

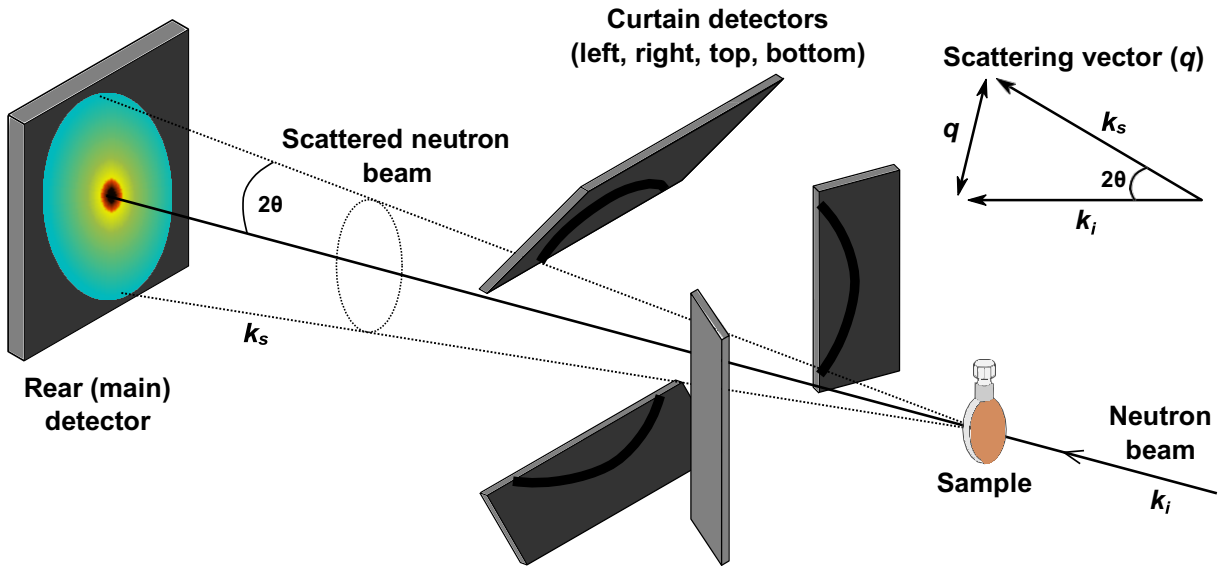


**Figure 6.2** This figure has been reproduced from [23]. Incident neutron vector $\vec{k}_i$ and the scattered neutron vector $\vec{k}_s$ and the scattering vector $\vec{q}$ is given as $\vec{q} = \vec{k}_s - \vec{k}_i$. The schematic representation of SANS shows 4 different curtain detectors[23]. The scattering vector depiction is shown in the top right corner of this Figure.

Stopped flow (dynamic and static) small-angle neutron scattering (SANS) measurements were obtained on the Bilby beamline [32, 33] in time-of-flight mode with an asymmetric detector array at the Australian Centre for Neutron Scattering (ACNS), ANSTO, Lucas Heights, NSW. A neutron wavelength of 6 Å was used in these measurements, obtaining a q-range of 0.003-0.47 Å. Samples were prepared as separate liposome and graphene oxide/reduced graphene oxide dispersions, and mixed using a stopped flow apparatus (BioLogic SFM-300 stopped flow mixing cell) whilst in the neutron beam. Contrast was introduced by using $D_2O$ as the solvent. Raw scattering counts were normalised against a blocked beam and a transmission measurement, then were reduced to average absolute intensity profiles as a function of the momentum transfer or scattering vector, q. Raw 1D data thus obtained were normalised and corrected against a solvent background comprising the measurement cell containing $D_2O$.

Lipids used in this study were stored at –20 °C until use. All samples were prepared in $D_2O$ and the initial concentration was 5 mg/mL. These samples were subsequently diluted to obtain desired concentration using the stopped flow setup. Lipid suspensions were extruded ~ 20 times through a 100 nm membrane in an attempt to obtain a comparatively small and monodisperse liposome dispersion. The extrusion of the lipid suspensions resulted in ~ 100 nm vesicles.

### 6.2.2 Modelling SANS data

Scattering data from liposomes and resulting lipid–GO/rGO composites were fit using either (or both) of two models. The first (multi-lamellar vesicles) best represents liposomes themselves, and is a slight adjustment of the core–shell sphere model developed by Guinier [24]. The model assumes that a central core of solvent is surrounded by N shells of thickness $t_s$, that separated by ‘shells’ of solvent (water) of thickness $t_w$.

In 1D form, the master expression for this type of scattering model is:

$$P(q) = scale.\frac{\Phi}{V(R_N)}F^2(q) + background \quad \text{Eq. 3}$$

where scale is an instrument-dependant scale factor (here set always to 1), Φ is the vesicle (liposome) volume fraction, V is the volume of a vesicle of radius r (see below), and the particle form factor, F is given by:

$$F(q) = (\rho_{shell} - \rho_{solvent}) \sum_{i=1}^{N} \left[ 3V(r_i) \frac{sin(qr_i) - qr_i cos(qr_i)}{(qr_i)^3} - 3V(R_i) \frac{sin(qR_i) - qR_i cos(qR_i)}{(qR_i)^3} \right] \quad \text{Eq. 4}$$

where $\rho_{shell}$ and $\rho_{solvent}$ are the neutron scattering length densities of the shell material and solvent respectively, $r_i$ is the inner radius of the $i^{th}$ shell, and $R_i$ is the outer radius of the $i^{th}$ shell, such that $r_i = r_c + (i–1)(t_s–t_w)$ and $R_i = r_i + t_s$.

It is evident from the summation over N shells that this model can account for polydispersity in shell number (*i.e.* unilamellar vesicles, plus contributions from bilamellar, trilamellar, *etc.*). In the way that this model is implemented in the SASView software environment that we use for fitting SANS data, this can be accomplished using a Shultz-type polydispersity factor for N (computationally simple but conceptually more challenging) or providing a direct matrix of shell proportional contributions (e.g. 95% unilamellar, 3% bilamellar, 2% trilamellar). Here we use the former approach for simplicity, with the acknowledgement that it is a simplification of the more robust (but much slower) second approach. This can result in apparent N values that are below 1 (which at first glance appears unphysical), but actually makes the closest correspondence to a distribution of the type described above that is typical of our starting liposome dispersions (around 93% unilamellar and 7% bilamellar).

For composite structures produced by lipids with GO, a ‘broad peak’ model was used to fit data. This simple model assumes two features: a Lorentzian-type peak describing correlations between scatterers at some preferred separation (where peak position defines

the correlation length, peak height indicates the length-scale over which this order persists, and peak width indicates the polydispersity within this correlation length) and a Porod region with a characteristic slope which gives information at larger length-scales on scattering from the surface of objects. The scattering is described by the master equation:

$$I(q) = \frac{A}{q^n} + \frac{C}{1 + (|q - q_0|\xi)^m} + B \qquad \text{Eq. 5}$$

where $A$ is the Porod scale factor, $n$ is the Porod exponent, $C$ is the Lorentzian scale parameter, $q_0$ is the position of the correlation peak, $m$ is the index for a generalised Lorentzian, ξ is the screening (persistence) length and $B$ is a flat (constant) background contribution. The peak position, $q_0$ can be converted into a correlation 'd-spacing' ($d$) using the relationship: $d = 2\pi/q_0$. In our work, we anticipate that the peak seen arises from the repeat spacing of lipid lamellar 'stacks', and indeed the typical spacings encountered are consistent with similar observations of lipid phases from the literature.

### 6.3 Results and Discussion

When liposomes are prepared in $D_2O$, good contrast can be obtained for the hydrophobic tail. Neutrons therefore experience strong contrast between the continuous solvent and the lipid tail, but the headgroups are highly solvated and comparatively weakly scattering. Graphene oxide and reduced graphene oxide are extremely weakly scattering for neutrons at the concentrations used, and therefore their contribution to the overall scattered intensity is minimal, and changes seen in scattering patterns arise from reconfiguration of the lipids themselves. Therefore, in the following exploration of obtained results, we assume that the system consists of 'slabs' of lipid tails in $D_2O$, and this description is consistent with much of the neutron literature concerning lipid systems [25, 26].

### 6.3.1 Zwitterionic liposome interaction with GO

#### 6.3.1.1 DOPC interaction with GO

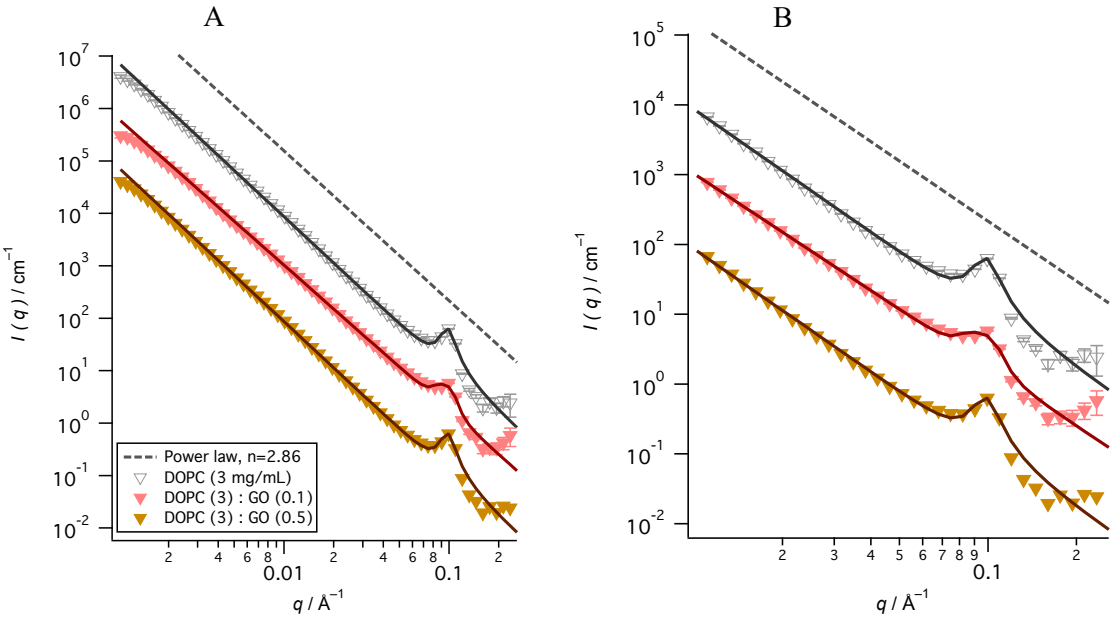


**Figure 6.3** Small angle neutron scattering data from DOPC vesicles, and their interaction with different concentrations of graphene oxide (GO). A) SANS data of DOPC with GO: data presented here are DOPC (3 mg/mL) by itself, DOPC with GO (3:0.1 mg/mL ratio) and DOPC with GO (3:0.5 mg/mL ratio).). B) 'zoomed in' (reduced q-range) plot highlighting the Porod region (mid-high q) of DOPC SANS and model fits. All solid lines represent the best fit using a 'broad peak' model as discussed in the text. 3 different experiments were performed.

DOPC is a phosphatidylcholine phospholipid that is zwitterionic at physiological pH and has a transition temperature ($T_c$) of –22° C. DOPC has a headgroup comprising choline, phosphate and glycerol that is attached to two hydrophobic fatty acids tail that are fully saturated. As such, DOPC is highly hydrophobic and self-assembles strongly and readily in water. DOPC is one of the most commonly studied phospholipids for exploring liposome/bilayer interactions with nanomaterials and proteins.

There are many different liposome formulation methods, each of which produces different sizes of vesicles. Liposomes can be prepared using freeze thaw cycling or by

hydrating a thin film of lipids [27-29]. However, these methods tend to produce multilamellar vesicles that are fairly large in terms of their size and they are generally polydisperse [28]. Extruded liposomes are mostly monodisperse and their size is based on the membrane used. For example we used a membrane with 100 nm pore size, and most of the vesicles produced were around 100–110 nm in diameter. Phospholipids including DOPC form predominantly unilamellar vesicles when hydrated and extruded using a 100 nm membrane. At room temperature, DOPC is above its $T_c$ and therefore in its liquid crystalline phase.

SANS data in Figure 6A show scattering from DOPC (3 mg/mL) by itself, and DOPC with GO (3:1 and 3:0.5 mg/mL respectively). DOPC 'vesicles' prepared using extrusion exhibit a distinctive Bragg peak around q = 0.1 Å as shown in Figure 6.3, which corresponds to a repeat spacing of around 63 Å, consistent with the stacking of DOPC layers in condensed multilayer systems [23]. It is significant to note that DOPC at this concentration lacks the characteristic turnover at low q that would indicate the spherical form factor of liposomes, and these data were therefore fitted using the simple 'broad peak' (Lorentzian + Porod) model. The scattering gradient in the medium-q region suggests that the surface of the structure is somewhat textured or tortuous ($q^{-x}$, where $2<x<3$, where 2 would represent scattering from flat, planar bilayers). The distinct peak in the Porod (high q) region relates to a repeated feature within the structure as shown in Figure 6.3.A and 6.3.B. This peak is usually a representation of multilamellar vesicles that show stacks of lipid lamellae. Similar peaks have been seen in unextruded DPPC samples [25]. This is quite unexpected; the peak suggests that this sample does not contain a particularly well-structured lipid morphology, and most likely comprises a mix of lipid multilayer fragments or very polydisperse liposomes that are clustered together.

The slight rounding at lowest q may indicate that only a few intact liposomes are present in the samples, or that they are very polydisperse and weakly structured. We

previously explored the behaviour of DOPC in AFM studies as well as protein interactions with this membrane lipid (previous chapters), and we were able to prepare polydisperse DOPC liposomes. This leads us to conclude that this was a one-off experimental error, likely arising from temperature changes during lipid handling; due to the very specific instrumentation, materials and setup required, I have not been able to repeat this experiment.

It is worthwhile to note however, that despite the weakly structured nature of DOPC by itself, mixing this lipid system with graphene oxide results in almost no change to the structure. There is very little evidence of a change in the shape or position of the Bragg peak at high-q, indicating that lipid stacking is broadly unaffected by mixing with GO. This would make sense when compared to the stark reconfigurations seen in AFM imaging of smooth DOPC bilayers, where stacking into lipid–GO nanocomposite structures was seen. In the present experiment, the lipid already appears to be present as multilayer fragments, and so further disruption of these structures by GO would likely not be seen at the short length-scales probed by this SANS measurement.

**Table 6.1** Fitted SANS parameters for interaction of GO with lipids where a 'broad peak' (Lorentzian plus Porod exponent) was used to fit scattering data.

| Lipid | Lipid conc. | GO conc. | Peak posit. | Corr. length | Porod exponent |
|---|---|---|---|---|---|
| | mg/mL | mg/mL | $Å^{-1}$ | Å | |
| DOPC | 5 | 0.5 | 0.0904 | 49.3 | 2.72 |
| DOPC | 3 | 0.5 | 0.091 | 50.5 | 2.75 |
| DOPC | 3 | 0.1 | 0.094 | 63.4 | 2.78 |
| POPC | 2 | 1 | 0.096 | 42.7 | 2.89 |
| POPC | 1 | 1 | 0.107 | 35.6 | 3.05 |
| DPPC | 2 | 1 | 0.0886 | 70.12 | 2.8 |
| DPPC | 5 | 1 | 0.0865 | 75.04 | 2.84 |
| POPC:POPS | 2 | 1 | 0.1061 | 49.236 | 3.47 |
| POPC:POPS | 5 | 0.5 | 0.0942 | 40.93 | 2.83 |

**Table 6.2** Fitted SANS parameters for interaction of GO with lipids where a multilamellar vesicle was used to fit scattering data.

| Lipid | Lipid conc. | GO conc. | Volume fraction | Radius (PD) | Shell thickness | Solvent thickness | $N_{shells}$ (PD) |
|---|---|---|---|---|---|---|---|
| | mg/mL | mg/mL | | Å | Å | Å | |
| DPPC | 5 | 0 | 0.020 | 450 (0.3) | 40 | 19 | 1.05 (0.3) |
| POPC | 10 | 0 | 0.037 | 460 (0.24) | 38 | 17 | 0.9 (0.39) |
| POPC | 5 | 0 | 0.019 | 460 (0.24) | 38 | 17 | 0.9 (0.39) |
| POPC | 5 | 0.5 | 0.021 | 460 (0.24) | 37 | 17 | 0.9 (0.39) |
| POPC:POPS | 5 | 0 | 0.029 | 460 (0.24) | 37 | 19 | 0.95 (0.3) |
| POPC:POPS | 5 | 0.1 | 0.029 | 470 (0.24) | 36 | 19 | 0.95 (0.36) |

Data presented above show scattering from equilibrium samples after mixing of lipid with GO (taken over the course of the 30 minutes following mixing). It is worth noting that due to the way data is collected on the Bilby SANS instrument, it is possible to 'bin' this data into time-slices of any duration, to explore any kinetic effects (*i.e.* transitional states or geometries) that occurred in the seconds to minutes after mixing. For none of the samples in this study did we notice any transitional structures, even when interrogating 1–5 seconds of scattering collected directly after mixing. This indicates that equilibrium is reached exceedingly quickly (in sub-second times) in the mixing conditions employed here. Stopped flow is known for extremely rapid, thorough and turbulent mixing, and so this is perhaps not surprising. However, as no kinetic effects were noted, we restrict the remainder of our discussion to equilibrium scattering patterns and geometries fitted to these equilibrium data.

#### 6.3.1.2 DPPC interaction with GO

DPPC is a zwitterionic phospholipid which consists of 2 saturated 16-carbon fatty acid chains connected by a glycerol backbone with a headgroup. Its phase transition temperature is at 41ºC, implying that its bilayers are much more crystalline than DOPC at room temperature. Scattering from pure DPPC liposomes is shown in Figure 6.4. The low q region (Guinier region) in the scattering data here provides information on the overall shape and size of structures present in the sample, whereas high q region typically contains information on bilayer thickness and whether the sample is multilamellar. The overall magnitude of the sample scattering intensity is determined by volume fraction.

For DPPC, it is clear from the turnover at high-q and the small peak/disclination in the scattering profile at q = 0.008 $Å^{-1}$ that liposomes are present for the pure lipid sample. Model fits indicate an overall diameter of 900 Å and bilayer thickness of 40.0 Å. The polydispersity

of these liposomes is quite high, in line with expectation from the preparation method used, with a polydispersity index of 0.3.

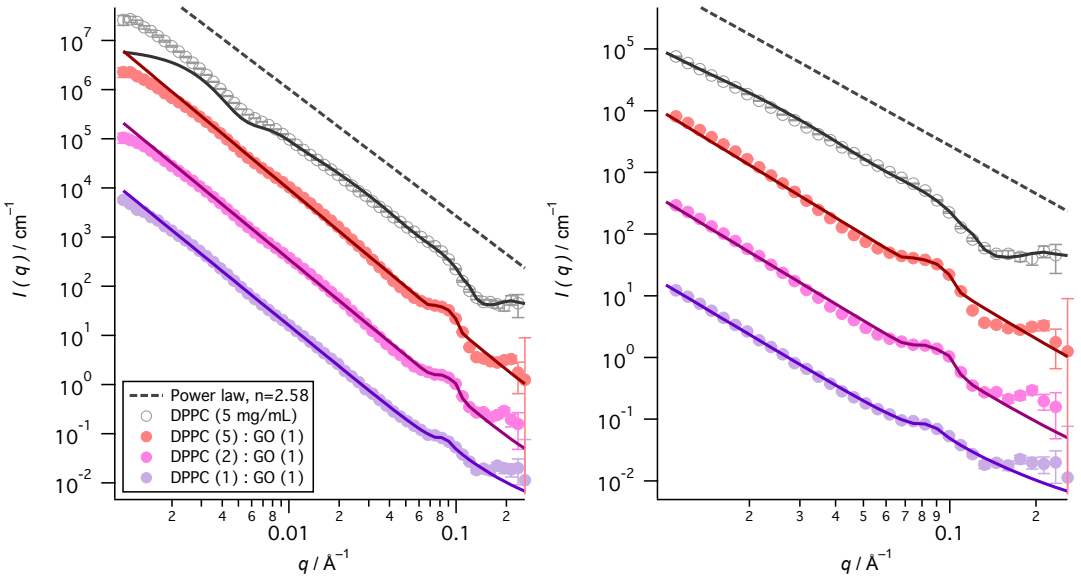


**Figure 6.4** Scattering plots of DPPC (5mg/mL) by itself and its interaction with different concentrations of GO. A) SANS data of DPPC by itself, and in mixtures with with GO (5:1, 2:1 and 1:1). B) zoomed in (reduced q-scale) image of the Porod region (high-q) of DPPC SANS and model fits. Symbols represent experimental scattering data and solid lines represent the best fit (see Tables 1 and 2). 3 different experiments performed.

Three different ratios of DPPC when mixed with GO were studied: 5:1, 2:1 and 1:1. Scattering data and model fits are displayed in Figure 6.4, with fitted model parameters shown in Tables 1 and 2. The Figure compares these to scattering data of DPPC (5 mg/mL) by itself. Comparing DPPC by itself with the different concentrations of added GO, there are some significant differences at both low q and high q. There is a trend in the shape of the scattering curve in all of these plots that can be fit consistently with the same model, albeit with some parameter changes.

The data at intermediate q in all the samples show similar gradients (Porod exponent ~2.8) indicating a rough or curved layer, most likely arising from reconfiguration of the lipids from the smooth surfaces of liposomes to a fractal composite with GO. The dip in the low q

region of the pure lipid scattering data shown in Figure 7 is largely due to convolution of bilayer thickness with core radius. This dip is usually not visible if the vesicles are too polydisperse or if their sizes are fairly large, which is the case in unextruded samples[25]. When GO is added to the system however, significant changes are seen.

When the ratio of DPPC:GO is 5:1, the downturn at low-q disappears and is replaced by a characteristic 'bump' at around q = 0.086 $Å^{-1}$. This loss of turnover at lowest q suggests that the liposomes are aggregating into a flatter structure or fragments that are fractally arranged. Interestingly, at this lipid:GO ratio, it appears that there is a coexistence between some remaining liposomes and stacked lipid fragments. As the vesicle structures disappears, the emerging correlation peak at q = 0.086 $Å^{-1}$ indicates the formation of stacked bilayers. A bilayer by itself is around 40 Å in thickness, and the correlation length in DPPC is between 70–73 Å, and the thickness of a water layer between adjacent bilayers in multilamellar vesicles is 19 Å (Table 2). Summing these gives 60 Å, and therefore does not explain the correlation length seen. This may instead indicate that GO is present between adjacent bilayers, and many studies have indicated a thickness of GO sheets of around 10 Å [30], so this would be consistent with our observations.

When the ratio of DPPC:GO is 2:1 and 1:1, the scattering data shows somewhat similar structural features, although there is no longer strong evidence of a coexistent population of liposomes, and instead it appears that all of the lipid is now present as stacked bilayer fragments. The turnover in the low-q region disappears, and a peak is evident at around q = 0.086 $Å^{-1}$. However, the intensity (prominence) of the peak is lower when the ratio of DPPC:GO is 1:1. This may be because there are fewer liposomes per GO sheet to form composite structures, and hence less multilayer stack is formed.

Considering the behaviour that is dent from the scattering, we posit the following observations: when GO was introduced to the sample, it interacted with the liposomes and

ruptured these liposomes, resulting in formation of a stack of lipid multilayers with GO between them. At low GO loadings, some liposomes persisted, but when the GO concentration was increased, the liposomes gradually transitioned to multilamellar fragmentary structures, no longer looking morphologically like a liposome. The correlation length of DPPC with GO is anywhere between 70–73 Å. This is well within the range that has been previously reported for stacked DPPC phases. Kucerka *et al.* had found a bilayer thickness for DPPC of 72.4 Å using x-ray scattering [31, 32], although this value evidently depends on the extent of solvent swelling, and our observations are still consistent with inclusion of GO between bilayers based on geometrical arguments.

#### 6.3.1.3 POPC interaction with GO

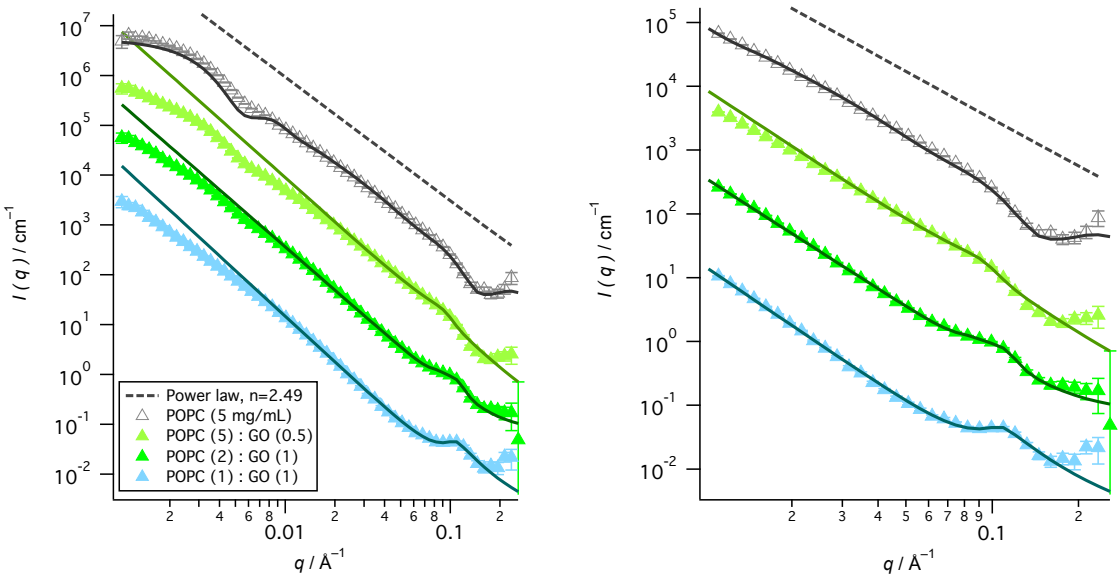


**Figure 6.5** Scattering plots of POPC (5 mg/mL) by itself and its interaction with different concentrations of GO. A) SANS data of POPC by itself, and in mixtures with with GO (5:0.5, 2:1 and 1:1). B) zoomed in (reduced q-scale) plot of the Porod region (high-q) of POPC SANS and model fits. Symbols represent experimental scattering data and solid lines represent the best fit (see Tables 1 and 2). 3 different experiments performed.

POPC is the most abundant lipid in biological cell membranes, and it has one saturated and one unsaturated carbon chain. At room temperature, POPC is in its liquid crystalline phase (unlike DPPC) with a chain melting temperature ($T_m$) of –2°C.

Scattering data from pure POPC liposomes is similar to that from pure DPPC. The diameter of the POPC vesicles is about 920 Å, which is similar to the measured DPPC vesicle size. The vesicle size of the POPC is slightly smaller than is typically reported in literature where samples were prepared using extrusion methods. However, the size of the vesicles can be dependent on lots of factors including temperature, number of extrusion cycles and the buffer being used. The sizes of extruded POPC vesicles when passed through a 100 nm membrane can range from 800 Å to 1400 Å [25, 33]. For the pure lipid, the characteristic curve shape at low-q and high-q indicates that most of the vesicles are unilamelar. However, the small peak at q = 0.1 Å suggests the presence of a small population of multilamellar vesicles, and model fitting agrees with this (Table 2).

The POPC bilayer thickness has been shown to be close to 37 Å [34]. The bilayer thickness of POPC measured in these experiments is 37–38 Å (Table 2) which is very consistent with this, however from the scattering data it is also seen that the correlation peak that emerges when GO is added corresponds to a repeat spacing between 58-65 Å.

When GO is added to the POPC samples, pronounced structural changes appear as seen in the SANS data in Figure 8. When the POPC:GO ratio is 5:0.5, the turnover at low-q slowly starts to disappear, and a peak at around q = 0.091 $Å^{-1}$ starts to appear, which suggests that the vesicles are breaking down and forming a mixture of stacked bilayers that may be fractally arranged or aggregated. In case of DPPC, there was a much more sudden change in the scattering behaviour compared to the more gradual morphological change seen for POPC, and this could be because the packing of the vesicles will be slightly different

and the difference in phase at room temperature might change the type of interactions between GO and the liposomes. For POPC, the change of liposomes to stacked multilayer is more gradual with increasing GO concentration, which corresponds to a gradual increase in stacked/fractal character of the samples. It could be that GO is rupturing the liposomes and they are forming a bilayer and GO may be in between those layers. When the lipid:GO ratio reaches 1:1, the Bragg peak at q = 0.107 $Å^{-1}$ is more pronounced, and almost all of the liposome seems to have disappeared to form multilamellar stacks, with a correlation distance of 58.7 Å. The correlation distance of DPPC in the presence of GO was around 70–72 Å whereas the correlation distance in POPC is considerably shorter, between 58-65 Å depending on GO concentration. Given that the POPC bilayer can be anywhere from 36–42 Å , typically with a water layer thickness of 17–19 Å, it is possible that when the lipid:GO ratio is 1:1, most of the sample will be present as stacked bilayer fragments, although given the smaller total inter-layer distance, it seems less likely for POPC that GO is trapped between the bilayers.

### 6.3.2 Anionic liposome (POPC/POPS) interaction with GO

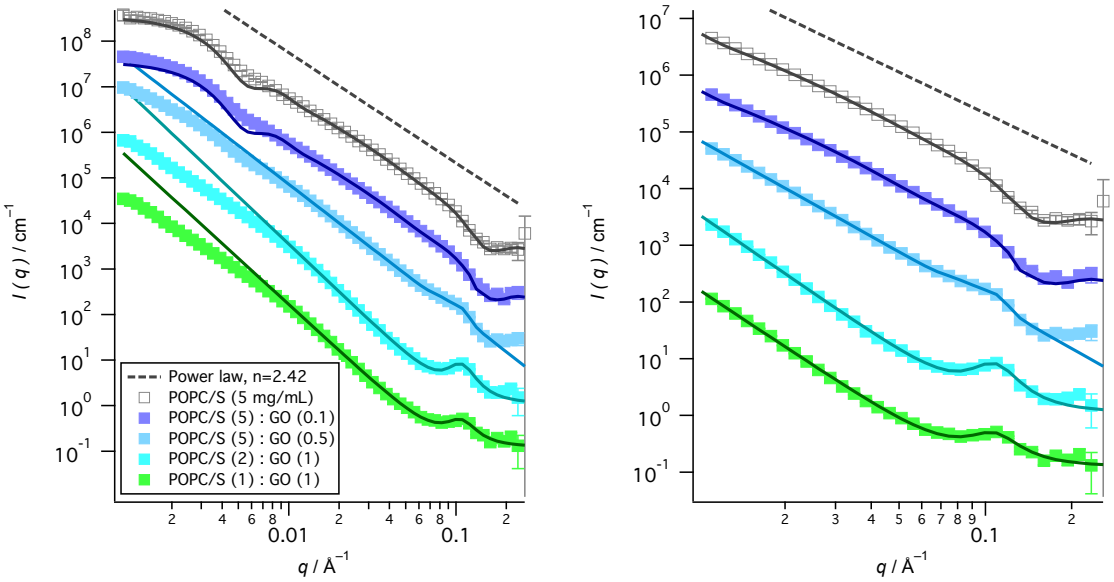


**Figure 6.6** Scattering plot of POPC:POPS (3:1) by itself and with different concentrations of GO. A) SANS data showing POPC:POPS (3:1) by itself, and this lipid combination with GO (5:0.1, 5:0.5, 2:1 and 1:1). B) zoomed in (reduced q-range) plot of the Porod region (high-q) of POPC:POPS SANS data and model fits. Symbols represent experimental scattering data and solid lines represent the best fit (see Tables 1 and 2). 3 different experiments performed.

The overall charges of the lipid POPS is negative, however, POPS contains a negatively charged phosphate group as well as a zwitterionic serine amino acid residue. Thus, the charge behaviour of POPC:POPS is anticipated to be complex, but we would expect the surface of the lipid layer to bear net more negative charge than the zwitterionic cases studied above. POPC:POPS liposome scattering data was fitted using a multilamellar vesicle model. The pure lipid scattering data shows a very clear rounding over at low-q that represents the spherical form factor of the liposomes. There is also has a dip at high-q that corresponds to the vesicle bilayer thickness, and these vesicles are the most monodisperse in terms of unilamellarity studied this work (see Table 2).

The scattering data in Figure 8 show a gradual change in liposome structure when different concentrations of GO were introduced. The peak shape at high q differs from the

previous systems studied. When GO was added in the ratio of (5:0.1, POPC/PS: GO), the scattering data shows very little change, and most likely corresponds to unilamellar vesicles that may not have a significant amount of bilayer stacking. However, when the ratio between liposomes and GO was increased to 5:0.5, the dip in low q starts to disappear and is replaced by a growing Bragg peak at q = 0.094 $Å^{-1}$. When the ratio of vesicles to GO was decreased further to 2:1 and 1:1, the scattering data is dominated mostly by the Bragg peak in the high q (but now shifted slightly to q = 0.1061 Å and 0.105 Å respectively). These samples were modelling using a broad Lorentzian peak fit to describe the correlation peak at high-q, plus Porod exponent. In the mid q region, unlike other systems studied, the slope changes markedly and this could be potentially because the surface of the stacked bilayers is no longer flat, or the fragments produced are smaller than in other systems. This suggests that the liposomes are ruptured by the GO sheets and this creates stacking where GO is potentially trapped in between.

When the ratio of lipid to GO is slowly increased, the change in vesicle structure to fractal/stacked structure is gradual rather than immediate. The Porod exponent for the data in Figure 8 ranges between 2.8–3.5 (see Table 1), which is higher compared to previously discussed POPC and DPPC samples. This also suggests that the surface of the sample is not smooth. The shape of the Bragg peak (at q~0.10 $Å^{-1}$) in this sample is flatter compared to the previous two systems studied, which suggests less ordered correlations. This also suggests that the stacking is less structured and less rigid, which is possibly because fewer lipids are sticking to GO. This is potentially because the anionic liposomes repel the negatively charged GO and hence result in less fractal aggregation.

### 6.3.3 Zwitterionic liposome interaction with rGO

Reduced GO sheets are similar to graphene, and are known as rGO. Once most of the oxygen atoms have been removed to form rGO, the material becomes more difficult to

disperse because it tends to aggregate due to increased hydrophobicity. Thus it may be anticipated that rGO could locate differently within lipid membranes compared to GO.

Reduced graphene oxide (rGO) does retain some peripheral negatively charged groups, making it dispersible in water up to around 0.15 mg/mL (hence the lower concentrations used here compared to GO), and this may further contribute to interactions seen with lipid systems.

### 6.3.4 DPPC interaction with rGO

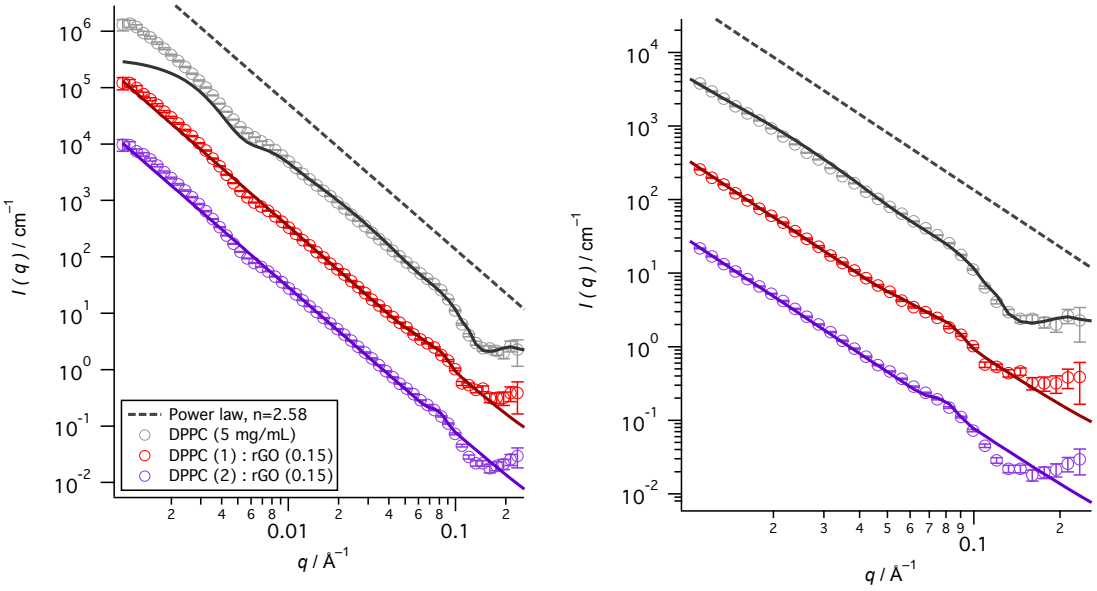


**Figure 6.7** Scattering plot of DPPC by itself and with different concentrations of rGO. A) SANS data showing DPPC by itself, and with GO (1:0.15 and 2:0.15). B) zoomed in (reduced q-range) plot of the Porod region (high-q) of DPPC/rGO SANS data and model fits. Symbols represent experimental scattering data and solid lines represent the best fit (see Tables 3 and 4).

As discussed previously, the scattering data in Figure 6.7 for pure DPPC indicates vesicle characteristics based on the turnover at high-q and the characteristic shape at low *q*. rGO is added in low concentrations because it tends to aggregate at high concentrations and is overall less stable than GO. Interestingly at both lipid to rGO ratios (1:0.15 and

2:0.15), the liposome characteristics in the scattering data are only slightly reduced, indicating that vesicles persist and little interaction with rGO occurs. A very small peak at high-*q* suggests there may be some rupture of the vesicles and formation of multilamellar stacking, but this is significantly less than compared to DPPC vesicles when interacting with GO. For consistency with the above data sets, these samples were fitted using a broad Lorentzian peak with Porod exponent model, with fitted parameters show in Table 3.

From these data, we can determine that the interaction of rGO with DPPC liposomes is much weaker than compared to GO. The correlation length for the small multilamellar peak that emerges at high-*q* is 79.5–89.8 Å, which is within the range that could be anticipated for stacked bilayers with a water space between them plus rGO. From these data and the weak overall level of interaction, it is not possible to determine whether rGO is hosted within the bilayers themselves (*i.e.* the hydrophobic region) or in the water space between bilayers. The Porod exponent is 2.6 which suggests that the surface of the sample is fairly flat.

The interaction of rGO with the zwitterionic DPPC liposomes is clearly weak, and this may be due to the less amphiphilic nature of rGO when compared to GO, inhibiting rGO from strongly interacting and rupturing the vesicles to create stacks of lipid bilayer. GO is often (incorrectly) described as a surfactant, although it is amphiphilic in nature [35], and can use this characteristic to interact strongly with a range of materials such as surfactants, polymers and particles [36]. rGO on the other hand has considerably reduced amphiphilicity, and so the lower level of interaction seen here is consistent with these characteristics.

**Table 6.3** Fitted SANS parameters for interaction of rGO with lipids where a 'broad peak' (Lorentzian plus Porod exponent) was used to fit scattering data.

| Lipid | Lipid conc. | rGO conc. | Peak pos. | Corr. length | Porod expon. |
|---|---|---|---|---|---|
| | mg/mL | mg/mL | $Å^{-1}$ | Å | |
| POPC | 1 | 0.15 | 0.0955 | 29.7 | 2.67 |
| POPC | 2 | 0.15 | | | 2.49 |
| DPPC | 1 | 0.15 | 0.07 | 50 | 2.6 |
| DPPC | 2 | 0.15 | 0.079 | 100 | 2.58 |

**Table 6.4** Fitted SANS parameters for interaction of rGO with lipids where a multilamellar vesicle was used to fit scattering data.

| Lipid | Lipid conc. | rGO conc. | Volume fraction | Radius (PD) | Shell thickness | Solvent thickness | $N_{shells}$ (PD) |
|---|---|---|---|---|---|---|---|
| | mg/mL | mg/mL | | Å | Å | Å | |
| DPPC | 5 | 0 | 0.020 | 450 (0.3) | 40 | 19 | 1.05 (0.3) |
| POPC | 10 | 0 | 0.037 | 460 (0.24) | 38 | 17 | 0.9 (0.39) |
| POPC | 5 | 0.15 | 0.024 | 460 (0.24) | 38 | 22 | 0.9 (0.38) |
| POPC | 5 | 0.1 | 0.031 | 460 (0.24) | 38 | 19 | 0.92 (0.38) |
| POPC | 5 | 0.05 | 0.036 | 460 (0.24) | 38 | 26 | 0.9 (0.37) |
| POPC:POPS | 5 | 0 | 0.029 | 460 (0.24) | 37 | 19 | 0.95 (0.3) |
| POPC:POPS | 1 | 0.15 | 0.0105 | 480 (0.24) | 36 | 19 | 0.95 (0.36) |
| POPC:POPS | 1 | 0.05 | 0.011 | 480 (0.24) | 36 | 19 | 0.96 (0.36) |

### 6.3.5. POPC interaction with rGO.

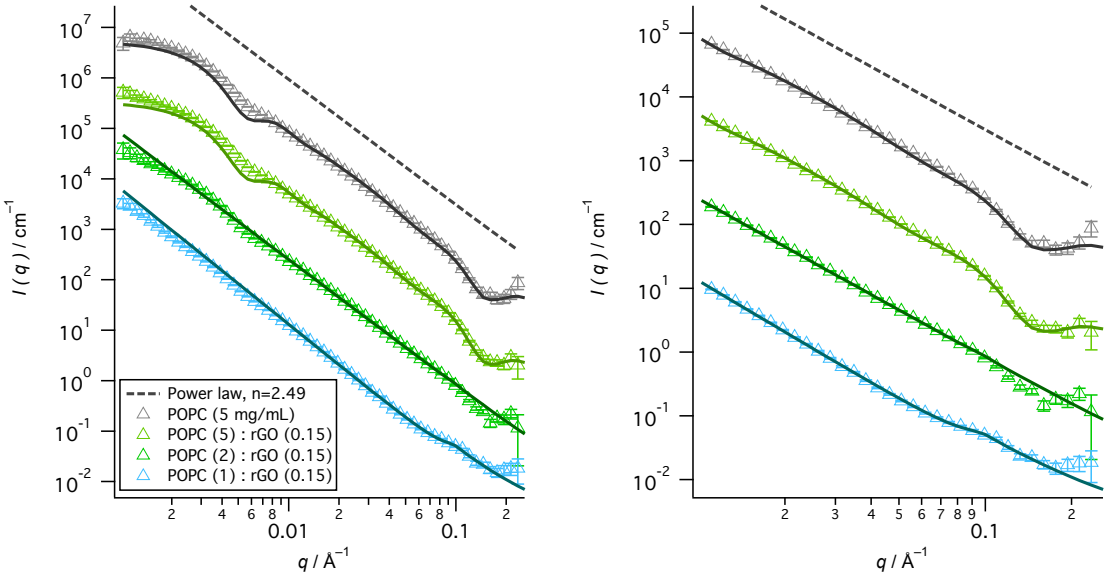


**Figure 6.8** Scattering plot of POPC by itself and with different concentrations of rGO. A) SANS data showing POPC by itself, and with GO (1:0.15, 2:0.15 and 5:0.15). B) zoomed in (reduced q-range) plot of the Porod region (high-q) of POPC/rGO SANS data and model fits. Symbols represent experimental scattering data and solid lines represent the best fit (see Tables 3 and 4).

Figure 6.8 shows the scattering data of POPC by itself and with different ratios of added rGO. The POPC liposome scattering data by itself were fitted with a model describing multilamellar vesicles, as noted in the sections above, and with fitted parameters shown in Table 2. rGO was added to the liposome sample in increasing concentration to give final ratios of POPC to rGO of 5:0.15, 2:0.15 and 1:0.15. When the lipid:rGO ratio was 5:0.15, the scattering data looks very similar to the POPC liposome by itself, and hence it was fitted with the multilamellar vesicle model as well. On increasing the proportional ratio of rGO however, significant changes are seen, meaning that the rGO was interacting with the vesicles and forming a composite structure. Interestingly the transition in behaviour is much more gradual than was seen for the interaction of this lipis with GO, and the data does not really show any significant Bragg peak around q = 0.1 Å$^{-1}$ either. Only when the ratio is

1:0.15, a small peak appears at around this point, suggesting a small contribution of stacking of the bilayer, but not to the extent seen with GO.

Like DPPC, POPC has a polar head group that repels negatively charged rGO. The disappearance of turnover in low q indicates some of the liposomes interact and rupture to form fractal/stacked (composite) material. However, the liposome signature ‘bump’ around q =0.08 $Å^{-1}$ indicates that significant amount of the vesicles are still intact. When the lipid:rGO ratio is 1:0.15, a weak Bragg peak appears at q =0.095 Å suggesting the presence of multilayer stacking. The correlation length corresponding to this peak is 65.8 Å, which is consistent with the spacing seen for POPC with GO, and likely indicating stacking of the lipid around the carbon nanomaterial sheets. The Porod exponent of this sample is 2.67, and this suggests that the sample surface is flat. It is possible that because rGO is not as polar (or amphiphilic) as GO, the interaction with the zwitterionic liposomes is limited, and rGO may not have a mechanistic path to rupture the liposomes easily.

### 6.3.6 Negatively charged liposome interaction with rGO

#### 6.3.6.1 POPC:POPS (3:1) interaction with rGO

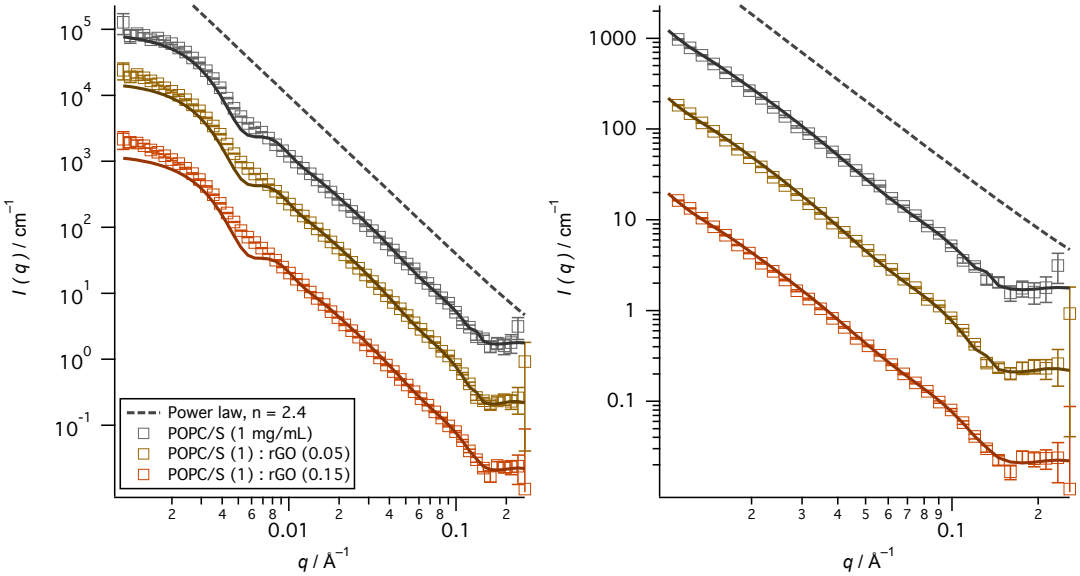


**Figure 6.9** Scattering plot of POPC:POPS (3:1) by itself and with different concentrations of rGO. A) SANS data showing POPC:POPS (3:1) by itself, and this lipid combination with rGO (1:0.05, 1:0.15). B) zoomed in (reduced q-range) plot of the Porod region (high-q) of POPC:POPS SANS data and model fits. Symbols represent experimental scattering data and solid lines represent the best fit (see Tables 1 and 2). 3 different experiments performed.

POPS has a net negative charge and POPC is zwitterionic, and therefore these mixed lipid liposomes have a net negative charge. The liposomes only scattering has been described above, and fitted parameters are shown in Table 2. When (negatively charged) rGO was added to the liposome samples, the spectra stay almost entirely the same. The turnover at low-q and the downturn at high-q remain the same, indicating that there is no interaction of rGO with the liposomes. It is possible that rGO sticks to the surface of the vesicles, as this would not be seen in the scattering profiles due to the very weak scattering contribution of rGO, but we anticipate that this is unlikely as negatively charged rGO would likely be repelled by negatively charged liposomes. It is possible that the repulsive forces are strong enough for rGO to not come in contact with the liposomes at all, and the two materials co-exist as a stable, non-interacting dispersion.

When GO was placed with these negatively charged liposome samples, we saw the opposite effect. GO interacted with the liposomes strongly and rapidly, and generated multilamellar stacks confirmed by the emergence of a peak at q~0.1 $Å^{-1}$. GO contains hydrophilic and polar groups along with a somewhat hydrophobic basal plane, and this amphiphilic character means that it can interact with the hydrophilic head-groups comprising the surface of the liposomes. In the case of dispersed liposomes, this interaction leads to the rupture of the vesicles and entrapment of the GO. No such interaction is seen with rGO, marking a significant difference in behaviour that hints at mechanistic effects.

## 6.4 Discussion and conclusion

Our aim for this chapter was to study the interactions of GO and rGO with model membrane systems. It is difficult to replicate the true complexity of the cell membrane but using biomimetic membranes we can study how representative lipid bilayers (here in the form of liposomes) interact with GO and rGO. This study included lipids with different alkyl chain lengths, different charges (zwitterionic and anionic) and different head group chemistry. In the previous chapter, we discussed some of these interactions using model supported lipid bilayer membranes at surfaces, and in the present chapter we focused our study on bulk interactions using vesicles.

Neutron scattering data in these studies clearly show that liposomes do interact with GO and rGO, at least to some extent, in most of cases. In some cases, the interaction leads to the rupture of the vesicles and in some cases it seems likely that GO becomes sandwiched between the bilayers in the lipid–GO composite hybrids formed. In some cases, it is seen that the carbon nanomaterials do not interact with the vesicles, which may be because of the charges on the liposomes and the carbon nanomaterials. Figure 6.10 summarises the anticipated morphological interactions seen and outcomes thereof.

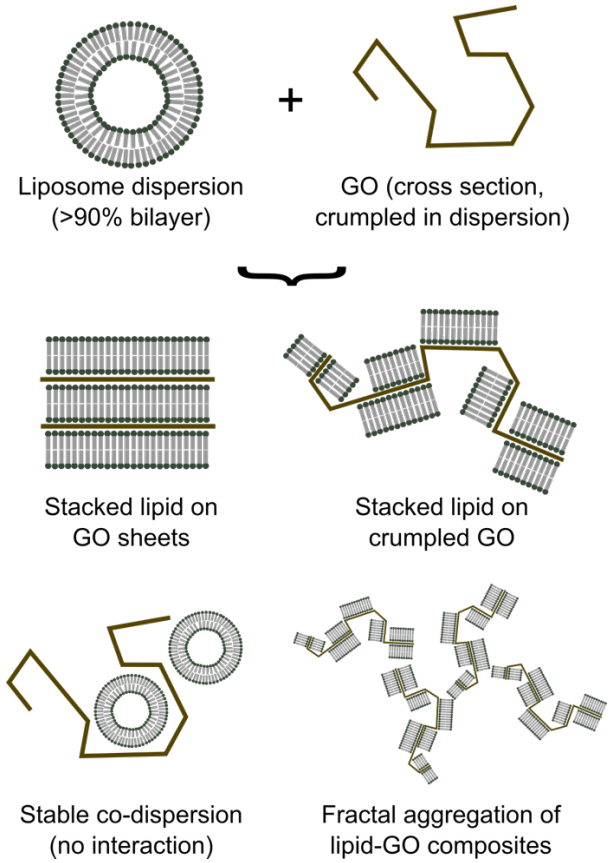


**Figure 6.10** Schematic showing the hypothesised outcomes of GO (rGO) interactions with liposomes.

The neutron scattering dataset shows the shape and the thickness of the liposome/lipid bilayer. In many cases, there is also a diffraction peak that can identify orientational interactions between bilayers present in the sample. Analysis of this peak provides the correlation length between layers when stacked phases occur. In this case, the hydration and repulsion between lipid headgroups results in a water layer (of dimensions typically 16–20 Å) in which GO could be hosted. In cases where a strong liposome form factor is not present, we can also look at the flatness/tortuosity (as evidenced by the Porod exponent) of the stacked bilayer.

These experiments clearly show that before interaction with GO/rGO, most of the vesicles are intact and do not seem to be rupturing by themselves, even in the high energy

mixing conditions of the stopped flow cell in which samples were prepared and mixed on-line. However, when GO was added to these vesicles, most samples showed evidence of multilamellar stack formation in the high-q region. This suggest that when vesicles come in contact with GO sheets, they rupture and stack on top of one another to form a multilamellar stack. In most of these cases, the correlation length corresponding to this stacking also matches with previously published data.

When rGO was added to zwitterionic liposomes, the interaction ruptured the liposomes and generated a lamellar stack similar to what GO did when interacting with the liposomes. However, with anionic liposomes, rGO did not seem to interact and the vesicles mostly remained intact. Interestingly, we also saw similar results with AFM as well. In the case of zwitterionic lipids, GO interacts with the bilayer and liposomes rapidly and at low concentration of GO. In the case of supported POPC lipid bilayers (shown in the previous chapter), GO interacts with the bilayer membrane, which results in bilayer defects which can be seen using AFM. These defects in the bilayer membrane can also be analysed using quartz crystal microbalance with dissipation monitoring as seen in the previous chapter. Using scattering data in this chapter, we have shown that GO interacts with zwitterionic (both DPPC and POPC) liposomes instantaneously, resulting in vesicles being ruptured. This led to the stacking of bilayers and in most cases GO could have been trapped in between the bilayers.

DPPC is a di-chain, fully saturated lipid, and POPC has one saturated and one unsaturated alkyl chain. They have vastly different transition temperature, 41°C for DPPC and –2 °C for POPC. DPPC at room temperature is in its gel phase and this can potentially change the acyl chain configuration, resulting in a change in liposome topology. The lipid head groups and the acyl chains are tightly packed resulting in increased van der Waals interactions. GO interacts strongly with both zwitterionic and negatively charged liposomes.

In case of negatively charged liposomes, the interaction with GO is more gradual and dependent on the concentration of GO added. This could be because both materials are negatively charged and to some extent repel each other. However, GO does still interact with POPC:POPS and results in a mixture of fractal/stacked lipid material. GO is more polar and notable amphiphilic, and this maybe the reason why it can interact strongly with the liposomes.

rGO interactions with both zwitterionic and negatively charged lipid were quite different when compared to interactions with GO. rGO interactions with the liposomes were generally weaker, and resulted often in mixed or intermediate morphologies. rGO lacks oxygen containing groups such as hydroxyl groups, and it is less polar (and more hydrophobic) and this affects the interaction with liposomes. Notably, it is much less amphiphilic than GO. Particularly in the case when the liposome is negatively charged, rGO interactions were very minimal. The liposomes and rGO effectively repel each other, and only at high rGO ratios was very minor evidence of any morphological change in the liposomes seen. The correlation length and other parameters suggest that the stacking is quite different to that seen with zwitterionic lipids.

Liu *et al.* studied antibacterial activity of graphene based materials and found that graphene can potentially be cytotoxic to bacteria [11]. They studied the effects of graphene based materials against E. coli and found that the graphene sheets can penetrate cell membranes spontaneously and extract phospholipids from cell membranes. [10, 12, 37]. These studies suggested that the GO sheets needed direct contact in order to inactivate the bacterial cell membrane. However, some of recent studies has suggested that bacterial inactivation can be achieved by the oxidative stress induced by GO sheets [38]. In the last 2 chapters, we have seen similar GO interactions with supported lipid bilayers and liposomes. In the case of supported bilayers, GO ripped apart the bilayer to form a

nanocomposite structure, and liposomes were ruptured to form a bilayer stack. Both of these observations indicate a contact-based mechanism for GO's interaction with cell membrane lipids.

In summary, contrary to previous investigations, but in congruence with the previous chapter in this thesis, GO and rGO can interact with typical cell membrane lipids in surprisingly diverse ways. This can result in significant morphological changes for these lipid structures, particularly in the case of the more water dispersible GO when compared to the more hydrophobic rGO. This surprising result is rationalised in the context of the significantly more amphiphilic nature of GO, enabling it to attach to and disrupt liposomes much more effectively than can rGO.

## 6.5. References


1. Richter, R.P., R. Berat, and A.R. Brisson, Formation of solid-supported lipid bilayers: an integrated view. Langmuir, 2006. **22**(8): p. 3497-505.
2. Frost, R., *et al.*, Graphene oxide and lipid membranes: interactions and nanocomposite structures. Nano Lett, 2012. **12**(7): p. 3356-62.
3. Novoselov, K.S., *et al.*, Electric field effect in atomically thin carbon films. Science, 2004. **306**(5696): p. 666-9.
4. Geim, A.K. and K.S. Novoselov, The rise of graphene. Nat Mater, 2007. **6**(3): p. 183-91.
5. Tombros, N., *et al.*, Electronic spin transport and spin precession in single graphene layers at room temperature. Nature, 2007. **448**(7153): p. 571-4.
6. Hollister, S.J., Porous scaffold design for tissue engineering. Nat Mater, 2005. **4**(7): p. 518-24.
7. Holzinger, M., A. Le Goff, and S. Cosnier, Nanomaterials for biosensing applications: a review. Front Chem, 2014. **2**: p. 63.
8. Bhunia, S.K., *et al.*, Carbon nanoparticle-based fluorescent bioimaging probes. Sci Rep, 2013. **3**: p. 1473.
9. Li, P. and S.F.Y. Li, Recent advances in fluorescence probes based on carbon dots for sensing and speciation of heavy metals. Nanophotonics, 2021. **10**(2): p. 877-908.
10. Li, Y., *et al.*, Graphene microsheets enter cells through spontaneous membrane penetration at edge asperities and corner sites. Proc Natl Acad Sci U S A, 2013. **110**(30): p. 12295-300.
11. Liu, S., *et al.*, Antibacterial activity of graphite, graphite oxide, graphene oxide, and reduced graphene oxide: membrane and oxidative stress. ACS Nano, 2011. **5**(9): p. 6971-80.
12. Tu, Y., *et al.*, Destructive extraction of phospholipids from Escherichia coli membranes by graphene nanosheets. Nat Nanotechnol, 2013. **8**(8): p. 594-601.
13. Li, S., *et al.*, Head Groups of Lipids Govern the Interaction and Orientation between Graphene Oxide and Lipids. The Journal of Physical Chemistry C, 2013. **117**(31): p. 16150-16158.
14. Huang, P.J., F. Wang, and J. Liu, Liposome/Graphene Oxide Interaction Studied by Isothermal Titration Calorimetry. Langmuir, 2016. **32**(10): p. 2458-63.
15. Frost, R., *et al.*, Graphene Oxide and Lipid Membranes: Size-Dependent Interactions. Langmuir, 2016. **32**(11): p. 2708-17.
16. Chadwick, J., Possible Existence of a Neutron. Nature, 1932. **129**(3252): p. 312-312.
17. Von Halban, H. and P. Preiswerk, Cross-Section Measurements with Slow Neutrons of Different Velocities. Nature, 1936. **137**(3474): p. 905-906.
18. Mitchell, D.P. and P.N. Powers, Bragg Reflection of Slow Neutrons. Physical Review, 1936. **50**(5): p. 486-487.
19. Borsali, R., R. Borsali, and R. Pecora, Soft-matter characterization. 1st ed. 2008, New York: Springer.
20. Hollamby, M.J., Practical applications of small-angle neutron scattering. Phys Chem Chem Phys, 2013. **15**(26): p. 10566-79.
21. Lakey, J.H., Neutrons for biologists: a beginner's guide, or why you should consider using neutrons. J R Soc Interface, 2009. **6 Suppl 5**: p. S567-73.
22. Berti, D. and G. Palazzo, Chapter 8 - Scattering of Radiation, in Colloidal Foundations of Nanoscience, D. Berti and G. Palazzo, Editors. 2014, Elsevier: Amsterdam. p. 177-197.

23. McCoy, T., Surfactant mediated control of aqueous graphene oxide dispersions, in chemistry. 2018, Monash University.
24. Fournet, A.G.a.G., Small-angle scattering of X-rays. 1955, New York: Wiley & sons.
25. Nele, V., *et al.*, Effect of Formulation Method, Lipid Composition, and PEGylation on Vesicle Lamellarity: A Small-Angle Neutron Scattering Study. Langmuir, 2019. **35**(18): p. 6064-6074.
26. van, T.H.L., *et al.*, Protein-Eye View of the in Meso Crystallization Mechanism. Langmuir, 2019. **35**(25): p. 8344-8356.
27. Bangham, A.D., M.M. Standish, and J.C. Watkins, Diffusion of univalent ions across the lamellae of swollen phospholipids. J Mol Biol, 1965. **13**(1): p. 238-52.
28. Ong, S.G., *et al.*, Evaluation of Extrusion Technique for Nanosizing Liposomes. Pharmaceutics, 2016. **8**(4).
29. Chapman, C.J., *et al.*, Factors affecting solute entrapment in phospholipid vesicles prepared by the freeze-thaw extrusion method: a possible general method for improving the efficiency of entrapment. Chem Phys Lipids, 1990. **55**(2): p. 73-83.
30. McCoy, T.M., A.C.Y. Liu, and R.F. Tabor, Light-controllable dispersion and recovery of graphenes and carbon nanotubes using a photo-switchable surfactant. Nanoscale, 2016. **8**(13): p. 6969-6974.
31. Kucerka, N., S. Tristram-Nagle, and J.F. Nagle, Structure of fully hydrated fluid phase lipid bilayers with monounsaturated chains. J Membr Biol, 2005. **208**(3): p. 193-202.
32. Kucerka, N., *et al.*, Structure of fully hydrated fluid phase DMPC and DLPC lipid bilayers using X-ray scattering from oriented multilamellar arrays and from unilamellar vesicles. Biophys J, 2005. **88**(4): p. 2626-37.
33. Frisken, B.J., C. Asman, and P.J. Patty, Studies of Vesicle Extrusion. Langmuir, 2000. **16**(3): p. 928-933.
34. Toroz, D. and I.R. Gould, A computational study of Anthracyclines interacting with lipid bilayers: Correlation of membrane insertion rates, orientation effects and localisation with cytotoxicity. Scientific Reports, 2019. **9**(1): p. 2155.
35. McCoy, T.M., *et al.*, Graphene oxide: a surfactant or particle? Current Opinion in Colloid & Interface Science, 2019. **39**: p. 98-109.
36. McCoy, T.M., *et al.*, Bulk properties of aqueous graphene oxide and reduced graphene oxide with surfactants and polymers: adsorption and stability. Physical Chemistry Chemical Physics, 2018. **20**(24): p. 16801-16816.
37. Kostarelos, K. and K.S. Novoselov, Materials science. Exploring the interface of graphene and biology. Science, 2014. **344**(6181): p. 261-3.
38. Gurunathan, S., *et al.*, Oxidative stress-mediated antibacterial activity of graphene oxide and reduced graphene oxide in Pseudomonas aeruginosa. Int J Nanomedicine, 2012. **7**: p. 5901-14.

# Chapter 7. Conclusions and Future directions

The first half of this thesis employed biophysical techniques to investigate autotransporter protein folding in biomimetic membranes, and the second part of the thesis focused on the interaction of graphene-based carbon nanomaterials with biomimetic membranes. While the two sections appear initially disparate, there are commonalities and parallels between the studies that offer additional physical insight into the role of model membrane systems in understanding biophysical interactions.

## 7.1 Pet β-barrel folding

The first part of the thesis focussed on autotransporter protein folding in the membrane and the stability of resultant folded protein. We used Pet protein as the model autotransporter protein for this study. Different motifs of outer membrane proteins have been explored over the years, and the predominant hypothesis is that conserved regions within these proteins play a significant role in protein folding in the outer membrane. Based on the secretion system, outer membrane proteins are classified into IX different groups, and the autotransporters arise from type V secretion systems. One of the interesting aspects of autotransporter folding is that there are no sources of energy for the protein transport, and this process also lacks ATP sources in the periplasm. To date, the source of energy for autotransporter folding and the secretion of the protein is still a mystery. The protein's passenger domain (N-terminal) contains the virulence factors of the Pet proteins, and in this case they are cleaved off autoproteolytically in the outer membrane. It is notable that Pet proteins are synthesised in the cytoplasm and travel through the inner membrane and periplasm unfolded.

Autotransporter proteins remain unfolded in the periplasm, and this is achieved because of the protein interaction with chaperone proteins such as SurA, Skp and DegP [1-5]. The barrel domain of the protein is then inserted in the outer membrane of the cell, and this facilitates the translocation of the passenger domain across the outer membrane. It has been known that the barrel domain folding and its insertion in the outer membrane is essential for the folding and translocation of the virulence factors of the autotransporter protein.

In this thesis, we identified conserved motifs in the barrel domain, and mutational studies were conducted to understand the importance of these conserved glycine residues. Phylogenetic analysis by Celik *et al.* had previously identified the similarity in autotransporter protein sequences [6]. Glycine residues are conserved in different strands of beta barrel domain; however it was still unclear what role these residues play (if any) in the folding of the barrel domain and the translocation of the passenger domain across the membrane. The first stage of the folding (barrel folding) is important because it determines whether the passenger domain can translocate to the cell surface in its functional form [7]. Natively folded beta barrel is essential for the translocation of the passenger domain. Pet $^{\Delta 1\text{-}902}G^{1061}A$ and Pet $^{\Delta 1\text{-}902}G^{1076}A$ were produced as mutated versions of the wild type Pet protein, where 1061 and 1071 are the positions of the mutated glycine residues on the full-length Pet protein. In these studies, these residues were mutated from glycine to alanine. Secondary and tertiary structure of the wild type and the mutated proteins were studied using CD spectroscopy and tryptophan fluorescence. The secondary structure and tertiary structure of the protein sample were different, and the conformation of Pet $^{\Delta 1\text{-}902}G^{1076}A$ was somewhat distorted. This was also shown by treating the folded samples with trypsin.

Non-native folding of the barrel domain affects the folding and the translocation of the passenger domain. Autoproteolytic cleavage of the passenger domain is an indication of

correctly folded (native-like) barrel. Tryptophan fluorescence spectra of wild type and mutated Pet protein confirmed that the folded structure is significantly different in each case. This meant that the mutated proteins were not achieving their native structure. Trypsinolysis of the folded protein sample generated a set of proteolytic products that are of different sizes depending on what part of the protein is exposed and what proteins are folded in their native structure. These (mutated Pet sample) proteolytic products were sequenced, and it was identified that proteolytic products containing passenger domain initiated at a different location compared to the wild type proteolytic products. This again proves that the mutation of glycine to alanine had a significant impact in the folding of the barrel domain, which in turn affects passenger domain folding and translocation across the outer membrane.

In addition to the mutational study, we also identified different sizes of Pet proteins and studied how passenger domain size difference affects protein folding. It became obvious that increasing the passenger domain size led to delayed autoproteolytic reaction of the Pet protein. Autoproteolytic reaction is the event whereby the passenger domain automatically separates from the barrel domain. We see that it is very important that the protein is folded in its native structure for this event to proceed. Fascinatingly, these results contradict previous studies with other autotransporters that found no dependence of folding on passenger domain size. This indicates that autotransporter protein folding is not governed universally by a single mechanism, and that a great deal of subtlety may be involved in the folding of such proteins.

Outer membrane protein folding is still an area that is very much under development, and such studies have occupied a minor place in protein folding investigations. In the last 10 years, there has been significant movement in the field of membrane protein structure biology. We used LDAO micelles to study the folding of the Pet protein, congruent with previous studies where outer membrane proteins are usually folded in a micelle or a lipid

bilayer to study their folding. This however poses some challenges to studying the stability, dynamics and function that are ultimately achieved for the membrane protein. The unusual properties of these membrane proteins require a specific environment so that the hydrophobic parts of the proteins can be accommodated within the membrane core and the hydrophilic pards of the protein are on the outside of the membrane, facing into the aqueous environment. In our approach, the beta barrel membrane proteins spontaneously fold into the membrane, and the stability, membrane contribution and the effect of protein sequence were thus studied. This work was necessary because these motifs and the conserved residues had never been studied and their purpose had not been identified. Just like other identified motifs, these residues affect the folding of the Pet protein, as shown in our study.

Even though the Pet protein was folded in its native structure in micelles successfully, it is unclear to what extent chaperone proteins and the Bam complex assist in the folding process, and it is still not understood whether the membrane folding, and insertion process will be different in the presence or the absence of the chaperones. Another outstanding question is how folding is affected in the case of a biomimetic membrane or even within liposomes. Comparative protein folding studies using micelles, liposomes and lipid bilayers would thereby provide further insights into folding and *in vivo* machinery, indicating the influence of different components present as well as phase curvature. Membrane fluidity would also be an interesting aspect to vary, exploring its effects on folding dynamics and protein assembly.

It was previously believed that the passenger domain is translocated from the channel formed exclusively by covalently bonded beta barrel [8]. However, our work suggests that this pathway may be somewhat more complex, and further insights are needed to better understand it. Beta barrel plays a significant role in translocation, however the passenger domain translocation across the membrane is complex and needs further study to

unambiguously isolate all mechanistic aspects. Our mutational study on the beta barrel showed that folding and/or integration of the β-barrel was compromised by mutation of key residues, which delayed the passenger domain translocation. Studies have suggested that the barrel domain achieves its native state only after the translocation of the passenger domain [9]. Several periplasmic chaperone proteins play important roles to keep autotransporter protein unfolded in the periplasm [10, 11]. The Bam complex is also known to play a role in autotransporter assembly as well as assembly of other beta barrel proteins [12, 13].

The role of the Bam complex (BamA, BamB, BamC and BamD) and chaperone proteins in autotransporter folding is still not clear. If we can better understand the role of the Bam complex and chaperone proteins in the biogenesis of autotransporter protein, we will have a better insight into autotransporter folding and passenger domain translocation in the outer membrane. The list of chaperone proteins that are known to interact with autotransporter proteins include DegP, FkpA, Skp and SurA. The next step in this project will naturally be to look at the interaction of these chaperone proteins with the Pet protein and to better understand their roles in the biogenesis of the Pet protein. Following this would be a study that looks into the interactions of the Bam complex with the Pet protein and its impact in the overall folding and translocation of Pet protein.

## 7.2 Interactions of biomimetic membranes with graphene oxide and reduced graphene oxide

Nanomaterials represent one of the most active research areas in modern science, impacting a wide range of disciplines including chemistry, materials science, medicine, sensors and more [14, 15]. Because of the unique 2D carbon geometry of graphene and its derivatives, there has been a great deal of interest in the scientific community in this family

of materials specifically [16]. Graphene based nanomaterials have been studied for different applications in drug delivery, gene therapy, biomedical imaging, as antibacterial agents, biosensors, in metal detection, and more [17, 18]. Whereas graphene itself is highly hydrophobic and non-dispersible in water without surfactants or polymers, graphene oxide (GO) is an oxidized form of graphene, which means that it is hydrophilic in nature. It is easily dispersible in water and is a cost effective and more stable version of graphene. The chemical structure of GO and its ability to be easily converted to reduced GO (rGO), with close resemblance to graphene, makes these materials attractive candidates for biomedical applications [19]. Due to the variety of functional groups present, they can also be potentially functionalised to target drug delivery and gene therapy [20, 21].

One question that we attempted to address in this work by exploring the interactions between carbon nanomaterials and representative cell membrane lipids was whether GO and rGO are biocompatible. In some experiments, GO has exhibited antibacterial and antimicrobial characteristics, but has been widely reported to be biocompatible [22]. However, high concentrations of GO have been seen to be potentially cytotoxic and may result in PC12 cells death as well [23-25]. Graphene based nanomaterials are continuously being studied in various biomedical applications such as drug delivery, antibacterial materials, gene delivery and more. It is therefore essential to better understand the interaction of GO and rGO with the cell membrane if we are to use these nanomaterials in drug delivery and other biomedical/biotechnological applications *in vivo*.

In this thesis, we explored interactions of GO and rGO with biomimetic membranes. Our goal was to conduct a comprehensive study of how these materials interacted using different lipid compositions. These lipids had different chain length, charges, different degrees of saturation and different concentrations. It is difficult to replicate the complexity of a cell membrane in its entirety, but we hypothesised that, similarly to the autotransporter

protein folding studies in the first half of the thesis, we could use biomimetic membranes as a suitable model to study GO/rGO interactions.

GO/rGO interacted with all of the biomimetic membranes used to some extent, but to a significantly different extent depending on the specific nature of the nanomaterial and the lipid. In many cases, this resulted in the formation of a distinct morphology that best resembled a nanocomposite, *i.e.* a hybrid of the two materials where lipid-coated GO or rGO sheets were often evident. AFM experiments clearly indicated that the integrity of bilayers were compromised after incubation with GO/rGO.

AFM images of pure lipid bilayers such as DOPC appear flat, however after incubation with GO, the bilayer contained GO flakes and was no longer flat, with a surface that looked very different morphologically. AFM force curves of DOPC when incubated with GO showed a characteristic peeling effect of the bilayer surface. It is clear that the bilayer did not have the same integrity after GO was introduced, and it was apparent that GO sheets had extracted lipid from the surfacec and formed a nanocomposite-like structure that was very adhesive to the cantilever tip. DOPC and rGO interacted as well and led to a formation of a stacked bilayers, similar in format to a nanocomposite.

We found that when GO was added to a negatively charged bilayer, interactions were much weaker, though this interaction did lead to some defects on the bilayer surface. However, disruption to the lipid bilayer was not to the same extent as for DOPC and POPC biomimetic membranes. It is noteworthy that the basis of this (weaker) interaction is a repulsive colloidal force: both GO and anionic lipids used for this study are negatively charged, tending to repel each other and thereby explaining the weaker interaction. GO interacted strongly with positively charged lipid bilayers and formed a complex mixture of GO and lipid fragments. When rGO was introduced to the charged bilayer sample, most of it remained dispersed in solution rather than interacting with the bilayer sample.

We also studied interactions between lipids and carbon nanomaterials using vesicles in the form of liposomes, following the progress of interactions using small-angle neutron scattering. Similarly to the supported lipid bilayer model, this study included lipids with different alkyl chain length, different charges and different head group charge/chemistry. These experiments clearly showed that before the interaction with GO/rGO, liposomes were intact and did not rupture by themselves even when aged for some time. However, when GO and rGO were added to the liposomes, most samples formed a multilamellar stack, as evidenced by the appearance of a characteristic Bragg peak in the high-*q* region of obtained small-angle neutron scattering profiles. When GO was introduced to a DPPC liposome sample, the data at intermediate *q* indicated a rough layer, which is most likely due to the formation of lipid fractal composites with GO. When GO was introduced to POPC:POPS (3:1), a Bragg peak appeared at high-*q*, indicating that GO interacted with the liposomes strongly and rapidly. This indicates that the lipid surface is no longer flat due to the rupture of liposomes, creating stacked layers where GO is potentially trapped between lipid layers/fragments.

Reduced graphene oxide (rGO) was added at lower concentration than GO because rGO aggregates at high concentrations in aqueous systems, and is generally less stable than GO in such circumstances. In most cases, liposome characteristics evident in SANS spectra remained intact because rGO interactions with liposomes were weak. Small peaks at high-*q* suggests that some liposomes were ruptured and formed a multilamellar stack. However, the peak at high-q was a lot smaller than compared to similar interactions of lipids with GO. This is probably a result of both the lower concentration of rGO and also because hydrated and charged lipid head groups may repel negatively charged rGO.

Despite variations, neutron scattering data showed that GO and rGO do interact with most of the liposomes studied at least to some extent. In some cases, these interactions

lead to vesicle rupture and in some cases GO became sandwiched between the bilayers to form lipid–GO hybrid structures. In other instance, the nanomaterials did not interact with the vesicles and this may be because of the charges on the liposomes and the nanomaterials. When reduced GO was added to zwitterionic liposomes, the liposomes ruptured and a lamellar stack was generated. This is similar to what was seen with GO and vesicle interactions. However, anionic liposomes remained intact when rGO interacted with them. The interaction of rGO with zwitterionic and negatively charged lipids were quite different when compared to their interaction with GO. rGO interactions with the liposomes were generally weaker and resulted in an intermediate morphology. Overall, we found that GO and rGO can interact with biomimetic membranes and vesicles in diverse ways which can result in significant changes in the system morphology, and indicate a range of interaction strengths depending on the specific chemistry of the lipids involved.

Major pharmaceutical company Merck recently announced a collaboration to develop the next generation of graphene-based bioelectronics to target severe chronic diseases. This is just one of many examples of increasing biological applications for graphene-based materials. Such materials are also being developed for use in a wide range of human medical interface technologies such as bioelectric sensory devices [26]. Because of graphene's potential biological applications, we need to understand its biocompatibility. In this work, we have used biomimetic membrane to mimic the mammalian cell membrane and study GO and rGO interactions with it. We found that in some cases GO and rGO significantly compromised this biomimetic membrane's integrity, indicating that careful testing and significant caution should be exercised when applying such materials. Even though (graphene like) rGO's interactions were generally weaker, it is possible that such materials could become oxidised within the body, resulting in more significant interactions.

Further to this study, it is essential to perform *in vivo* experiments to understand the interaction of carbon nanomaterials with more diverse cell membranes and its impact on cells themselves from a mechanistic standpoint. Live cell imaging techniques have made significant advances in the last few years, and are available at most modern universities such as Monash for collaborative work. Using advances fluorescence microscopy techniques such as direct stochastic optical reconstruction microscopy (dSTORM), one can look at a single molecule super-resolution images without having to use any activator fluorophore. Live cell imaging could be the vital next step in studying the effects of graphene and graphene-like nanomaterials on live cells.

## 7.3 References


1. Baud, C., *et al.*, Role of DegP for two-partner secretion in Bordetella. Mol Microbiol, 2009. **74**(2): p. 315-29.
2. Ieva, R. and H.D. Bernstein, Interaction of an autotransporter passenger domain with BamA during its translocation across the bacterial outer membrane. Proc Natl Acad Sci U S A, 2009. **106**(45): p. 19120-5.
3. Oberhettinger, P., *et al.*, Intimin and invasin export their C-terminus to the bacterial cell surface using an inverse mechanism compared to classical autotransport. PLoS One, 2012. **7**(10): p. e47069.
4. Pavlova, O., *et al.*, Mechanistic link between beta barrel assembly and the initiation of autotransporter secretion. Proc Natl Acad Sci U S A, 2013. **110**(10): p. E938-47.
5. Weirich, J., *et al.*, Identifying components required for OMP biogenesis as novel targets for antiinfective drugs. Virulence, 2017. **8**(7): p. 1170-1188.
6. Celik, N., *et al.*, A bioinformatic strategy for the detection, classification and analysis of bacterial autotransporters. PLoS One, 2012. **7**(8): p. e43245.
7. Leyton, D.L., *et al.*, A mortise-tenon joint in the transmembrane domain modulates autotransporter assembly into bacterial outer membranes. Nat Commun, 2014. **5**: p. 4239.
8. Pohlner, J., *et al.*, Gene structure and extracellular secretion of Neisseria gonorrhoeae IgA protease. Nature, 1987. **325**(6103): p. 458-62.
9. Peterson, J.H., S. Hussain, and H.D. Bernstein, Identification of a novel post-insertion step in the assembly of a bacterial outer membrane protein. Mol Microbiol, 2018. **110**(1): p. 143-159.
10. Sikdar, R., *et al.*, Folding of a bacterial integral outer membrane protein is initiated in the periplasm. Nat Commun, 2017. **8**(1): p. 1309.
11. Peterson, J.H., *et al.*, Selective pressure for rapid membrane integration constrains the sequence of bacterial outer membrane proteins. Mol Microbiol, 2017. **106**(5): p. 777-792.
12. Wu, T., *et al.*, Identification of a multicomponent complex required for outer membrane biogenesis in Escherichia coli. Cell, 2005. **121**(2): p. 235-45.
13. Hagan, C.L., S. Kim, and D. Kahne, Reconstitution of outer membrane protein assembly from purified components. Science, 2010. **328**(5980): p. 890-2.
14. Pradeep, T., NANO: The Essentials: Understanding Nanoscience and Nanotechnology. 2007, New York: McGraw-Hill Education.
15. The Chemistry of Nanostructured Materials. 2011, WORLD SCIENTIFIC. 336.
16. Zhu, Y., *et al.*, Graphene and graphene oxide: synthesis, properties, and applications. Adv Mater, 2010. **22**(35): p. 3906-24.
17. Singh, Z., Applications and toxicity of graphene family nanomaterials and their composites. Nanotechnol Sci Appl, 2016. **9**: p. 15-28.
18. Jang, H., *et al.*, Graphene-Based Flexible and Stretchable Electronics. Adv Mater, 2016. **28**(22): p. 4184-202.
19. Ray, S.C., Applications of graphene and graphene-oxide based nanomaterials. Micro and Nano Technologies Series. 2015, Amsterdam: Elsevier. 84 pages.
20. Gong, P., *et al.*, Fluorescence-switchable ultrasmall fluorinated graphene oxide with high near-infrared absorption for controlled and targeted drug delivery. Chemical Engineering Journal, 2018. **348**: p. 438-446.
21. Alibolandi, M., *et al.*, Fabrication of aptamer decorated dextran coated nano-graphene oxide for targeted drug delivery. Carbohydr Polym, 2017. **155**: p. 218-229.

22. Shahmoradi, S., *et al.*, Optimizing the nanostructure of graphene oxide/silver/arginine for effective wound healing. Nanotechnology, 2018. **29**(47): p. 475101.
23. Faraji, S., *et al.*, Electrospun poly-caprolactone/graphene oxide/quercetin nanofibrous scaffold for wound dressing: Evaluation of biological and structural properties. Life Sciences, 2020. **257**: p. 118062.
24. Zhang, Y., *et al.*, Cytotoxicity effects of graphene and single-wall carbon nanotubes in neural phaeochromocytoma-derived PC12 cells. ACS Nano, 2010. **4**(6): p. 3181-6.
25. Gurunathan, S. and J.H. Kim, Synthesis, toxicity, biocompatibility, and biomedical applications of graphene and graphene-related materials. Int J Nanomedicine, 2016. **11**: p. 1927-45.
26. Goldsmith, B. R., *et al.* Digital biosensing by foundry-fabricated graphene sensors. Scientific Reports, 2019. **9**: p. 1-10.